Multiple Generations of Granite in the Fosdick Mountains, Marie Byrd Land, West Antarctica: Implications for Polyphase Intracrustal Differentiation in a Continental Margin Setting

F. J. KORHONEN[1]*, S. SAITO[1,2], M. BROWN[1], C. S. SIDDOWAY[3] AND J. M. D. DAY[4]

[1]LABORATORY FOR CRUSTAL PETROLOGY, DEPARTMENT OF GEOLOGY, UNIVERSITY OF MARYLAND, COLLEGE PARK, MD 20742, USA

[2]INSTITUTE FOR RESEARCH ON EARTH EVOLUTION, JAPAN AGENCY FOR MARINE–EARTH SCIENCE AND TECHNOLOGY, 2-15 NATSUSHIMA-CHO, YOKOSUKA-CITY, KANAGAWA 237-0061, JAPAN

[3]DEPARTMENT OF GEOLOGY, COLORADO COLLEGE, COLORADO SPRINGS, CO 80903, USA

[4]DEPARTMENT OF GEOLOGY, UNIVERSITY OF MARYLAND, COLLEGE PARK, MD 20742, USA

Production of granite in the middle to lower crust and emplacement into the middle to upper crust at convergent plate margins is the dominant mechanism of crustal differentiation. The Fosdick Mountains of West Antarctica host migmatitic paragneisses and orthogneisses corresponding to the middle to lower crust and granites emplaced as dikes, sills and small plutons, which record processes of intracrustal differentiation along the East Gondwana margin. U–Pb chronology on magmatic zircon from granites reveals emplacement at c. 358–336 Ma and c. 115–98 Ma, consistent with a polyphase tectonic evolution of the region during Devonian–Carboniferous continental arc activity and Cretaceous continental rifting. The gneisses and granites exposed in the Fosdick migmatite–granite complex were derived from Early Paleozoic quartzose turbidites of the Swanson Formation and Ford Granodiorite suite calc-alkaline plutonic rocks, both of which are widely distributed outside the Fosdick Mountains and have affinity with rock elsewhere in East Gondwana. Granites of both Carboniferous and Cretaceous age have distinct chemical signatures that reflect different melting reactions and accessory phase behavior in contrasting sources. Based on whole-rock major and trace element geochemistry and Sr–Nd isotope compositions, Carboniferous granites with low Rb/Sr are interpreted to be products of melting of the Ford Granodiorite suite. Extant mineral equilibria

modeling indicates that the Ford Granodiorite suite compositions produce melt volumes >10 vol. % at temperatures above biotite stability, involving the breakdown of hornblende + plagioclase, consistent with the high CaO and Na$_2$O contents in the low Rb/Sr granites. The Carboniferous low Rb/Sr granites show a sequence from near-melt compositions to compositions with increasing amounts of early crystallized biotite and plagioclase and evidence for apatite dissolution in the source. Carboniferous granites derived from the Swanson Formation are scarce, suggesting that the significant quantities of melt produced from the now residual paragneisses were emplaced at shallower crustal levels than are now exposed. The Cretaceous granites are divided into two distinct groups. An older group of granites (c. 115–110 Ma) has compositions consistent with a dominant Ford Granodiorite source, and characteristics that indicate that they may be less evolved equivalents of the regionally exposed Byrd Coast Granite suite at higher crustal levels. The younger group of granites (c. 109–102 Ma) has distinct light rare earth element depleted signatures. The chemical and isotopic data suggest that these granites were derived from partial melting of both fertile and residual Swanson Formation and had low water contents, indicating that the source rocks may have been dehydrated prior to anatexis as the Byrd Coast Granite suite magmas were transferring

*Corresponding author. Present address: Department of Applied Geology, Curtin University of Technology, Perth, WA, Australia. Telephone: +61 8 9266 2446. Fax: +61 8 9266 3153. E-mail: f.korhonen@curtin.edu.au

through and accumulating at higher crustal levels. The Cretaceous granites derived from the Swanson Formation make up a prominent horizontally sheeted leucogranite complex. The accumulation of these melts probably facilitated melt-induced weakening of the crust during a well-documented transition from regional shortening to regional extension, the formation of a detachment structure, and rapid exhumation of the Fosdick migmatite–granite complex. These multiple episodes of melting along the East Gondwana margin resulted in initial stabilization of the continental crust in the Carboniferous and further intracrustal differentiation in the Cretaceous.

KEY WORDS: *active continental margin; anatexis; Antarctica; crustal differentiation; East Gondwana; Fosdick Mountains; granite petrogenesis; migmatite*

INTRODUCTION

Convergent plate margins are the primary sites for the generation of the continental crust, operating through mass additions of arc basalt, production of granite *sensu lato* by crustal anatexis, and hybridization of these melts in the deep crust (e.g. Tatsumi, 2000; Davidson & Arculus, 2006; Saito *et al.*, 2007; Otamendi *et al.*, 2009). Subsequent production of granite in the middle to lower crust and emplacement into the middle to upper crust is the dominant mechanism of intracrustal differentiation (e.g. Rudnick, 2003; Brown & Rushmer, 2006; Brown, 2009). To better understand the processes related to granite petrogenesis in a continental arc setting we have undertaken a multidisciplinary study of an exposed crustal section in the Fosdick Mountains of Marie Byrd Land, West Antarctica, which was part of the Paleozoic–Mesozoic convergent accretionary margin of East Gondwana.

The Fosdick migmatite–granite complex preserves a polyphase history characterized by Paleozoic Andean-style convergence along the East Gondwana margin in the Devonian to Jurassic, overprinted by regional extension and lithospheric thinning during the Cretaceous (e.g. Pankhurst *et al.*, 1998; Siddoway, 2008; Siddoway & Fanning, 2009; McFadden *et al.*, 2009, in preparation). Two major anatectic events have been identified—an older Devonian–Carboniferous event and a younger event in the Cretaceous—both events corresponding to a period of high-temperature metamorphism and the production of the voluminous granite (e.g. Siddoway *et al.*, 2004; Korhonen *et al.*, 2009). This location is particularly well suited to the investigation of granite production and the processes of intracrustal differentiation for two reasons. First, there were two discrete melting events, well separated in time. Second, the protolith source rocks in this region are well characterized, allowing petrogenetic models for the granites and migmatites to be developed and tested.

Here, we present field observations, zircon U–Pb chronology, and whole-rock, trace element and Sr–Nd isotope compositions of representative rock types in the region of the Fosdick Mountains. The specific aims of this study are to: (1) determine the crystallization age of selected granites in the complex; (2) constrain the source(s) and chemical differentiation of the granites; (3) investigate the effects and implications of accessory phase behavior on trace element and isotope compositions; (4) evaluate the possible genetic links among leucosomes within migmatites and granites within and above the Fosdick migmatite–granite complex; (5) place the petrogenesis of the granites in the context of events along the proto-Pacific margin of Gondwana. The results presented here, coupled with previous modeling of source rock fertility and the melting–melt loss history recorded in the host gneisses (Korhonen *et al.*, 2009), constrain processes related to two cycles of intracrustal differentiation during the evolution of a long-lived continental arc and have implications for understanding Devonian–Carboniferous continental margin activity and Cretaceous continental rifting along the active margin of East Gondwana.

GEOLOGICAL SETTING
Geological setting of the Ford Ranges

Rocks from Marie Byrd Land in West Antarctica record the Paleozoic–Mesozoic tectonothermal evolution of part of the active continental margin of East Gondwana (Fig. 1a and b; Pankhurst *et al.*, 1998; Vaughan & Pankhurst, 2008). In the Ford Ranges of western Marie Byrd Land, the oldest exposed unit is the Lower Paleozoic Swanson Formation (Fig. 1c), a folded and cleaved turbidite sequence, correlated with the Lachlan Group in Australia, the Robertson Bay Group in northern Victoria Land, and the Greenland Group in the Western Province of New Zealand (e.g. Adams, 1986, 2004; Ireland *et al.*, 1998).

The calc-alkaline I-type Ford Granodiorite suite intrudes the Swanson Formation (Fig. 1c; Weaver *et al.*, 1991); it was emplaced in the region during a short-lived pulse of magmatic activity at *c.* 375 Ma (Pankhurst *et al.*, 1998). Richard *et al.* (1994) reported a U–Pb zircon age of *c.* 353 Ma from inferred Ford Granodiorite suite rocks in the Chester Mountains (see also Richard & Kimbrough, 1991; Fig. 1c). Two-mica S-type granites in the region (Fig. 1d) yield similar U–Pb monazite ages of *c.* 359 and 351 Ma (Tulloch *et al.*, 2009). A minor magmatic pulse at *c.* 340–320 Ma has also been documented in the northeastern Ford Ranges and the Ruppert Coast, constrained by Rb–Sr whole-rock and sparse U–Pb zircon chronology (Pankhurst *et al.*, 1998; Mukasa & Dalziel, 2000). The youngest plutonic phase is the Cretaceous Byrd Coast Granite suite (Fig. 1d) with ages of *c.* 140 and 110 Ma (Adams, 1987; Weaver *et al.*, 1991).
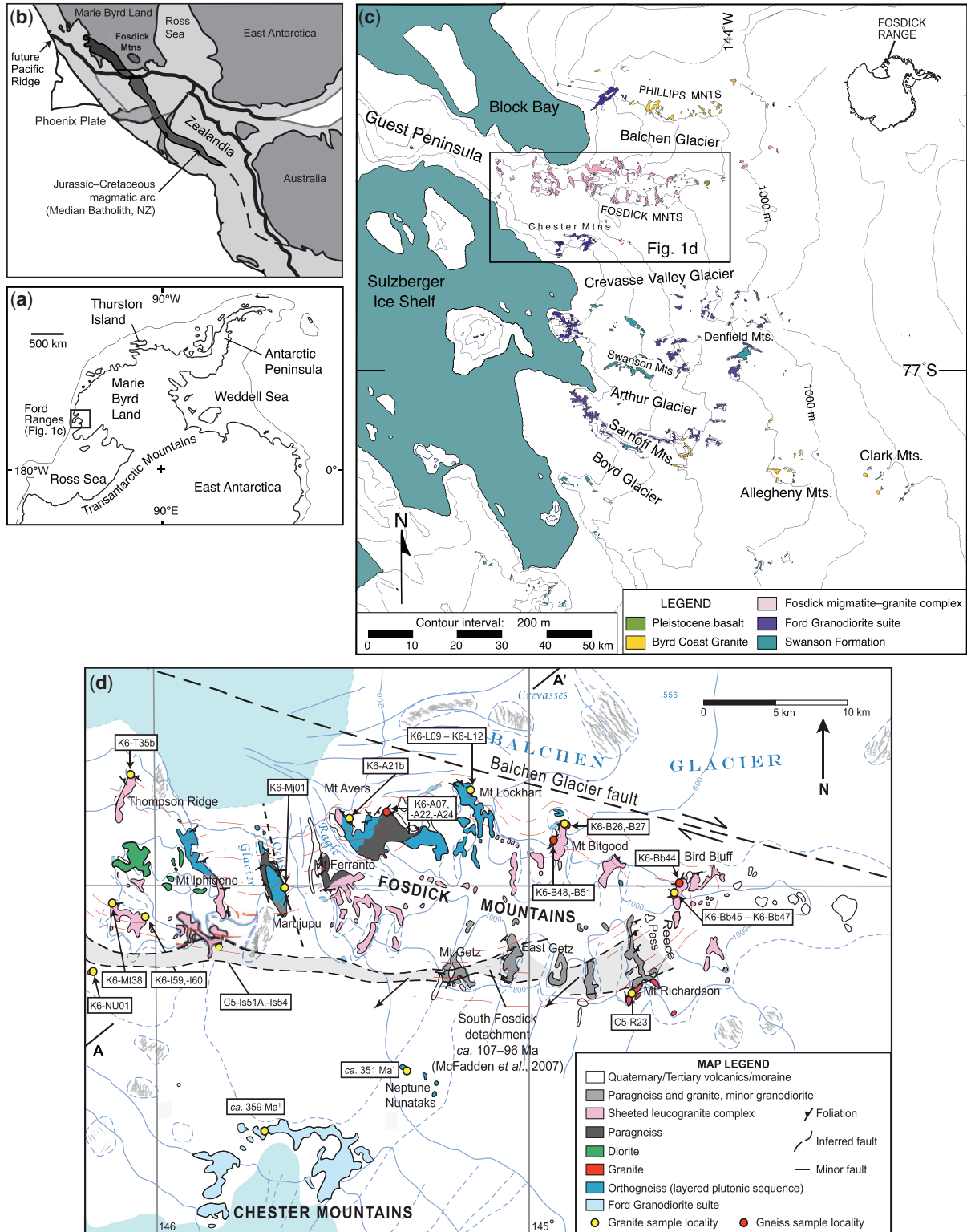
Fig. 1. (a) West Antarctica and location of the Ford Ranges. (b) Reconstruction of the East Gondwana margin at *c.* 95 Ma (modified from Tulloch *et al.*, 2006). (c) Geological map of the Ford Ranges (modified from Siddoway, 2008). (d) Geological map of the Fosdick migmatite–granite complex (modified from McFadden *et al.*, 2007) showing granite and gneiss sample locations. A–A' is the location of the SW–NE cross-section in Fig. 2. [1]U–Pb monazite ages from two-mica granites reported by Tulloch *et al.* (2009).

In the northern Ford Ranges, recent chronological investigations of a migmatite–granite complex in the Fosdick Mountains (Fig. 1d) have confirmed this polyphase history. U–Pb zircon ages from granite plutons and discordant leucogranite dikes range from *c.* 369 to *c.* 353 Ma, interpreted as constraining the timing of magmatism and migmatitization (Siddoway & Fanning, 2009). *In situ* U–Pb monazite chronology from host migmatites reveals younger ages of *c.* 340–310 Ma (Korhonen *et al.*, 2007; unpublished data). These studies have also shown that the Cretaceous episode of high-temperature metamorphism and anatexis commenced during tectonic convergence from *c.* 140 to 110 Ma, suggesting a prolonged period of crustal heating and melt accumulation (Siddoway *et al.*, 2004, 2006; Korhonen *et al.*, 2007; Siddoway, 2008; McFadden *et al.*, 2009, in preparation). The youngest crystallization ages of the Cretaceous leucogranites coincide with the onset of regional transtension at *c.* 100 Ma and development of the West Antarctic rift system (Siddoway, 2008; McFadden *et al.*, in preparation). The rapid change from regional convergence to rifting may be due to ridge–trench interaction (Luyendyk, 1995; Mukasa & Dalziel, 2000) or the presence of a mantle plume (Weaver *et al.*, 1994; Storey *et al.*, 1999).

The Fosdick migmatite–granite complex

The Fosdick Mountains form an elongate antiformal structure (80 km × 15 km) comprising migmatitic paragneiss and orthogneiss, and multiple phases of granite (Figs 1d, 2 and 3). The protoliths for the paragneiss and orthogneiss within the Fosdick migmatite–granite complex are interpreted to be the Swanson Formation and Ford Granodiorite suite, respectively, based on similar U–Pb zircon age populations (Siddoway *et al.*, 2004). The Fosdick migmatite–granite complex is bounded to the south by the South Fosdick detachment, a south-dipping, dextral oblique detachment zone (McFadden *et al.*, 2007), and to the north by the Balchen Glacier fault, an inferred steep dextral strike-slip fault (Siddoway *et al.*, 2004, 2005)

(Figs 1d and 2). U–Pb monazite ages from syn- to post-tectonic granites (Richard *et al.*, 1994) and U–Pb zircon ages from the South Fosdick detachment zone (McFadden *et al.*, 2007) constrain the timing of formation of the antiformal structure to *c.* 107–96 Ma.

The deepest structural level of the complex is an ∼5 km thick layered sequence of paragneisses and orthogneisses with granite distributed in decimeter- to kilometer-scale bodies and meter- to decimeter-scale sills and dikes (McFadden *et al.*, in preparation, has provided a detailed description of the units and their architecture; Fig. 2). The paragneiss and orthogneiss layers are foliated and commonly migmatitic, with millimeter- to centimeter-scale in-source leucosome (Fig. 3b; migmatite terminology after Sawyer, 2008). Domains of migmatitic paragneiss are exposed at Mt. Avers and in the western Fosdick Range, and ridges and summits to the east and west of Mt. Avers comprise a layered plutonic sequence (Fig. 1d). The layered plutonic sequence is made up of orthogneiss and meter- to decimeter-thick bodies of granite, granodiorite, and diorite with subordinate paragneiss in mostly concordant, laterally continuous layers (Siddoway & Fanning, 2009). This sequence grades into an ∼2 km thick section of voluminous sheeted leucogranites that localized in and beneath the South Fosdick detachment zone (McFadden *et al.*, in preparation). Granite bodies up to 100 m in thickness separate meter-thick layers of ortho- and paragneiss, resulting in a sheeted leucogranite complex with dominantly shallow fabrics (e.g. Fig. 3b; Siddoway *et al.*, 2004; McFadden *et al.*, in preparation). Beneath the South Fosdick detachment zone, granite and leucosome also occupy dilatant transverse structures, such as ductile shear bands, and relict melt flow networks connecting meter-scale sills and dikes (McFadden *et al.*, 2007). Above the leucogranite complex is a kilometer-thick section of leucosome-poor migmatite exhibiting solid-state fabrics associated with the South Fosdick detachment zone (McFadden *et al.*, 2007, in preparation).
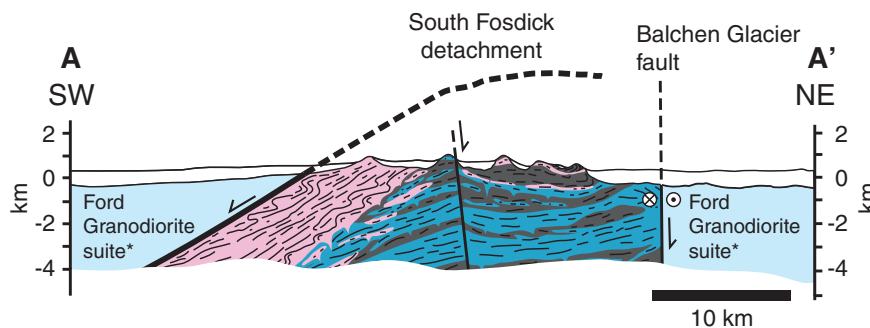
Fig. 2. SW–NE cross-section across the Fosdick migmatite–granite complex, illustrating schematic relationships between residual paragneiss, orthogneiss, and granite (modified from McFadden *et al.*, in preparation). *Ford Granodiorite suite is exposed at higher structural levels, and occupies the hanging walls along the South Fosdick detachment and the Balchen Glacier Fault. Byrd Coast Granite suite intrudes the Ford Granodiorite suite in other localities in the Ford Ranges, and both Ford Granodiorite suite and Byrd Coast Granite suite intrude the Swanson Formation. Rock types in the cross-section are the same as those shown in Fig. 1d.

Evidence for Devonian–Carboniferous metamorphism and crustal anatexis is preserved in the deepest structural levels in the complex (Korhonen *et al.*, 2007; Siddoway & Fanning, 2009). A comparison of preserved peak assemblages in the gneisses with forward mineral equilibria modeling of protolith compositions constrains conditions of Devonian–Carboniferous metamorphism to 820–870°C and 7·5–11·5 kbar (Korhonen *et al.*, 2009). These results also suggest that ∼4–25 vol. % melt was produced from the range of Swanson Formation compositions during this event, and that >70% of the melt generated must have been extracted; in contrast, the Ford Granodiorite suite is not a fertile source at these conditions.

A Cretaceous overprint on the residual gneisses is characterized by the growth of cordierite after garnet, and after biotite + sillimanite in garnet-absent domains. Mineral equilibria modeling of gneissic compositions constrains conditions of Cretaceous metamorphism to 830–870°C and 6–7·5 kbar, and shows that up to ∼12 vol. % melt could be produced from the residual compositions (Korhonen *et al.*, 2009). The Devonian–Carboniferous event is pervasively overprinted by the Cretaceous event at higher structural levels in the complex below the South Fosdick detachment zone (Korhonen *et al.*, 2007; McFadden *et al.*, in preparation). The elevated geotherms in a magmatic arc environment during the Devonian–Carboniferous allow the possibility that these higher structural levels remained subsolidus during the first event, and therefore, these protoliths could be fertile sources during the Cretaceous event (Korhonen *et al.*, 2009). U–Pb zircon ages from samples in dilatant transverse structures associated with the sheeted leucogranite complex confirm that this remnant melt network was active between *c.* 115 and 102 Ma (McFadden *et al.*, in preparation). The accumulation of granite may have caused initiation of the South Fosdick detachment, or alternatively the detachment zone may have acted as a rheological barrier that focused deformation and melt accumulation (McFadden *et al.*, in preparation), obscuring evidence of the older Devonian–Carboniferous history.

FIELD RELATIONS AND PETROGRAPHY OF GRANITES AND GNEISSES

To characterize the processes related to intracrustal differentiation during the two anatectic events, granite and migmatite samples were selected from different structural levels and rock units. Sample localities are shown in Fig. 1d.

Samples associated with residual paragneiss

Outcrops at Mt. Avers are dominated by stromatic metatexite migmatite with a vertical thickness and lateral extent exceeding 1000 m, providing the most extensive exposure of migmatitic paragneiss within the Fosdick migmatite–granite complex (Fig. 1d). The migmatites comprise discrete garnet–cordierite–sillimanite–biotite-bearing melanosome and quartz–plagioclase–K-feldspar–biotite ± garnet-bearing leucosome that range in thickness from a few millimeters to several centimeters (Korhonen *et al.*, 2007, 2009). Three samples of migmatitic paragneiss from Mt. Avers were analyzed in this study (K6-A07, K6-A22, and K6-A24; Fig. 1d).

Samples associated with the layered plutonic sequence

Samples of granite hosted in the layered plutonic sequence were collected from Mt. Avers (sample K6-A21b), Marujupu Peak (sample K6-Mj01) west of the residual paragneiss domain, and from Mt. Lockhart (samples K6-L09, -Ll0, -Ll1) to the east. Sample K6-A21b is a biotite granite occurring as an ∼100 m thick sill (Fig. 3f). The granite is undeformed with biotite schlieren parallel to the granite–gneiss contact. Sample K6-Mj01 is a 1 m thick garnet-bearing sill exposed along Ochs Glacier (Fig. 3c). The three samples from Mt. Lockhart were collected from the same heterogeneous granite body. The granite has a sharp, irregular contact with the host orthogneiss. Magmatic layering in the granite is defined by discrete compositional domains consisting of K-feldspar-, garnet-, and cordierite-rich layers. Late sillimanite schlieren are also common. Sample K9-L09 corresponds to a garnet-bearing layer, and samples K6-Ll0 and K6-Ll1 are from a cordierite-bearing layer. Sample K6-Ll2 is from the host orthogneiss.

Samples associated with the sheeted leucogranite complex

Several samples of granite and gneisses associated with the sheeted leucogranite complex were sampled across the Fosdick Mountains. To the west, sampled localities include SE Mt. Iphigene (samples C5-Is51A and C5-Is54), SW Mt. Iphigene (samples K6-I59b, K6-I60, K6-Mt38), and Thompson Ridge (sample K6-T35b). To the east, localities include Mt. Bitgood (samples K6-B26, -B27, -B48, and -B51) and Bird Bluff (samples K6-Bb44-47).

Sample C5-Is51A is a laterally continuous tabular body of gray orthoclase-porphyritic biotite monzogranite. Sensitive high-resolution ion microprobe (SHRIMP) chronology on this sample yields a U–Pb zircon age of 353·4 ± 3·2 Ma (Siddoway & Fanning, 2009). Sample C5-Is54 is a biotite granite sheet structurally below the detachment. It is part of the Ochs Glacier suite of McFadden *et al.* (in preparation) and has a SHRIMP U–Pb zircon age of 114·8 ± 1 Ma. Samples K6-I59b and K6-I60 were collected from a heterogeneous biotite granite body that is exposed over a large area of Mt. Iphigene. The granite has distinct layering defined by biotite- and
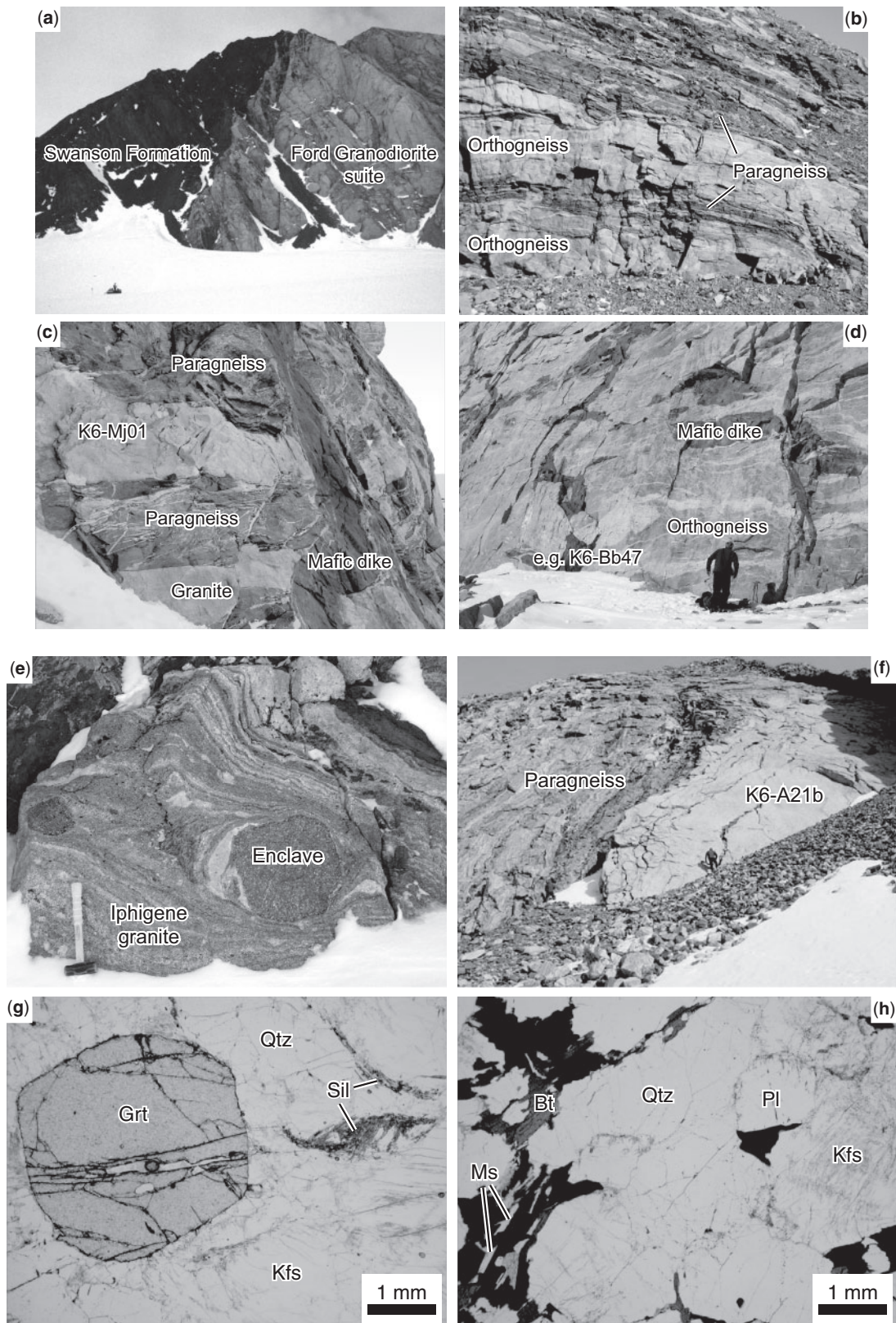
Fig. 3. Field photographs and representative granite petrography of components within the Fosdick migmatite–granite complex; geographical names and sample locations shown in Fig. 1b and c. (a) Contact relationship between the Ford Granodiorite suite and the Swanson

K-feldspar-rich layers at the outcrop scale, although the proportion of biotite increases significantly across the exposure. Biotite schollen and enclaves of granodiorite that have a weak foliation rotated with respect to the foliation of the host granite are common (Fig. 3e). To the west of this granite body, the proportion of migmatitic paragneiss in the sheeted leucogranite complex increases. Sample K6-Mt38 is from a large biotite monzogranite body intrusive into paragneiss. The granite is heterogeneous with biotite schlieren and mafic enclaves. Sample K6-T35b is another granite body that intrudes a domain of migmatitic paragneiss at Thompson Ridge, although, in contrast to sample K6-Mt38, this granite is more homogeneous.

The two granite bodies sampled in the eastern portion of the sheeted leucogranite complex are more homogeneous than the granites in the west. They contain significantly fewer schlieren and schollen, and typically form horizontal sheets. The granite sampled at Mt. Bitgood (sample K6-B27) is a massive and coarse-grained K-feldspar granite that intrudes orthogneiss and paragneiss. The granite contains small (2–5 mm) euhedral pristine garnet and sillimanite schlieren that define a weak foliation. The orthogneiss at this locality (sample K6-B26) is foliated and contains sparse leucosomes 1–3 cm in width. The leucosomes have petrological continuity (i.e. similar mineralogy, mode and grain size) with the quartzofeldspathic layers in the orthogneiss host and have meter-scale spacing in outcrop. Garnet is concentrated in the biotite-rich selvedge that separates the leucosome and paleosome, and is also present as euhedral grains in leucosomes. Stromatic migmatitic paragneiss on the west side of Mt. Bitgood was also sampled (K6-B48 and K6-B5l).

A similar granite phase is also present at Bird Bluff, where it intrudes foliated and weakly migmatitic orthogneiss. Veins and dikes ranging in thickness from 2 to 20 cm extend from the granite body into the host gneiss (Fig. 3d). The samples collected here (K6-Bb46 and K6-Bb47) are from different compositional layers in the same granite body. Sample K6-Bb46 is a garnet-bearing layer, and sample K6-Bb47 is a cordierite-bearing layer. The host orthogneiss was also sampled (K6-Bb45). Sample K6-Bb44 is a stromatic migmatitic paragneiss from a layer ∼l00 m north of the granite.

Other samples

Two granite samples were collected above the South Fosdick detachment. Sample C5-R23 is from a foliated body of coarse-grained granite at Mt. Richardson that is cross-cut by the detachment. Sample K6-NU0l is from a coarse-grained two-mica granite collected from the unnamed nunatak SW of Mt. Iphigene. Samples analyzed from outside the Fosdick Mountains include four Swanson Formation metasedimentary rocks from the Swanson Range (see Fig. lc for range locations), two Ford Granodiorite suite samples from the Denfield Mountains, and two Byrd Coast Granite suite samples from the Sarnoff Mountains.

Granite petrography

The analyzed granites from the Fosdick migmatite–granite complex generally consist of a coarse-grained interlocking matrix of quartz–plagioclase–K-feldspar. Quartz commonly has irregular grain boundaries and exhibits moderate development of subgrains. Biotite mode varies between granites, but where present it generally occurs as dark brown laths distributed throughout the matrix, and may also occur interstitially between quartz and feldspar. Sample K6-Mt38 contains distinctive brown biotite that is coarser and lighter in color than biotite in the other granites. Some granites exhibit a weak foliation defined by biotite and/or sillimanite schlieren. The granites can be broadly divided into two groups based on petrography. One group of granites contains quartz–plagioclase–K-feldspar–sillimanite ± biotite ± muscovite ± garnet ± cordierite (e.g. Fig. 3g), whereas the other group contains quartz–plagioclase–K-feldspar–biotite ± muscovite ± garnet (e.g. Fig. 3h). Both types of granite have zircon, apatite, opaque minerals and/or monazite as common accessory phases. A detailed description of the gneisses has been given by Korhonen *et al.* (2009).

ZIRCON U–Pb CHRONOLOGY

To investigate the timing of granite crystallization, zircon U–Pb chronology was undertaken using laser ablation inductively coupled plasma mass spectrometry (LA-ICP-MS) at the University of Maryland. Zircon grains were separated from eight granite samples within the complex and two samples of granite outside the

Formation; Mt. Dolber, Sarnoff Mountains. (b) Interlayered orthogneiss and paragneiss; Mt. Bitgood. People for scale in lower right. (c) Granite sill (sample K6-Mj0l) intrusive into paragneiss at Marujupu Peak; hammer for scale in lower left. Granite and host are cross-cut by a mafic dike of inferred Cretaceous age. (d) Small-scale granite body (similar phase to samples K6-Bb46, -Bb47) from Bird Bluff with veins that extend from the granite body into the host gneiss. Samples K6-Bb46 and K6-Bb47 were collected from a larger body ∼l00 m south of the photograph. (e) Granite body from Mt. Iphigene (samples K6-I59, -I60) with enclaves of granodiorite inferred to be Ford Granodiorite suite. (f) Granite sill (sample K6-A2lb) from Mt. Avers. (g) Photomicrograph of an exemplar granite comprising quartz–plagioclase–K-feldspar–sillimanite ± biotite ± muscovite ± garnet ± cordierite (sample K6-Bb46). (g) Photomicrograph of an exemplar granite comprising quartz–plagioclase–K-feldspar–biotite ± muscovite ± garnet (sample K6-T35b). Mineral abbreviations after Kretz (l983).

complex (Fig. 1d). The analyzed granites contain one of two types of zircon: Type I zircon occurs as prismatic and elongate euhedral grains with well-developed concentric oscillatory zoning; Type II zircon occurs as stubby to elongated, prismatic grains with distinctive cores that lack zoning. These two types of zircon morphology correlate with whole-rock chemistry as discussed below. Cathodoluminescence (CL) images of zircon grains indicating the analysis position and calculated $^{206}Pb/^{238}U$ ages are shown in Fig. 4. Tera–Wasserburg concordia diagrams are shown in Fig. 5. Representative analytical results are given in Table 1; the full data are available on request from the corresponding author. Analytical methods are given in the Appendix.

Granites with Type I zircon

Type I zircon grains have well-developed concentric oscillatory zoning, sometimes with overgrowths that may embay the zoned core (Fig. 4a–c and e). The age associated with the oscillatory zoning is interpreted to date the crystallization of the granite.

Two dominant crystallization ages are distinguished from granites with Type I zircon: K6-I60 (358 ± 8 Ma, $n = 5$), K6-A2lb (350 ± 10 Ma, $n = 8$), and K6-T35b (343 ± 8 Ma, $n = 5$) are Carboniferous; and K6-NU01 (119 ± 8 Ma, $n = 3$) and K6-Mt38 (114 ± 5 Ma, $n = 7$) are Cretaceous (reported ages are the mean and 2σ uncertainty of concordant analyses; Fig. 5a–d, j). Zircon grains from Carboniferous granites K6-I60 and K6-T35b also have overgrowths that yield concordant Cretaceous ages (c. 114–107 Ma from K6-T35b and c. 106 Ma from K6-I60; Figs 4b, c and 5b, c), suggestive of new growth or dissolution–reprecipitation during the Cretaceous event.

Zircon grains from sample C5-R23 have zoned cores with bright CL characteristics rimmed by a wide domain with oscillatory zoning and dark CL characteristics (Fig. 4j). Analyses from two grains yield a Carboniferous core and Cretaceous rim (Fig. 4j). Two rim analyses (c. 105 and 117 Ma) and one core analysis (c. 355 Ma) plot on concordia (Fig. 5e). These data are interpreted as the growth of Cretaceous magmatic zircon around a core inherited from the source.

Granites with Type II zircon

Type II zircon grains contain distinctive cores that lack zoning. Grains from three granite samples (K6-Mj01, K6-B27, K6-Bb47) have dusty cores with dark CL characteristics mantled by clear rims with oscillatory growth zoning (Fig. 4d, f and g). Zircon rims from sample K6-Bb47 yield concordant Cretaceous ages (109 ± 2 Ma, $n = 5$; Fig. 5h), and zircon rims from sample K6-Mj01 yield slightly younger ages (102 ± 3 Ma, $n = 4$; Fig. 5f). These ages are interpreted to date the crystallization of the granite. The dusty cores yield discordant ages (Fig. 5f and h). Zircons from sample K6-B27 are small grains less

than 0·2 mm in length (Fig. 4f). Analyses on rims yield ages ranging from Carboniferous to Cretaceous (Fig. 4f), and the data are scattered in the Tera–Wasserburg diagram (Fig. 5g). Five concordant rim analyses yield a mean age of 336 ± 12 Ma (Fig. 5g), suggestive of zircon growth or dissolution–reprecipitation during the Carboniferous event.

Zircon grains from sample K6-Ll0 have bright cores in CL rimmed by a wide overgrowth with dark CL characteristics (Fig. 4h). $^{206}Pb/^{238}U$ ages from the cores are Proterozoic in age (c. 2003–586 Ma). Three concordant core analyses suggest inheritance from an older crustal source (Fig. 5i). Four analyses from rims yield concordant $^{206}Pb/^{238}U$ ages ranging from the Devonian to the Cretaceous (c. 400–98 Ma; Fig. 5i). This zircon yielded no dominant age population.

The analyzed zircons from samples K6-B27 and K6-Ll0 yield poorly defined or ambiguous crystallization ages. However, these two granite samples are argued to be Cretaceous based on chemical constraints presented below; an interpretation also compatible with field observations and the structural context of these samples.

GEOCHEMISTRY

Major and trace element compositions were determined on 15 granites, three orthogneisses and four paragneisses within the Fosdick migmatite–granite complex, four Swanson Formation metasedimentary rocks, two Ford Granodiorite suite samples, and three Byrd Coast Granite suite samples. Melanosome and leucosome components from five paragneiss migmatite and one orthogneiss migmatite were separated and analyzed separately. Sample locations are shown in Fig. 1d.

Major and trace elements were analyzed by X-ray fluorescence spectrometry (XRF) at Franklin & Marshall College following their standard procedures (Boyd & Mertzmann, 1987). FeO contents were analyzed by Fe^{2+} titration and Fe_2O_3 contents were calculated by difference. Anhydrous values normalized to 100% are used in the text and figures for all major element data. Chemical compositions determined by XRF are listed in Table 2.

Trace elements, including the rare earth elements (REE) were analyzed by inductively coupled plasma mass spectrometry (ICP-MS) at the University of Maryland and are listed in Table 3, with a detailed description of the analytical procedures outlined in the Appendix. Replicate analyses from separate dissolutions commonly show some variability in absolute trace element and REE abundances, reflecting minor heterogeneity in the sample powder; however, relative abundances between replicate analyses remain consistent. The full set of analyses is available on request from the corresponding author.
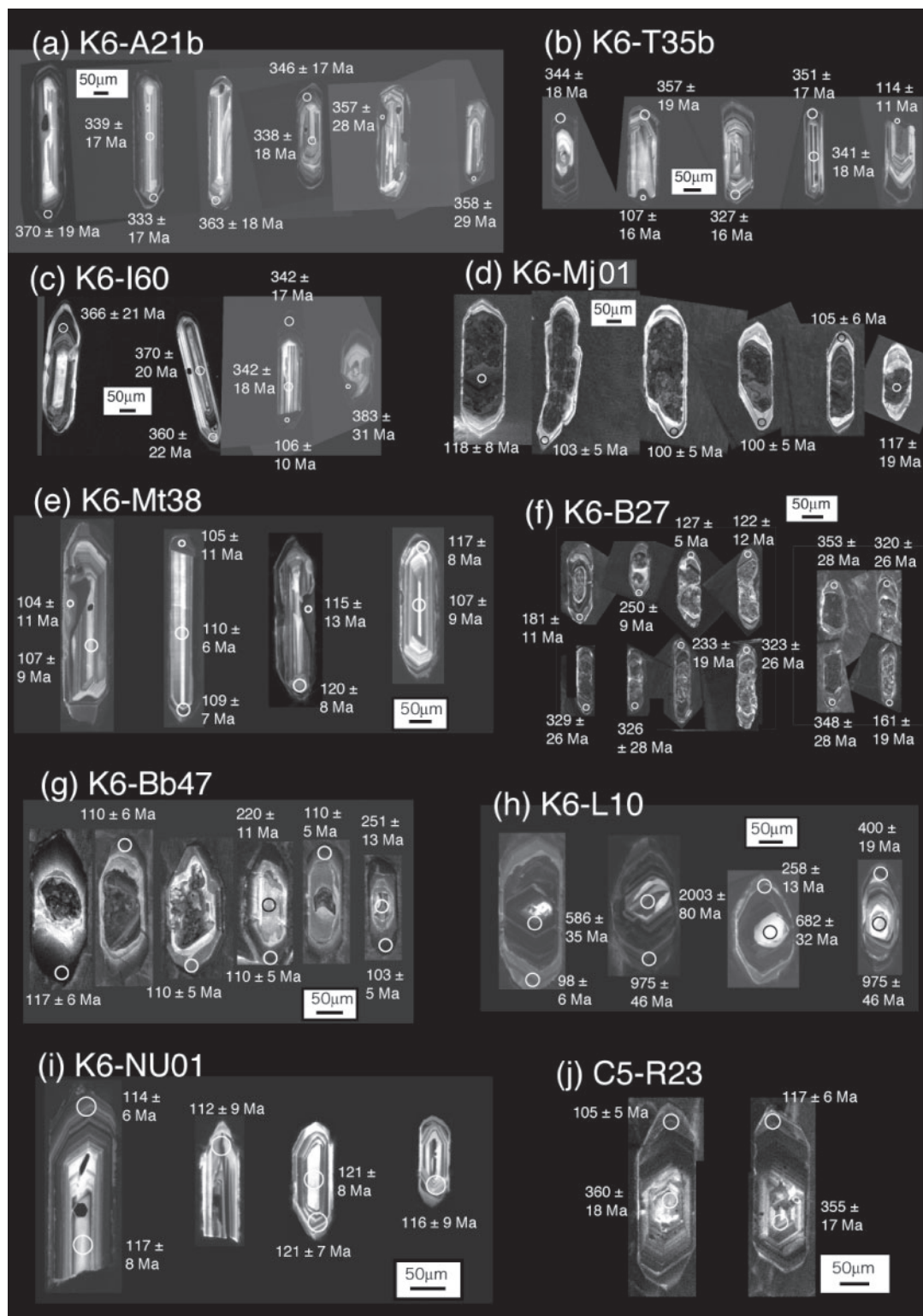
Fig. 4. Cathodoluminescence images of zircon grains. Circles indicate the position of analysis points. Ages shown are [206]Pb/[238]U ages determined by LA-ICP-MS.
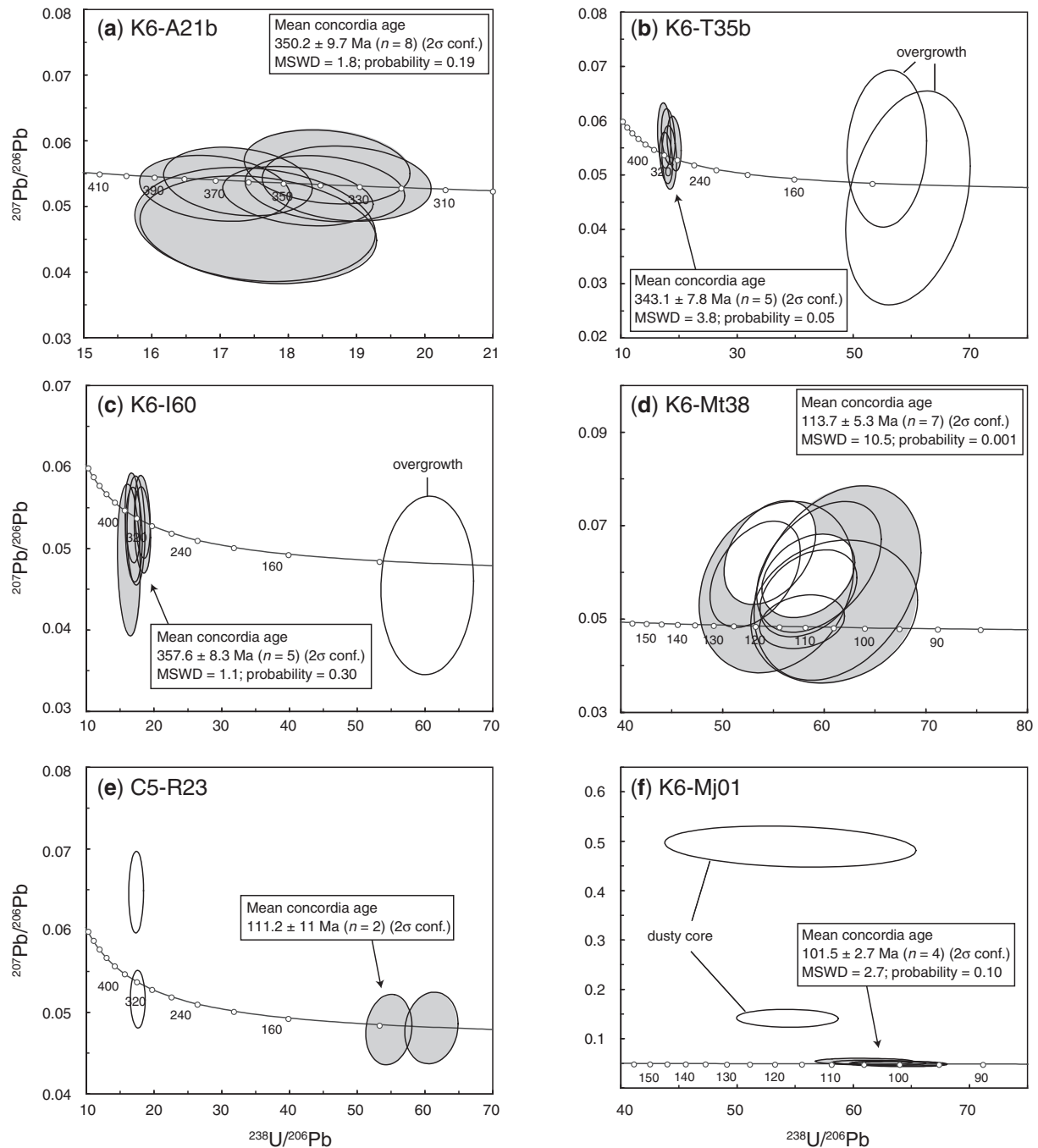
Fig. 5. Tera–Wasserburg concordia diagrams for LA-ICP-MS zircon U–Pb data. Data point error ellipses are at the 2σ confidence level, which includes U decay constant uncertainty. Shaded ellipses are used for the mean concordia age calculation. (g) Carboniferous concordia age for K6-B27 interpreted as inherited age based on low Zr content and thin rims that yield Cretaceous ages.

Major and trace element compositions

Potential source rocks exposed in the Ford Ranges

Potential source rocks for the granites and migmatites are the regionally exposed Ford Granodiorite suite and Swanson Formation metasedimentary rocks. The Ford Granodiorite suite has normalized SiO_2 contents of 65–76 wt %, and is metaluminous to peraluminous with aluminum saturation index (ASI = molar [Al_2O_3/(CaO + Na_2O + K_2O)]) values between 0·85 and 1·16 (this study; Weaver *et al.*, 1991; D. Kimbrough, unpublished data).
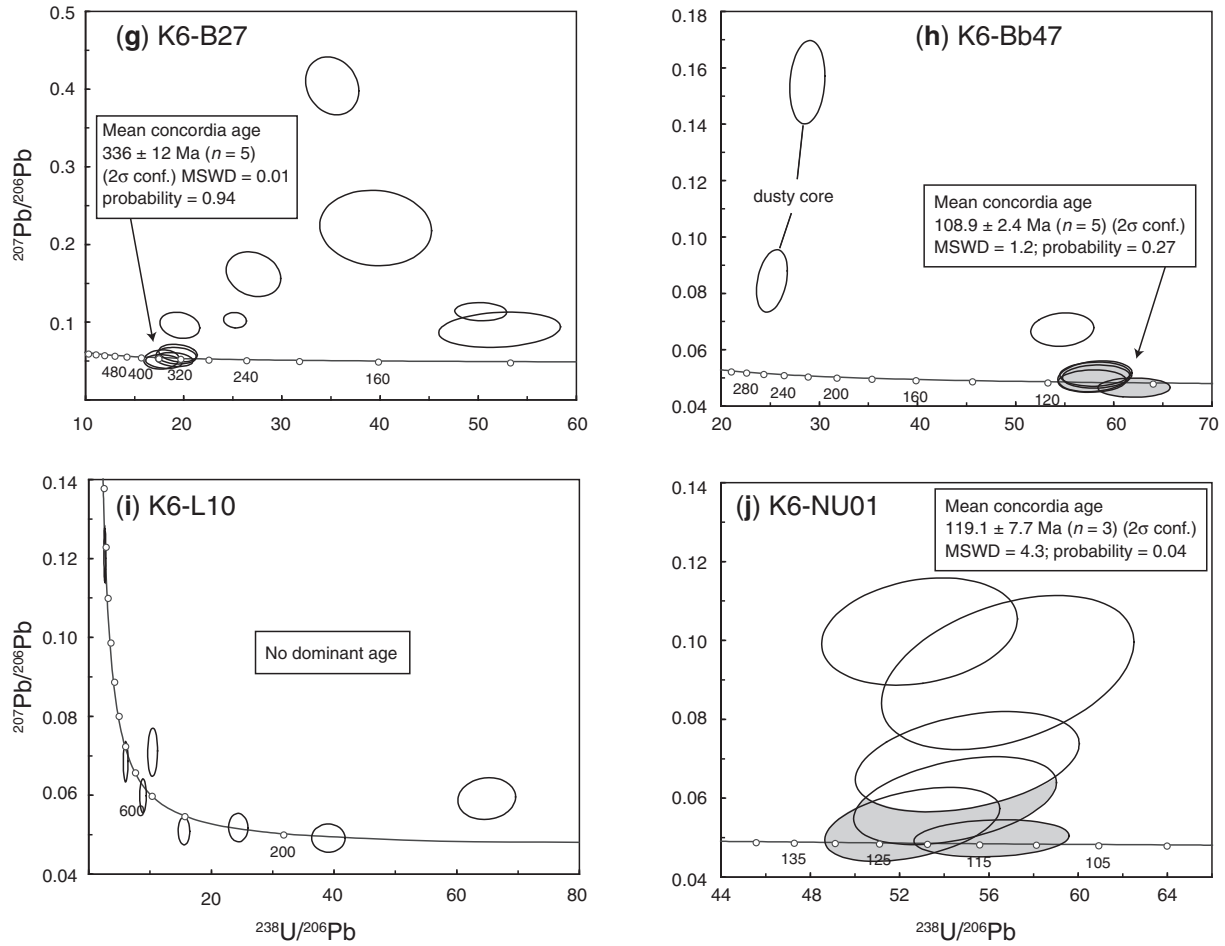
Fig. 5. Continued.

Table 1: Representative LA-ICP-MS U–Pb zircon data from granites

Spot	Spot size (μm) and location		Radiogenic atomic ratios						
			$^{207}Pb/^{235}U$	2σ	$^{206}Pb/^{238}U$	2σ	$^{207}Pb/^{206}Pb$	2σ	rho*
K6-I60 (low Rb/Sr granite, Type I zircon)									
Sp11a23	30	rim	0·4040	0·041	0·0544	0·0028	0·0538	0·0042	0·670
Sp11a25	30	core	0·3921	0·042	0·0545	0·0029	0·0522	0·0043	0·638
No26a13	15	overgrowth	0·1037	0·022	0·0166	0·0015	0·0454	0·0089	0·388
K6-T35b (low Rb/Sr granite, Type I zircon)									
Sp11a43	30	rim	0·4094	0·041	0·0559	0·0028	0·0530	0·0039	0·706
Sp11a45	30	core	0·3985	0·044	0·0544	0·0030	0·0531	0·0048	0·599
No26a17	15	overgrowth	0·1352	0·031	0·0179	0·0018	0·0547	0·0118	0·345
K6-A21b (low Rb/Sr granite, Type I zircon)									
Sp11a63	30	rim	0·3913	0·038	0·0551	0·0027	0·0515	0·0037	0·708
Sp11a65	30	core	0·4152	0·044	0·0538	0·0029	0·0559	0·0046	0·643

(continued)

Table 1: Continued

Spot	Spot size (μm) and location		Radiogenic atomic ratios						
			$^{207}Pb/^{235}U$	2σ	$^{206}Pb/^{238}U$	2σ	$^{207}Pb/^{206}Pb$	2σ	rho*
C5-R23 (low Rb/Sr granite, Type I zircon)									
No26b04	30	rim	0·1205	0·010	0·0183	0·0009	0·0478	0·0035	0·499
No26b06	30	core	0·4019	0·031	0·0565	0·0028	0·0515	0·0029	0·681
K6-Mt38 (low Rb/Sr granite, Type I zircon)									
No26c18	30	rim	0·1541	0·022	0·0188	0·0013	0·0595	0·0093	0·023
No26c140	30	core	0·1306	0·017	0·0171	0·0011	0·0554	0·0076	0·134
K6-Mj01 (LREE-depleted granite, Type II zircon)									
Sp11a75	30	rim	0·1118	0·012	0·0161	0·0008	0·0505	0·0040	0·666
Sp11a105	30	core	0·3563	0·045	0·0184	0·0012	0·1405	0·0148	0·552
mK6-B27 (LREE-depleted granite, Type II zircon)									
No26c154	15	rim	0·3699	0·066	0·0524	0·0043	0·0511	0·0074	0·618
No26c160	15	rim	0·3972	0·082	0·0562	0·0046	0·0512	0·0101	0·319
K6-Bb47 (LREE-depleted granite, Type II zircon)									
No26c136	30	rim	0·1160	0·009	0·0173	0·0008	0·0487	0·0032	0·553
No26c138	30	core	0·7397	0·064	0·0347	0·0018	0·1547	0·0121	0·455
K6-L10 (LREE-depleted granite, Type II zircon)									
No26c38	30	core	6·0648	0·423	0·3645	0·0169	0·1207	0·0057	0·743
No26c134	30	rim	0·1252	0·011	0·0154	0·0009	0·0590	0·0043	0·586
K6-NU01 (Byrd Coast Granite suite)									
No26c116	30	rim	0·1396	0·018	0·0190	0·0012	0·0532	0·0077	0·001
No26c120	30	core	0·1498	0·021	0·0183	0·0013	0·0592	0·0091	0·038

Spot	Apparent age (Ma)								
	$^{207}Pb/^{235}U$	2σ	$^{206}Pb/^{238}U$	2σ	$^{207}Pb/^{206}Pb$	2σ	Concordia age	2σ	MSWD
K6-I60 (low Rb/Sr granite, Type I zircon)									
Sp11a23	345	29	342	17	363	170	341	17	0·07
Sp11a25	336	30	342	18	294	184	342	18	0·26
No26a13	100	20	106	10	0	374	106	10	0·37
K6-T35b I60 (low Rb/Sr granite, Type I zircon)									
Sp11a43	348	29	351	17	331	161	351	17	0·06
Sp11a45	341	32	341	18	335	198	341	18	0·00
No26a17	129	27	114	11	401	450	115	11	1·20
K6-A21b I60 (low Rb/Sr granite, Type I zircon)									
Sp11a63	335	28	346	17	262	161	347	17	1·11
Sp11a65	353	31	338	18	449	178	337	17	1·40
C5-R23 (low Rb/Sr granite, Type I zircon)									
No26b04	116	9	117	6	0	352	117	6	0·09
No26b06	343	22	355	17	265	125	353	17	2·00
K6-Mt38 (low Rb/Sr granite, Type I zircon)									
No26c18	145	19	120	8	585	322	124	8	6·00
No26c140	125	15	109	7	429	293	112	7	3·70

(continued)

Table 1: Continued

Spot	Apparent age (Ma)								
	$^{207}Pb/^{235}U$	2σ	$^{206}Pb/^{238}U$	2σ	$^{207}Pb/^{206}Pb$	2σ	Concordia age	2σ	MSWD
K6-Mj01 (LREE-depleted granite, Type II zircon)									
Sp11a75	108	11	103	5	217	177	102	5	1·50
Sp11a105	309	33	117	8	2233	177	discordant		
K6-B27 (LREE-depleted granite, Type II zircon)									
No26c154	320	49	329	26	247	316	330	26	0·25
No26c160	340	59	353	28	249	425	352	28	0·21
K6-Bb47 (LREE-depleted granite, Type II zircon)									
No26c136	111	8	110	5	132	153	111	5	0·08
No26c138	562	37	220	11	2398	130	discordant		
K6-L10 (LREE-depleted granite, Type II zircon)									
No26c38	1985	60	2003	80	1966	83	1986	61	0·46
No26c134	120	10	98	6	567	156	discordant		
K6-NU01 (Byrd Coast Granite suite)									
No26c116	133	16	121	7	339	310	123	7	1·60
No26c120	142	18	117	8	576	317	121	7	6·00

*Ratio between the relative standard deviation between $^{207}Pb/^{235}U$ and $^{206}Pb/^{235}U$ ratios.

Table 2: Whole-rock and component (XRF) compositions

Rock type:	Carboniferous low Rb/Sr granite				High Rb/Sr	Cretaceous granite, Type I zircon				Cretaceous LREE-depleted granite		
Sample no.:	K6-A21b	K6-I59	K6-I60	K6-T35b	C5-Is51A	C5-Is54	C5-R23	K6-Mt38	K6-B27	K6-Bb46	K6-Bb47
wt %											
SiO_2	71·26	72·23	70·53	71·99	69·31	71·22	74·47	70·31	74·45	75·16	75·15
TiO_2	0·21	0·23	0·41	0·37	0·49	0·25	0·15	0·39	0·03	0·02	0·02
Al_2O_3	15·09	14·93	14·62	14·64	15·13	14·58	14·02	15·09	14·76	13·84	14·10
Fe_2O_3	0·60	0·17	0·53	0·73	0·64	0·27	0·15	0·66	0·17	0·35	0·03
FeO	0·78	1·38	2·41	1·67	2·47	1·43	0·63	1·98	0·50	0·31	0·45
MnO	0·02	0·02	0·03	0·04	0·05	0·03	0·02	0·02	0·08	0·05	0·01
MgO	0·53	0·58	1·26	0·88	1·10	0·53	0·22	1·32	0·09	0·11	0·15
CaO	1·67	2·04	2·03	2·04	1·33	1·46	1·14	2·09	0·81	0·83	1·05
Na_2O	3·18	4·08	3·79	4·00	3·27	3·62	3·62	3·27	3·14	2·58	2·71
K_2O	5·65	3·53	3·11	2·73	4·93	5·24	5·10	3·78	5·53	6·30	5·72
P_2O_5	0·07	0·13	0·18	0·13	0·24	0·20	0·09	0·11	0·11	0·16	0·18
LOI	0·54	0·59	0·72	0·57	0·95	0·67	0·48	0·87	0·39	0·44	0·59
Total	99·60	99·91	99·62	99·79	99·91	99·50	100·09	99·89	100·06	100·15	100·16
ASI	1·05	1·05	1·10	1·11	1·15	1·02	1·03	1·14	1·17	1·10	1·12
ppm											
Rb	155·8	131·4	153·9	158·4	283·5	223·2	171·6	151·2	147·1	185·4	182
Sr	332	363	325	258	108	283	248	264	95	159	207
Y	7·4	7·5	12·6	11·2	19·8	14·3	7·7	6·7	7·9	4·4	1·5

Table 2: Continued

Rock type:	Carboniferous low Rb/Sr granite				High Rb/Sr	Cretaceous granite, Type I zircon			Cretaceous LREE-depleted granite		
Sample no.:	K6-A21b	K6-I59	K6-I60	K6-T35b	C5-Is51A	C5-Is54	C5-R23	K6-Mt38	K6-B27	K6-Bb46	K6-Bb47
Zr	181	165	165	159	185	137	117	193	35	72	30
V	19	30	57	40	52	33	16	59	6	7	7
Ni	3	9	13	6	14	5	5	11	2	5	4
Cr	10	28	70	20	71	42	23	121	4	27	27
Nb	4·5	6·7	12·7	12·9	16·7	15·5	6·6	12·4	1	1·4	2·4
Ga	12·5	15·7	17·6	16·9	21·3	17	13·7	18·5	14·6	11·7	13·6
Cu	<1	<2	<1	<1	<2	<2	<2	24	<1	9	2
Zn	24	43	59	47	99	71	28	69	3	17	18
Co	<1	2	3	1	9	3	<1	8	<1	<1	<1
Ba	745	508	460	415	413	639	663	608	155	370	410
La	33	25	24	28	29	32	21	28	11	10	8
Ce	76	53	49	61	64	60	46	57	10	7	9
U	1·6	2·5	1·9	4·3	4·2	2·8	1·5	1·3	0·7	2·6	1·3
Th	20·4	9·8	7·6	10·9	14·2	18·6	7·7	8·5	<0·5	2·6	2·9
Sc	4	8	10	9	10	7	3	9	5	4	1
Pb	40	40	34	27	27	43	34	33	50	65	58
T_{Zr} (M)	798	785	790	786	814	773	761	808	681	729	665
T_{Zr} (FM)	803	789	759	772	778	773	782	777	699	752	685
T_{Zr} (K)	818	803	775	787	795	785	790	795	694	753	680

Rock type:	Cretaceous LREE-depleted granite				Ford Granodiorite suite		Byrd Coast Granite suite			Swanson Formation	
Sample no.:	K6-L09	K6-L10	K6-L11	K6-Mj01	912-2A	9N27-4	9D12-2	9D12-JS	K6-NU01	K6-SR29	K6-SR30
wt %											
SiO_2	73·61	73·67	73·86	74·30	72·68	66·34	75·14	78·17	75·18	61·35	63·14
TiO_2	0·03	0·07	0·04	0·02	0·27	0·68	0·09	0·06	0·08	0·70	0·78
Al_2O_3	15·07	14·89	15·13	13·94	13·88	15·91	13·38	12·02	14·29	17·39	15·53
Fe_2O_3	0·78	0·06	0·16	0·44	0·29	0·39	0·07	0·08	0·74	1·53	2·93
FeO	0·61	0·43	0·30	1·20	1·42	3·08	1·26	0·51	0·29	4·74	3·20
MnO	0·12	0·01	0·02	0·23	0·04	0·06	0·06	0·01	0·14	0·08	0·07
MgO	0·17	0·24	0·18	0·28	0·35	1·66	0·09	0·03	0·11	3·57	3·38
CaO	1·22	0·96	1·43	1·39	1·11	3·67	0·87	0·79	0·49	1·05	1·58
Na_2O	3·32	3·29	3·77	2·69	3·61	3·92	3·54	3·53	4·21	1·29	1·69
K_2O	4·71	5·99	4·41	4·68	5·05	2·82	4·95	3·95	3·99	4·32	3·53
P_2O_5	0·13	0·13	0·12	0·10	0·13	0·21	0·05	0·07	0·12	0·13	0·19
LOI	0·43	0·58	0·73	0·76	1·04	1·22	0·48	0·44	0·70	4·26	4·29
Total	100·20	100·32	100·15	100·03	99·87	99·96	99·98	99·66	100·34	100·41	100·31
ASI	1·18	1·09	1·11	1·16	1·03	0·98	1·05	1·04	1·18	2·00	1·64
ppm											
Rb	127·4	176·2	133·3	126·1	272·3	121·1	253	198·1	370·4	215·5	170·6
Sr	90	147	133	298	111	399	34	54	46	95	112
Y	11·5	3·4	5·2	29·4	33·1	17·7	96·7	30·6	21·6	26·6	38·2
Zr	41	78	63	49	185	187	118	39	54	113	166
V	10	16	9	6	29	75	9	5	15	113	101
Ni	11	3	4	1	4	13	1	2	3	42	38

(continued)

Table 2: Continued

Rock type:	Cretaceous LREE-depleted granite				Ford Granodiorite suite		Byrd Coast Granite suite			Swanson Formation	
Sample no.:	K6-L09	K6-L10	K6-L11	K6-Mj01	912-2A	9N27-4	9D12-2	9D12-JS	K6-NU01	K6-SR29	K6-SR30
Cr	60	58	36	3	54	55	34	17	25	100	85
Nb	1·2	3·2	1·6	0·7	23·1	14	29·6	11·9	38·4	12	14·9
Ga	13·8	13	13·5	9·4	16·5	16·3	16·2	13·3	24·9	22·6	19·3
Cu	2	<2	<2	12	<2	<2	<2	<2	<2	29	20
Zn	16	21	14	8	53	66	41	24	64	113	91
Co	<1	<1	<1	<1	1	11	<1	<1	<1	17	14
Ba	163	363	210	903	438	594	162	107	88	595	592
La	11	14	14	13	34	19	33	15	15	30	31
Ce	11	16	15	21	71	50	63	19	18	65	73
U	1	1·7	1·2	2·1	2·1	0·7	7·7	8·4	2·9	0·9	1·3
Th	1·6	3·1	1·5	2·4	18·8	7·4	22	7·8	7·5	14·3	13·4
Sc	4	3	1	10	6	11	9	4	13	15	13
Pb	60	58	54	55	22	11	45	41	7	<1	17
T_{Zr} (M)	698	758	739	706	822	756	790	701	730	—	—
T_{Zr} (FM)	690	736	716	699	802	785	764	675	716	—	—
T_{Zr} (K)	701	755	738	706	807	736	782	704	731	—	—

Rock type:	Swanson Formation		Paragneiss						Leucosome in paragneiss		
Sample no.:	K6-SR31	K6-SR32	K6-A07	K6-A22	K6-A24	K6-B48	K6-B51	K6-Bb44	K6-A22	K6-A24	K6-B48
wt %											
SiO_2	69·10	67·83	74·11	64·81	72·16	71·83	70·27	67·34	70·49	76·62	72·49
TiO_2	0·69	0·71	0·68	0·98	0·76	0·33	0·68	0·84	0·29	0·10	0·14
Al_2O_3	12·81	13·63	11·23	16·66	12·98	14·02	13·66	14·57	15·55	11·89	14·45
Fe_2O_3	0·72	0·54	1·14	1·27	1·29	0·80	1·49	1·18	0·32	0·19	1·07
FeO	3·91	4·74	3·40	5·64	3·59	1·94	3·93	4·99	1·62	1·79	1·48
MnO	0·08	0·07	0·06	0·09	0·06	0·06	0·08	0·06	0·02	0·06	0·11
MgO	2·59	3·64	2·26	3·50	2·40	1·16	2·46	3·22	0·85	0·72	0·80
CaO	1·96	1·96	1·64	0·82	0·97	1·03	0·97	1·07	1·25	1·18	1·12
Na_2O	1·94	1·65	2·15	1·08	1·09	2·87	1·97	1·64	2·26	1·56	3·05
K_2O	2·40	2·88	2·18	3·51	3·00	4·38	3·07	2·69	5·96	4·57	4·21
P_2O_5	0·19	0·18	0·14	0·09	0·15	0·11	0·09	0·16	0·20	0·21	0·12
LOI	4·00	2·34	0·97	1·83	1·84	1·26	1·67	2·34	0·87	1·39	1·09
Total	100·39	100·17	99·96	100·28	100·29	99·79	100·34	100·10	99·68	100·28	100·13
ASI	1·37	1·45	1·26	2·36	1·91	1·24	1·64	1·93	1·25	1·23	1·24
ppm											
Rb	117·7	135	131·5	203	160·7	187·6	240·4	238·8	180·9	136·1	153·1
Sr	136	199	159	133	128	136	110	110	361	261	150
Y	31·7	30·5	29·2	30·5	28	17	39·6	30·9	12·9	28·4	29·7
Zr	247	171	302	212	249	136	223	178	84	57	119
V	82	103	98	144	97	57	89	123	44	17	34
Ni	30	22	52	55	37	13	35	37	26	9	4
Cr	70	143	150	124	73	41	70	98	27	12	39
Nb	12	13·4	12·7	18·1	13·1	15·1	18·6	17·3	6·8	2·7	5·8
Ga	13·9	16	12·7	25·4	15·4	15·7	20·2	20·8	11·4	6·1	14·4

(continued)

Table 2: Continued

Rock type:	Swanson Formation		Paragneiss						Leucosome in paragneiss		
Sample no.:	K6-SR31	K6-SR32	K6-A07	K6-A22	K6-A24	K6-B48	K6-B51	K6-Bb44	K6-A22	K6-A24	K6-B48
Cu	8	14	29	13	5	5	3	20	41	4	8
Zn	76	79	94	150	92	60	105	133	46	30	39
Co	12	17	16	26	13	<1	15	14	4	2	<1
Ba	480	570	397	598	625	572	460	344	1467	1356	575
La	30	27	22	27	24	29	25	32	15	13	30
Ce	76	58	56	64	59	55	59	63	34	18	63
U	3·3	1·6	1·1	2·4	3·1	4·5	5·3	3·6	1·5	0·5	3·8
Th	12·3	10·4	13·3	11·3	9·5	12·9	9·9	13·2	6·7	3·7	9·9
Sc	12	13	12	16	10	7	15	17	3	7	12
Pb	4	7	16	14	18	32	12	<1	49	51	37

Rock type:	Leucosome in paragneiss		Melanosome in paragneiss					Orthogneiss			Leucosome
Sample no.:	K6-B51	K6-Bb44	K6-A22	K6-A24	K6-B48	K6-B51	K6-Bb44	K6-B26	K6-Bb45	K6-L12	K6-B26
wt %											
SiO_2	73·19	73·25	57·82	68·69	63·93	70·03	65·84	66·54	73·99	72·25	68·43
TiO_2	0·09	0·10	1·51	1·34	1·35	1·24	1·04	0·72	0·22	0·24	0·04
Al_2O_3	15·13	14·84	18·65	13·39	14·92	11·40	14·44	16·33	14·32	14·85	15·66
Fe_2O_3	0·30	0·73	0·95	0·74	0·65	0·40	1·15	1·06	0·10	0·34	0·21
FeO	0·67	0·87	8·70	5·78	6·64	7·12	6·26	3·09	1·17	1·53	1·42
MnO	0·02	0·04	0·09	0·04	0·05	0·04	0·06	0·04	0·01	0·04	0·08
MgO	0·44	0·80	5·23	3·78	4·27	3·89	3·76	1·58	0·53	0·59	0·37
CaO	2·13	2·25	0·31	0·46	0·61	0·20	0·71	3·44	0·98	1·60	2·42
Na_2O	4·60	3·59	0·38	0·60	1·43	0·45	1·12	3·84	2·99	3·69	2·60
K_2O	2·52	2·16	3·70	3·12	3·63	3·18	3·18	1·97	5·23	4·23	6·59
P_2O_5	0·11	0·25	0·09	0·08	0·06	0·05	0·11	0·22	0·16	0·12	1·12
LOI	1·00	1·54	2·98	2·04	2·68	1·87	2·61	0·81	0·54	0·59	0·72
Total	100·20	100·42	100·41	100·06	100·22	99·87	100·28	99·64	100·24	100·07	99·66
ASI	1·07	1·20	3·59	2·57	2·02	2·51	2·20	1·11	1·16	1·10	0·99
ppm											
Rb	93·7	95·2	255·1	215·6	340·6	373·5	294·7	149·4	196·6	162·7	211·1
Sr	211	253	44	64	52	23	85	317	99	253	330
Y	13·7	23·5	45·7	18·7	16	35·5	29·9	17·1	6·6	9·7	78·9
Zr	45	22	281	349	357	371	213	255	98	108	16
V	13	27	185	154	161	138	142	75	24	28	7
Ni	8	1	74	59	60	64	46	14	8	9	<1
Cr	6	15	145	121	155	101	124	37	50	28	4
Nb	3·7	1·7	25·4	21·8	61·2	27·9	19·7	18·9	11·8	10·3	1·4
Ga	13·5	9·9	32·9	22·8	35·6	26·8	21·6	19·9	20	15·7	12·5
Cu	<2	9	24	2	14	6	18	1	<2	4	11
Zn	24	29	208	153	224	187	166	90	55	53	20
Co	<1	<1	36	25	19	29	19	7	<1	3	<1

(continued)

Table 2: Continued

Rock type:	Leucosome in paragneiss		Melanosome in paragneiss					Orthogneiss			Leucosome
Sample no.:	K6-B51	K6-Bb44	K6-A22	K6-A24	K6-B48	K6-B51	K6-Bb44	K6-B26	K6-Bb45	K6-L12	K6-B26
Ba	464	588	446	475	252	305	323	532	259	543	1350
La	18	14	27	26	34	31	35	33	22	17	22
Ce	29	24	73	70	82	70	69	90	39	28	51
U	3·1	1·9	3·7	2·6	6·4	5·5	3·7	1·8	4·1	1·9	1·6
Th	5·1	1·1	19·7	16·3	20·1	17·8	15·3	7·7	12	7·7	2·2
Sc	3	5	19	11	12	17	20	12	4	10	6
Pb	33	19	1	5	<1	<1	<1	15	44	36	26

FeO by Fe^{2+} titration; Fe_2O_3 by difference; T_{Zr} (M), (FM), zircon saturation thermometer (Watson & Harrison, 1983) using *M*, *FM* (see text); T_{Zr} (K), from Kelsey *et al.* (2008).

Table 3: Whole-rock and component (ICP-MS) compositions

Rock type:	Carboniferous low Rb/Sr granite				High Rb/Sr	Cretaceous granite, Type I zircon			Cretaceous LREE-depleted granite		
Sample no.:	K6-A21b*	K6-I59	K6-I60*	K6-T35b	C5-Is51A*	C5-Is54	C5-R23	K6-Mt38*	K6-B27	K6-Bb46	K6-Bb47
ppm											
Sc	4·38	3·7	8·58	8·5	5·29	3·2	1·9	4·63	5·0	3·72	0·6
V	10·64	14·8	45·30	31·1	31·05	14·6	6·0	37·05	0·4	0·46	0·4
Cr	6·37	6·2	24·43	14·3	17·82	4·5	1·8	10·54	0·3	0·17	0·2
Co	2·73	2·5	5·98	4·3	4·94	2·5	0·8	5·28	0·4	10·41	0·4
Ni	5·63	8·2	13·28	9·2	10·17	4·7	2·6	7·40	2·3	2·34	1·9
Rb	147·52	117·6	113·34	146·6	196·12	139·3	143·0	53·89	131·1	179·76	173·6
Sr	308·21	319·5	251·59	239·8	74·10	200·8	183·8	100·67	73·4	136·03	174·0
Y	8·37	8·8	13·84	10·9	18·55	12·1	8·3	6·14	8·1	10·41	2·1
Zr	174·85	76·6	241·50	67·8	190·50	92·8	73·7	203·66	18·1	48·59	5·4
Nb	4·99	6·0	10·48	11·4	16·98	12·9	5·7	12·36	0·8	0·95	1·7
Cs	1·95	5·24	4·67	8·44	6·88	2·85	3·36	2·12	0·88	5·45	6·90
Ba	647·52	422·35	328·19	370·77	266·56	602·33	643·07	334·52	159·86	302·81	411·14
Hf	5·06	2·19	6·76	2·20	4·97	3·11	2·63	5·48	0·93	1·98	0·23
Ta	0·23	0·84	1·15	1·18	1·71	1·03	0·66	0·76	0·04	0·21	0·34
Th	23·44	8·5	9·03	12·7	15·25	18·4	12·5	6·53	0·8	0·76	0·1
U	2·94	2·7	2·44	4·6	4·31	2·9	2·9	1·38	1·1	3·55	1·5
La	52·13	23·47	23·37	35·86	30·21	29·58	22·39	15·81	4·03	3·55	2·12
Ce	104·63	46·70	48·54	71·55	66·96	58·50	46·67	35·66	6·91	5·62	3·61
Pr	12·29	5·14	5·61	7·42	8·20	6·07	5·26	4·03	0·70	0·57	0·29
Nd	40·76	18·26	20·45	29·60	30·97	23·29	18·85	15·58	2·25	1·92	0·90
Sm	7·47	3·39	3·94	5·01	6·42	4·60	3·69	3·23	0·48	0·46	0·21
Eu	1·26	0·85	0·84	0·97	0·79	0·79	0·81	0·69	0·37	0·71	0·76
Gd	6·38	3·07	3·69	4·42	5·68	4·40	3·30	2·96	0·53	0·60	0·24

(continued)

Table 3: *Continued*

Rock type:	Carboniferous low Rb/Sr granite				High Rb/Sr	Cretaceous granite, Type I zircon			Cretaceous LREE-depleted granite		
Sample no.:	K6-A21b*	K6-I59	K6-I60*	K6-T35b	C5-Is51A*	C5-Is54	C5-R23	K6-Mt38*	K6-B27	K6-Bb46	K6-Bb47
Tb	0·63	0·43	0·51	0·55	0·72	0·60	0·43	0·36	0·12	0·14	0·05
Dy	2·30	2·09	2·72	2·47	3·56	2·90	1·95	1·59	1·09	1·16	0·32
Ho	0·31	0·34	0·47	0·42	0·63	0·48	0·33	0·23	0·28	0·27	0·07
Er	0·76	0·86	1·23	1·06	1·71	1·22	0·87	0·54	1·08	1·04	0·21
Tm	0·07	0·11	0·16	0·12	0·23	0·14	0·11	0·06	0·22	0·24	0·03
Yb	0·45	0·67	1·05	0·72	1·44	0·90	0·78	0·44	1·77	2·29	0·23
Lu	0·07	0·09	0·15	0·10	0·20	0·12	0·12	0·07	0·28	0·39	0·03
Eu/Eu*	0·54	0·79	0·66	0·61	0·39	0·53	0·69	0·67	2·20	4·12	10·15
La_N/Lu_N	81·85	25·98	15·79	37·53	15·53	25·10	19·51	24·89	1·51	0·96	6·89
Tb_N/Lu_N	6·52	3·10	2·25	3·75	2·43	3·35	2·44	3·76	0·29	0·26	1·03
Rb/Sr	0·48	0·37	0·45	0·61	2·65	0·69	0·78	0·54	1·79	1·32	1·00

Rock type:	Cretaceous LREE-depleted granite				Ford Granodiorite suite		Byrd Coast Granite suite			Swanson Formation	
Sample no.:	K6-L09	K6-L10	K6-L11	K6-Mj01	912–2A	9N27-4	9D12-2	9D12-JS	K6-NU01	K6-SR29	K6-SR30
ppm											
Sc	7·1	1·5	0·9	13·31	6·8	7·3	6·40	3·0	8·40	17·83	14·07
V	0·8	5·6	1·3	1·24	13·4	57·3	1·70	0·4	3·48	128·62	94·37
Cr	2·2	2·3	1·4	1·66	2·6	21·4	0·47	-0·1	0·76	97·12	77·65
Co	1·0	1·1	0·6	1·55	2·1	8·6	0·53	0·3	0·58	16·10	10·35
Ni	3·7	3·6	2·9	6·22	3·7	15·0	3·48	1·6	3·48	43·82	38·11
Rb	129·1	162·6	114·5	117·62	244·4	109·3	242·99	191·8	303·46	218·95	168·33
Sr	77·2	123·1	100·2	266·39	89·6	358·0	24·80	49·6	29·08	88·36	97·35
Y	14·5	5·3	3·4	38·16	33·3	19·3	115·37	32·4	19·97	32·15	39·71
Zr	10·2	38·9	31·0	15·27	112·5	125·2	95·17	21·2	42·18	111·35	105·71
Nb	0·5	2·6	1·3	1·22	24·4	14·3	32·27	11·3	36·34	14·67	16·08
Cs	1·35	1·67	2·02	2·34	12·15	5·91	8·67	6·65	12·53	12·12	8·34
Ba	163·51	353·18	203·41	745·49	399·20	479·58	75·60	64·43	68·20	587·95	499·24
Hf	0·54	1·35	1·27	0·64	3·50	3·19	3·87	1·25	2·17	2·96	2·92
Ta	0·06	0·18	0·11	0·22	3·28	1·03	1·35	1·23	3·43	1·09	1·11
Th	3·5	3·9	1·6	1·59	15·0	7·5	23·25	5·9	5·88	14·51	12·89
U	1·1	1·5	1·5	3·98	2·8	1·7	7·58	8·7	3·41	1·98	1·85
La	7·99	9·07	6·58	5·01	30·14	23·16	30·08	8·19	5·55	40·87	35·26
Ce	17·83	19·73	12·34	9·10	67·68	47·29	77·41	17·86	17·46	79·06	72·97
Pr	2·17	2·22	1·35	0·97	6·82	5·25	8·42	2·15	2·06	9·36	8·39
Nd	7·73	7·81	4·66	3·37	26·99	21·23	32·38	7·90	7·95	36·15	33·64
Sm	1·89	1·75	1·07	0·79	5·77	4·20	8·94	2·40	3·06	6·93	7·17
Eu	0·46	0·75	0·57	1·24	0·82	1·19	0·30	0·40	0·13	1·32	1·41
Gd	1·75	1·66	0·98	1·01	5·72	4·25	10·37	2·89	2·90	6·84	7·18
Tb	0·31	0·24	0·14	0·28	0·94	0·59	2·03	0·69	0·56	0·96	1·08
Dy	2·22	1·15	0·71	3·52	5·66	3·34	15·11	5·06	3·50	5·55	6·54
Ho	0·52	0·18	0·11	1·20	1·09	0·65	3·41	1·07	0·60	1·08	1·29

(continued)

Table 3: Continued

Rock type:	Cretaceous LREE-depleted granite				Ford Granodiorite suite		Byrd Coast Granite suite			Swanson Formation	
Sample no.:	K6-L09	K6-L10	K6-L11	K6-Mj01	912–2A	9N27-4	9D12-2	9D12-JS	K6-NU01	K6-SR29	K6-SR30
Er	1·85	0·48	0·32	5·44	3·23	1·92	10·47	3·45	1·66	3·17	3·73
Tm	0·42	0·06	0·05	1·20	0·50	0·27	1·59	0·59	0·28	0·46	0·53
Yb	3·76	0·35	0·36	10·22	3·45	1·85	10·33	4·24	2·00	3·04	3·43
Lu	0·60	0·05	0·05	1·73	0·49	0·27	1·50	0·61	0·28	0·44	0·48
Eu/Eu*	0·76	1·32	1·67	4·23	0·43	0·85	0·10	0·47	0·13	0·58	0·59
La_N/Lu_N	1·39	19·92	13·35	0·30	6·34	8·89	2·08	1·40	2·08	9·58	7·58
Tb_N/Lu_N	0·36	3·41	1·88	0·11	1·29	1·48	0·92	0·77	1·38	1·48	1·52
Rb/Sr	1·67	1·32	1·14	0·44	2·73	0·31	9·80	3·87	10·43	2·48	1·73

Rock type:	Swanson Formation		Paragneiss						Leucosome in paragneiss		
Sample no.:	K6-SR31	K6-SR32	K6-A07*	K6-A22	K6-A24*	K6-B48	K6-B51	K6-Bb44	K6-A22	K6-A24	K6-B48
ppm											
Sc	11·2	15·43	9·83	15·71	11·24	7·27	13·98	14·5	3·31	7·61	10·90
V	76·2	108·69	72·21	120·23	83·28	38·92	77·29	108·5	32·53	8·86	16·43
Cr	66·4	142·27	79·08	84·25	64·83	35·93	61·16	94·6	22·14	7·95	17·40
Co	13·0	16·99	11·12	18·41	12·46	5·64	12·58	16·5	9·11	3·01	3·59
Ni	29·8	94·41	38·56	41·05	31·70	16·76	32·68	38·8	19·48	7·46	10·87
Rb	111·4	150·62	76·14	183·65	136·57	173·79	224·35	234·7	167·91	121·20	140·20
Sr	119·9	205·24	107·75	116·86	105·84	111·30	92·76	92·4	321·36	222·20	118·07
Y	31·5	37·10	30·63	31·02	31·84	19·09	36·30	27·5	15·48	30·11	34·61
Zr	102·2	142·76	249·81	9·45	259·73	18·96	15·76	31·0	6·32	3·06	14·89
Nb	12·2	15·91	12·10	19·54	14·00	15·60	19·54	18·6	5·77	1·56	5·97
Cs	6·29	9·92	2·97	5·80	3·08	2·16	4·55	9·29	2·64	0·97	1·37
Ba	429·58	516·71	172·56	497·85	461·48	466·29	363·37	301·19	1331·32	1137·43	452·13
Hf	3·24	3·78	6·15	0·35	6·73	0·64	0·51	0·95	0·20	0·11	0·51
Ta	1·01	1·07	0·71	1·39	0·98	0·71	1·30	1·53	0·43	0·14	0·30
Th	13·7	12·97	11·41	19·26	14·11	14·35	14·75	15·3	5·81	2·84	15·55
U	3·8	3·01	2·09	4·16	3·05	4·60	6·17	4·0	1·84	1·09	5·06
La	42·85	36·53	30·90	56·19	40·02	39·37	40·91	44·17	20·46	11·25	42·49
Ce	86·88	75·14	66·19	114·50	84·56	79·16	84·11	89·43	41·75	23·15	86·00
Pr	9·87	8·56	7·98	14·32	10·27	9·41	10·37	10·27	4·98	2·92	10·32
Nd	38·81	34·15	29·38	50·45	36·99	33·43	36·15	41·23	19·27	10·92	36·15
Sm	7·49	7·06	5·82	10·34	7·52	6·47	7·44	7·88	4·12	2·53	7·21
Eu	1·36	1·51	1·25	1·54	1·38	0·99	1·12	1·07	2·67	2·16	1·03
Gd	7·28	7·05	5·61	9·82	7·30	5·83	7·24	7·35	4·10	2·78	6·62
Tb	1·04	1·01	0·78	1·23	1·00	0·73	1·01	1·05	0·58	0·51	0·93
Dy	5·82	5·99	4·70	6·21	5·63	3·60	5·97	5·30	3·07	4·01	5·41
Ho	1·14	1·18	0·99	1·06	1·09	0·63	1·18	0·97	0·51	0·96	1·10
Er	3·30	3·40	3·01	2·82	3·02	1·77	3·41	2·65	1·24	3·08	3·39
Tm	0·46	0·49	0·46	0·36	0·42	0·25	0·48	0·34	0·14	0·49	0·52
Yb	2·99	3·16	3·07	2·21	2·69	1·57	3·00	2·02	0·81	3·19	3·32
Lu	0·42	0·44	0·46	0·31	0·39	0·22	0·42	0·28	0·11	0·46	0·47

(continued)

Table 3: Continued

Rock type:	Swanson Formation		Paragneiss						Leucosome in paragneiss		
Sample no.:	K6-SR31	K6-SR32	K6-A07*	K6-A22	K6-A24*	K6-B48	K6-B51	K6-Bb44	K6-A22	K6-A24	K6-B48
Eu/Eu^*	0·56	0·65	0·66	0·46	0·56	0·48	0·46	0·42	1·96	2·47	0·45
La_N/Lu_N	10·61	8·55	7·03	18·62	10·69	18·46	10·20	16·24	19·22	2·56	9·46
Tb_N/Lu_N	1·69	1·55	1·17	2·69	1·76	2·24	1·65	2·54	3·57	0·77	1·36
Rb/Sr	0·93	0·73	0·71	1·57	1·29	1·56	2·42	2·54	0·52	0·55	1·19

Rock type:	Leucosome in paragneiss		Melanosome in paragneiss					Orthogneiss			Leucosome
Sample no.:	K6-B51	K6-Bb44	K6-A22*	K6-A24*	K6-B48*	K6-B51*	K6-Bb44*	K6-B26*	K6-Bb45	K6-L12	K6-B26
ppm											
Sc	1·84	2·15	17·36	10·87	11·79	15·71	14·47	11·14	3·8	5·1	6·67
V	8·28	10·48	184·77	140·13	144·27	128·98	125·13	62·74	10·4	16·8	4·49
Cr	5·48	8·07	131·05	107·11	148·25	99·11	97·71	23·75	8·5	9·6	2·54
Co	1·86	3·00	26·08	18·47	18·95	20·66	17·30	7·85	2·4	2·6	1·62
Ni	8·13	8·55	57·82	42·63	53·57	50·11	42·10	17·86	5·2	7·0	6·85
Rb	90·17	91·39	129·53	175·28	274·09	232·35	202·78	120·67	191·4	91·4	189·23
Sr	186·03	222·80	24·92	52·63	35·00	16·89	54·92	276·80	89·3	169·9	295·40
Y	16·63	18·48	38·52	22·82	15·55	30·81	27·69	17·10	8·6	7·5	80·66
Zr	9·90	2·67	203·90	392·18	385·55	329·05	234·62	217·24	53·7	36·4	4·44
Nb	2·60	2·52	28·33	22·21	64·12	28·92	20·64	17·27	11·3	9·1	1·23
Cs	0·84	3·21	5·18	4·29	6·98	6·19	10·51	5·70	5·34	3·32	2·47
Ba	360·12	442·27	251·69	301·73	153·83	159·01	188·71	380·92	233·45	495·22	1188·94
Hf	0·30	0·10	5·17	9·86	10·37	8·31	5·98	5·29	1·77	1·38	0·24
Ta	0·21	0·22	1·74	1·58	3·01	1·71	1·42	0·85	0·58	0·84	0·11
Th	6·15	2·36	19·79	19·86	19·44	17·72	18·05	5·64	16·0	5·2	0·60
U	3·27	1·36	4·37	3·69	7·23	6·39	4·28	2·04	5·4	1·5	2·31
La	21·97	10·05	58·13	55·12	49·33	50·45	51·26	29·16	28·82	11·25	20·20
Ce	42·95	21·07	121·39	115·12	101·80	107·06	104·75	62·79	63·47	25·71	53·89
Pr	4·92	2·69	15·33	13·93	12·30	13·14	12·86	7·25	7·00	2·91	7·79
Nd	18·28	10·28	55·75	49·75	42·70	47·14	45·13	27·14	28·46	10·70	33·43
Sm	3·71	2·54	11·28	9·93	8·72	9·38	9·15	4·93	6·69	2·39	10·29
Eu	1·78	1·61	0·97	1·05	0·45	0·55	0·82	1·53	0·68	0·63	1·92
Gd	3·66	2·72	10·69	9·21	7·80	8·86	8·43	4·60	5·36	2·19	11·72
Tb	0·51	0·47	1·38	1·11	0·93	1·13	1·06	0·58	0·63	0·33	2·28
Dy	2·90	3·11	7·27	5·08	3·86	5·82	5·39	3·08	2·29	1·69	13·40
Ho	0·55	0·61	1·34	0·80	0·53	1·05	0·95	0·58	0·33	0·29	2·38
Er	1·53	1·65	3·68	1·93	1·24	2·85	2·55	1·63	0·80	0·81	5·83
Tm	0·21	0·23	0·48	0·22	0·13	0·37	0·32	0·21	0·08	0·11	0·75
Yb	1·23	1·43	3·00	1·44	0·87	2·35	2·05	1·34	0·42	0·74	4·24
Lu	0·17	0·19	0·44	0·22	0·13	0·34	0·29	0·20	0·05	0·10	0·52
Eu/Eu^*	1·46	1·85	0·26	0·33	0·16	0·18	0·28	0·96	0·34	0·82	0·53
La_N/Lu_N	13·46	5·42	13·77	26·38	38·16	15·26	18·07	15·48	58·69	11·12	3·99
Tb_N/Lu_N	2·06	1·67	2·15	3·49	4·72	2·24	2·45	2·04	8·43	2·14	2·96
Rb/Sr	0·48	0·41	5·20	3·33	7·83	13·76	3·69	0·44	2·14	0·54	0·64

*Powder digestion in Teflon bomb; otherwise digestion in $HF–HNO_3$ acid only (see Appendix).
Subscript N indicates normalized to chondrite.

TiO_2, Al_2O_3, $(FeO^* + MgO)$, CaO, Ba and Sr are negatively correlated with SiO_2, whereas K_2O, Rb and ASI values exhibit a positive correlation, and Na_2O is relatively constant across the range of SiO_2 contents (Figs 6 and 7). The two Ford Granodiorite suite samples analyzed in this study have similar REE concentrations and similarly shaped chondrite-normalized REE patterns (Fig. 8). These patterns are smooth and straight to slightly concave-upward in the heavy REE (HREE: Tb–Lu). The least fractionated sample in this study (9N27-4) has a small negative Eu anomaly (Eu/$Eu^* = 0.85$), whereas a more fractionated sample (9l2–2A) has a more pronounced negative Eu anomaly (Eu/$Eu^* = 0.43$). These results are similar to those reported by Weaver *et al.* (1992).

The Swanson Formation metasedimentary rocks exhibit some major element compositional variability with SiO_2 contents ranging from 63 to 76 wt % (this study; unpublished data). Al_2O_3, $(FeO^* + MgO)$, K_2O, ASI, Ba, Rb and ASI values decrease with increasing SiO_2, whereas TiO_2, CaO, Na_2O and Sr are relatively constant for variable SiO_2 contents (Figs 6, 7). Swanson Formation rocks span a limited range in both absolute and relative abundances of the REE, with smooth to slightly concave-downward light REE and middle REE (LREE and MREE; La–Gd) patterns and smooth to slightly concave-upward HREE patterns (Fig. 8). All samples have negative Eu anomalies (Eu/$Eu^* = 0.56$–0.65) and the overall shape and steepness of the REE patterns are similar to those of the North American shale composite (Taylor & McLennan, 1985).

Carboniferous granites

Carboniferous granites have normalized SiO_2 contents of 69–72 wt %, and are peraluminous with ASI values between 1.05 and 1.15 (Fig. 6; Table 2). TiO_2 and $(FeO^* + MgO)$ generally decrease with increasing SiO_2, whereas Na_2O, CaO, and Sr increase slightly with increasing SiO_2, and Al_2O_3, K_2O, Rb, and Ba show no correlation with SiO_2 (Fig. 6). Zr contents are elevated (>150 ppm; Fig. 7) and correspond to the presence of Type I zircon. Within the Carboniferous age group, the granites can be distinguished based on their Rb and Sr contents (Fig. 6). Four of the granites have Rb/Sr ratios <1.0, whereas one Carboniferous granite (sample C5-Is5lA) has an elevated Rb/Sr ratio (>2.5). As discussed below, the variations in chemistry reflect different petrogenesis and derivation from two different sources.

The Carboniferous granites show broadly similar chondrite-normalized REE patterns with variable Eu anomalies (Fig. 8). The four granites with low Rb/Sr ratios have similar LREE patterns with smooth to slightly concave-upward trends. Granite K6-A2lb has the steepest overall chondrite-normalized REE pattern with the highest concentrations of LREE and the steepest HREE slope with a Tb_N/Lu_N (where subscript N indicates normalized

to chondrite) ratio of 6.5. The granite sample with the elevated Rb/Sr ratio (sample C5-Is5lA) shows the most negative Eu anomaly (Eu/$Eu^* = 0.39$) of the Carboniferous age group (Table 3). The overall shape and steepness of these patterns are similar to those for the Ford Granodiorite suite and Swanson Formation metasedimentary rocks.

Cretaceous granites

Two groups of Cretaceous granites are identified based on their trace element and REE compositions. One group of granites (K6-Mt38, C5-Is54, and C5-R23) is characterized by low Rb/Sr ratios (<1.0) and elevated Zr contents (>100 ppm), corresponding to the presence of Type I zircon. These granites have normalized SiO_2 contents of ~71–75 wt %, and are peraluminous with ASI values between 1.02 and 1.14 (Fig. 6; Table 2). TiO_2, $(FeO^* + MgO)$, Al_2O_3, and CaO decrease with increasing SiO_2, whereas Na_2O increases slightly with increasing SiO_2, and K_2O shows no correlation with SiO_2, although the sample with the lowest SiO_2 content also has the lowest K_2O contents (Fig. 6). Ba, Sr, and Rb content generally increase with SiO_2 (Fig. 7).

The other group of granites ($n = 6$; from three separate granite bodies) typically has higher Rb/Sr ratios (1.0–1.8), low Th (<5 ppm) and Zr contents (<80 ppm,), and Type II zircon. One sample (K6-Mj0l) has a low Rb/Sr ratio (~0.4) and high Ba contents (745 ppm; Fig. 7), but otherwise plots with the granites with Type II zircon, possibly suggesting that this granite has a slightly different petrogenesis. These granites have broadly similar major element compositions with normalized SiO_2 contents of ~74–75 wt %. They are peraluminous with ASI values between 1.09 and 1.18. TiO_2, Na_2O, and Al_2O_3 decrease with increasing SiO_2, whereas K_2O, Rb, Sr, and Ba increase slightly with increasing SiO_2, and $(FeO^* + MgO)$ and CaO show no correlation with SiO_2 (Figs 6 and 7).

The chondrite-normalized REE patterns of the Cretaceous granites are distinct, with two types consistent with the grouping described above (Fig. 8). The granites with Type I zircon have the highest LREE concentrations with overall patterns similar to the Carboniferous granites. Granites with Type II zircon are generally REE depleted and have smooth LREE and MREE patterns. With the exception of one sample from Mt. Lockhart (K6-L09), the granites have prominent, positive Eu anomalies (Eu/$Eu^* = 1.32$–10.15). The presence of garnet in some samples is reflected by enrichment in the HREE and the positive slope of the HREE pattern ($Tb_N/Lu_N = 0.11$–0.36). Garnet-absent samples have flat to shallow HREE slopes ($Tb_N/Lu_N = 1.03$–$3.4l$) with low HREE concentrations. Garnet has a first-order control on the HREE concentrations in the granites. The three samples (K6-L09, -Ll0, -Ll1) from a heterogeneous granite body at Mt. Lockhart have chondrite-normalized REE similar to the
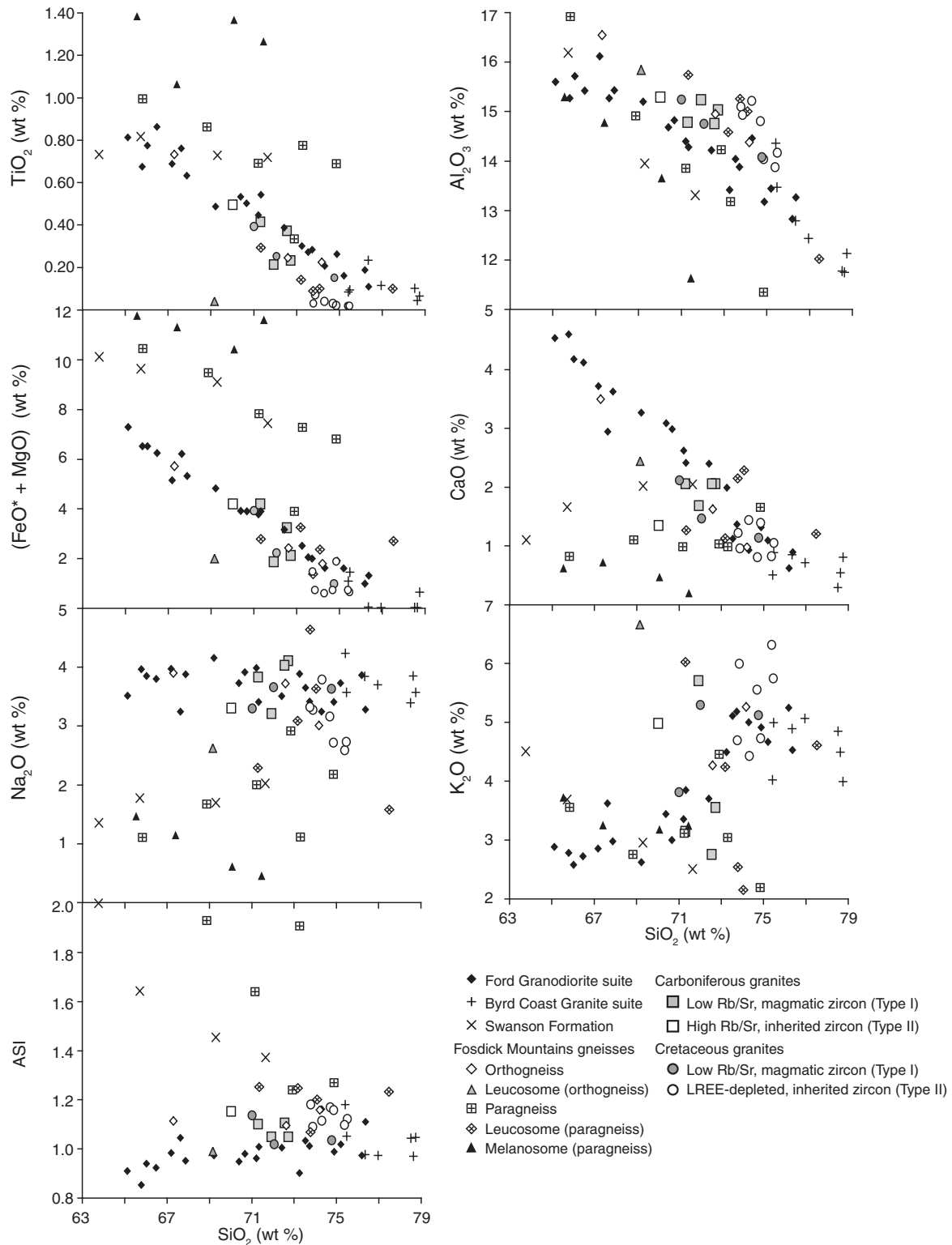
Fig. 6. Selected major element data for rocks in the Ford Ranges and Fosdick migmatite–granite complex determined by XRF. Data for Ford Granodiorite suite and Byrd Coast Granite suite also include data from Weaver *et al.* (1991), Kimbrough (unpublished data); those for Swanson Formation include data from Siddoway (unpublished data). Aluminum saturation index (ASI) = molar [Al$_2$O$_3$/(CaO + Na$_2$O + K$_2$O)].
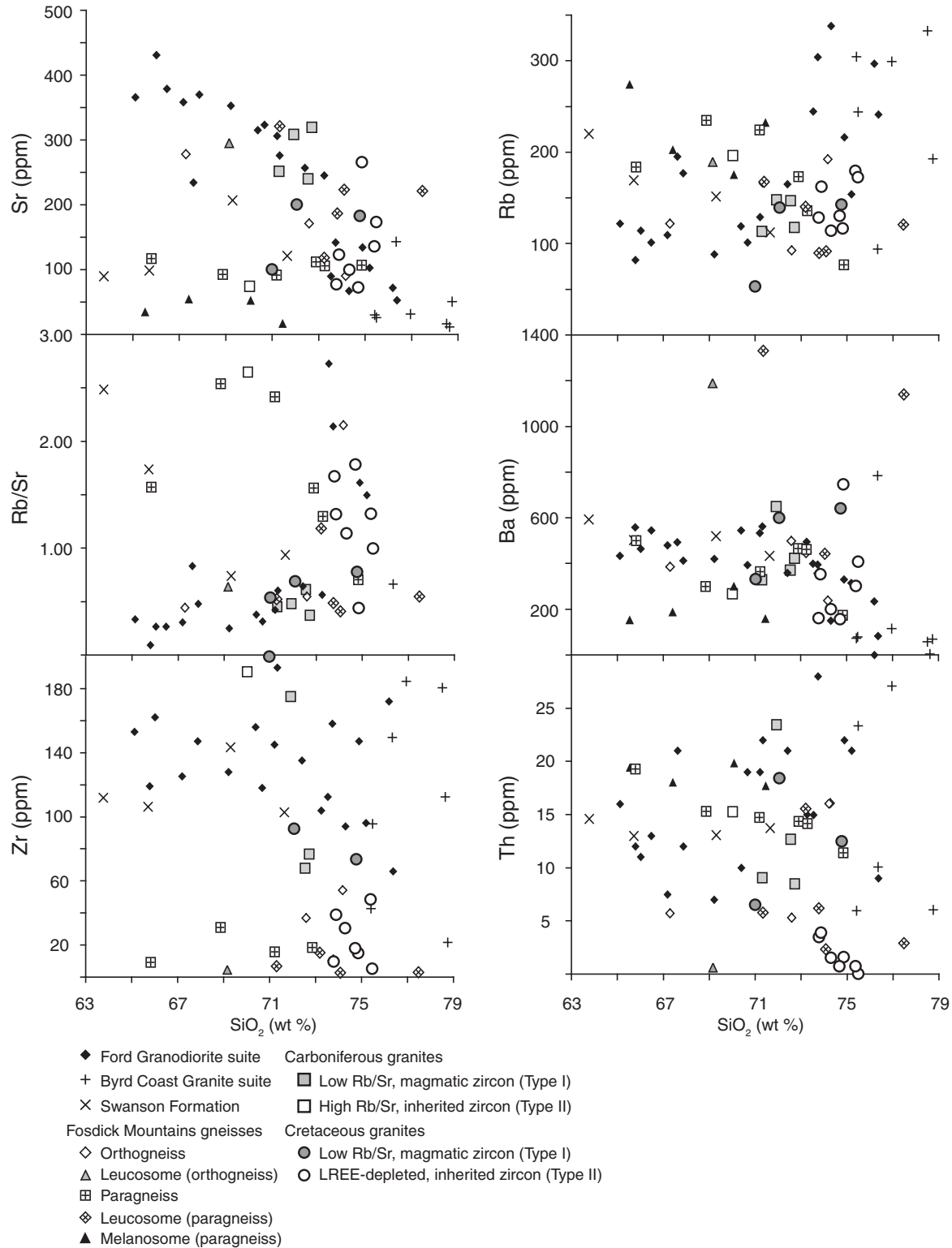
Fig. 7. Selected trace element and REE data for rocks in the Ford Ranges and Fosdick migmatite–granite complex determined by ICP-MS. Data for Ford Granodiorite suite and Byrd Coast Granite suite also include data from Weaver *et al.* (1991) and Kimbrough (unpublished data); those for Swanson Formation include data from Siddoway (unpublished data). Trace element contents determined by XRF and ICP-MS are listed in Tables 2 and 3, respectively.
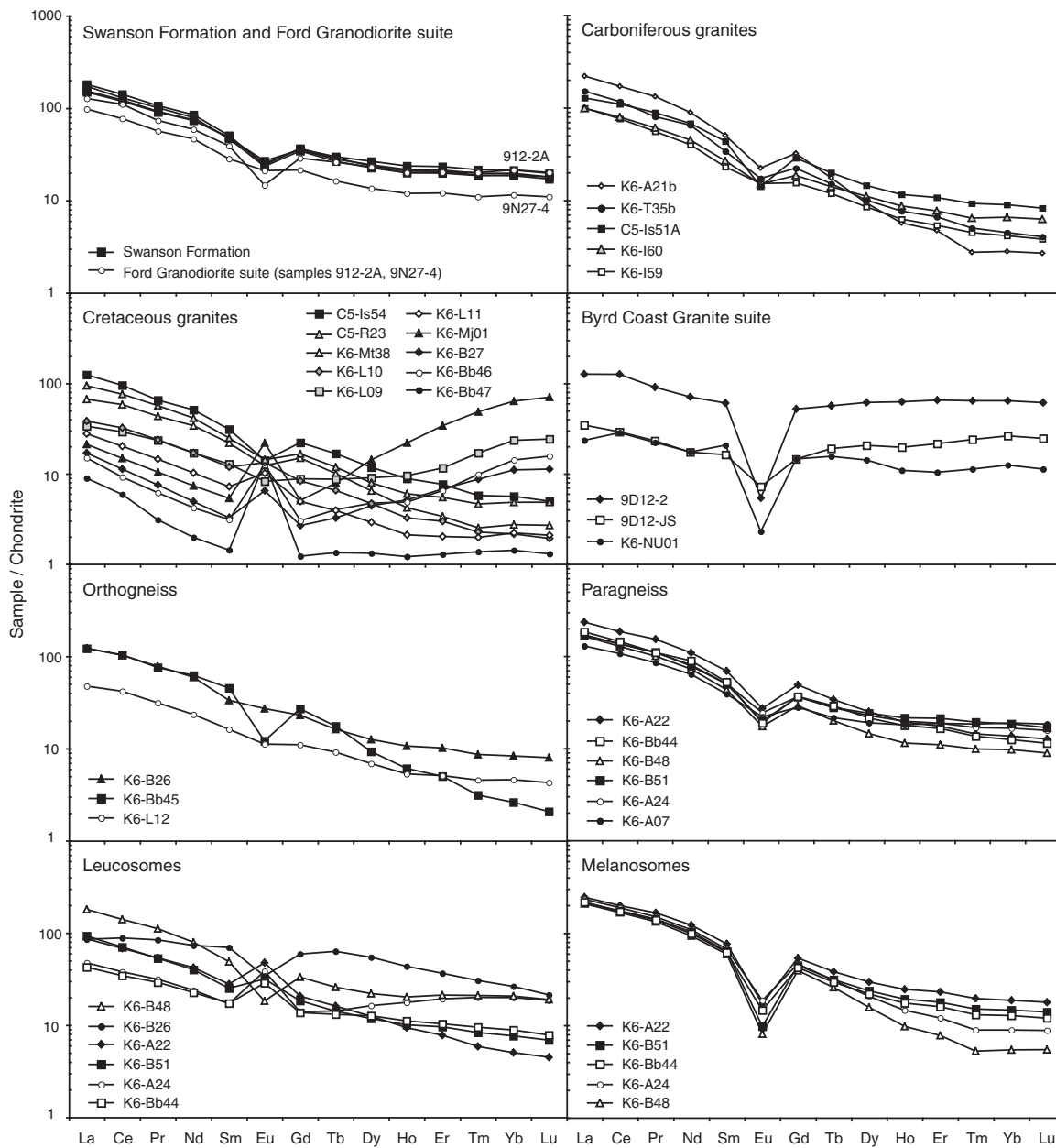
Fig. 8. Chondrite-normalized REE patterns for source rocks, granites, gneisses, and separated migmatite components (determined by ICP-MS; Table 3).

Cretaceous granites in the sheeted leucogranite complex, although the Eu anomalies are less prominent (Eu/Eu* = 0·76–1·67). The REE patterns of the Mt. Lockhart samples provided permissive evidence that these granites were generated during the Cretaceous.

Byrd Coast Granite suite

Samples from the Byrd Coast Granite suite have normalized SiO_2 contents of 74–79 wt %. Granite compositions are metaluminous to slightly peraluminous with ASI values between 0·96 and 1·18 (this study; Weaver *et al.*, 1991; D. Kimbrough, unpublished data). TiO_2, Al_2O_3, (FeO* + MgO), CaO, K_2O, and Sr decrease, whereas Na_2O and Rb increase with increasing SiO_2 and Ba shows no correlation with SiO_2 content (Figs 6 and 7).

There is variability in the absolute REE concentrations, although the chondrite-normalized REE patterns are consistently flat with La_N/Lu_N ranging between 1·40 and 2·08 (Fig. 8). All patterns have a prominent negative Eu anomaly (Eu/Eu* = 0·10–0·47). These REE patterns are similar

to those of Cretaceous granites from the Edward VII Peninsula reported by Weaver *et al.* (1992).

Other rocks and migmatite components

The compositional range of the migmatitic paragneiss typically overlaps with the Swanson Formation metasedimentary rocks. With increasing SiO_2 in the paragneiss, TiO_2, Al_2O_3, ($FeO^* + MgO$), and K_2O decrease, and CaO and Na_2O increase (Fig. 6). Rb/Sr ratios generally decrease with increasing SiO_2, which is controlled primarily by variations in Rb content. The chondrite-normalized REE patterns for the paragneiss are very similar to the REE patterns from the Swanson Formation (Fig. 8).

Five leucosome–melanosome pairs were separated from migmatitic paragneiss. Two localities are from Mt. Avers in the central Fosdick Mountains, and three localities are from paragneiss layers in the sheeted leucogranite complex to the east (Fig. 1d).

Leucosome compositions from the paragneiss have normalized SiO_2 contents ranging between 71 and 77·5 wt %, and are peraluminous with ASI values between 1·07 and 1·25. TiO_2 and Al_2O_3 generally decrease with increasing SiO_2, whereas ($FeO^* + MgO$), CaO, K_2O, Na_2O, Sr, Rb, and Ba show no correlation with SiO_2 (Figs 6 and 7). The Rb/Sr ratios are typically between 0·4 and 0·55, although one sample within the sheeted leucogranite complex (sample K6-B48) has a slightly higher Rb/Sr ratio of 1·19. Zr contents are lower than in granites with Type I zircon, and are similar to or slightly elevated with respect to granites with Type II zircon (Fig. 7). The two leucosome samples from Mt. Avers have a large difference in SiO_2 and Al_2O_3, and elevated K_2O and Ba contents and lower Na_2O compared with the leucosomes from paragneiss layers within the leucogranite sheeted complex (Fig. 6). The LREE patterns define smooth to slightly concave-downward trends and the HREE patterns have smooth to slightly concave-upward trends (Fig. 8). Four of the leucosomes have prominent negative Eu anomalies ($Eu/Eu^* = 1·46–2·47$), but one leucosome from the sheeted leucogranite complex (sample K6-B48) has a positive Eu anomaly ($Eu/Eu^* = 0·45$).

The melanosome compositions have normalized SiO_2 contents ranging between 59 and 71·5 wt %. TiO_2, Al_2O_3, CaO, K_2O, and Na_2O generally decrease with increasing SiO_2. However, a sample from Mt. Avers (K6-A22) with the lowest SiO_2 content also corresponds to the lowest CaO and Na_2O contents (Tables 2 and 3; data not shown in Figs 6 and 7). Melanosome samples show no correlation between ($FeO^* + MgO$), Sr, Rb, and Ba contents and SiO_2 (Figs 6 and 7). The chondrite-normalized REE patterns for the melanosomes are similar to the REE patterns from the paragneiss (Fig. 8). There is typically less variability in the LREE contents in the melanosomes as compared with the bulk migmatitic paragneiss, whereas the HREE contents are more variable. The melanosomes also have more negative Eu anomalies ($Eu/Eu^* = 0·16–0·33$) compared with the paragneiss ($Eu/Eu^* = 0·42–0·66$).

The whole-rock compositions of the orthogneiss are broadly comparable with those of the Ford Granodiorite suite. TiO_2, Al_2O_3, ($FeO^* + MgO$), CaO, Na_2O and Sr contents decrease, and K_2O increases with increasing SiO_2 (Figs 6 and 7). Ba shows no correlation with SiO_2 content. The REE patterns are generally smooth with some variability in the HREE (Fig. 8). One sample (K6-Bb45) has a prominent negative Eu anomaly ($Eu/Eu^* = 0·34$), whereas the other two samples have a slightly negative or no Eu anomaly ($Eu/Eu^* = 0·82–0·96$).

One leucosome separate was analyzed from orthogneiss K6-B26 from Mt. Bitgood, which has lower SiO_2, Na_2O, Th, and Zr compared with the other leucosomes and granites, but elevated K_2O, CaO, Al_2O_3, P_2O_5, Ba, Sr, and Rb (Figs 6 and 7). The chondrite-normalized REE pattern is flat ($La_N/Lu_N = 3·99$; Fig. 8) with a negative Eu anomaly ($Eu/Eu^* = 0·53$) and minor depletion in the HREE. The HREE depletion in the leucosome probably reflects the partitioning of HREE into garnet that is mainly present along the selvedge between the melanosome and leucosome.

Zircon saturation thermometry for granites

In a cooling magma undersaturated with respect to Zr, the temperature at which zircon saturates in a melt (T_{Zr}) can be estimated from the granite rock composition using the zircon saturation thermometer of Watson & Harrison (1983). Table 2 shows the range of calculated temperatures using the compositional parameters M (= [(Na + K + 2Ca)/(Al × Si)]; Watson & Harrison, 1983) and FM (= [(Na + K + 2(Ca + Fe + Mg))/(Al × Si)]; Ryerson & Watson, 1987; Baker *et al.*, 2002). The calculated temperatures using the empirical Zr saturation equation defined by Kelsey *et al.* (2008) are also listed in Table 2.

Using the M parameter and the thermometer of Watson & Harrison (1983), the Carboniferous granites have saturation temperatures of 815–785°C, whereas the Cretaceous granites have saturation temperatures of 810–665°C (Table 2). The Cretaceous granites in the sheeted leucogranite complex with Type II ('inherited') zircon have systematically lower temperatures (735–665°C) than the two Cretaceous granites with Type I ('magmatic') zircon within the deeper structural level of the complex (810 and 775°C). Sample C5-R23 groups with the Cretaceous granites with magmatic zircon (Type I) but represents a higher structural level above the detachment. The zircon saturation temperature from this sample is 760°C.

Sr and Nd isotopic compositions

Sr and Nd isotopic compositions and Nd and Sm concentrations for representative samples of various rock types were acquired at the Department of Geology, University of Maryland (Table 4). Methods and analytical

Table 4: Sr–Nd isotopic compositions for whole-rock and components

Rock type:	Carboniferous low Rb/Sr granite			High Rb/Sr	Cretaceous granite, Type I zircon		
Sample no.:	K6-A21b	K6-I60	K6-T35b	C5-Is51A	C5-Is54	C5-R23	K6-Mt38
Sm	6·78	5·56	4·29	7·89	4·90	4·25	5·94
Nd	38·88	29·71	24·28	38·84	23·81	22·90	29·45
Sm/Nd	0·174	0·187	0·177	0·203	0·206	0·186	0·202
$^{87}Rb/^{86}Sr$	1·36	1·37	1·78	7·60	2·28	2·00	1·66
$^{87}Sr/^{86}Sr$	0·7151	0·7127	0·7151	0·7530	0·7135	0·7183	0·7190
$^{87}Sr/^{86}Sr_{(100Ma)}$	0·7132	0·7108	0·7126	0·7422	0·7102	0·7154	0·7167
$^{87}Sr/^{86}Sr_{(350Ma)}$	0·7084	0·7059	0·7063	0·7152	0·7021	0·7083	0·7108
$^{147}Sm/^{144}Nd$	0·1053	0·1130	0·1067	0·1228	0·1244	0·1122	0·1219
$^{143}Nd/^{144}Nd$	0·5122	0·5123	0·5123	0·5121	0·5124	0·5123	0·5122
$\varepsilon Nd_{(100Ma)}$	−6·9	−6·0	−6·0	−9·1	−3·9	−4·8	−7·5
$\varepsilon Nd_{(350Ma)}$	−3·9	−3·4	−3·2	−6·8	−1·6	−2·1	−5·1

Rock type:	Cretaceous LREE-depleted granite				Ford Granodiorite suite		Byrd Coast Granite suite	
Sample no.:	K6-B27	K6-Bb47	K6-L10	K6-Mj01	912-2A	9N27-4	9D12-2	K6-NU01
Sm	0·70	0·20	3·64	1·16	9·43	4·00	9·81	2·82
Nd	3·00	0·87	17·25	5·30	50·13	20·17	34·64	7·32
Sm/Nd	0·234	0·227	0·211	0·218	0·188	0·198	0·283	0·385
$^{87}Rb/^{86}Sr$	4·48	2·54	3·47	1·22	7·10	0·88	21·53	23·30
$^{87}Sr/^{86}Sr$	0·7454	0·7269	0·7314	0·7172	0·7411	0·7106	0·7413	0·7411
$^{87}Sr/^{86}Sr_{(100Ma)}$	0·7390	0·7233	0·7265	0·7155	0·7311	0·7094	0·7107	0·7080
$^{87}Sr/^{86}Sr_{(350Ma)}$	0·7231	0·7142	0·7141	0·7111	0·7059	0·7063	0·6343	0·6253
$^{147}Sm/^{144}Nd$	0·1412	0·1373	0·1275	0·1317	0·1137	0·1198	0·1713	0·2329
$^{143}Nd/^{144}Nd$	0·5123	0·5122	0·5122	0·5122	0·5123	0·5123	0·5124	0·5124
$\varepsilon Nd_{(100Ma)}$	−6·6	−7·4	−6·9	−7·4	−4·9	−4·7	−3·6	−5·0
$\varepsilon Nd_{(350Ma)}$	−4·9	−5·5	−4·7	−5·3	−2·3	−2·2	−2·8	−6·2

Rock type:	Swanson Formation				Paragneiss			Leucosome
Sample no.:	K6-SR29	K6-SR30	K6-SR31	K6-SR32	K6-A22	K6-A24	K6-B51	K6-B26
Sm	7·57	7·88	7·24	6·02	19·91	15·69	9·03	10·08
Nd	42·78	38·24	37·86	27·91	100·59	82·82	47·99	32·12
Sm/Nd	0·177	0·206	0·191	0·216	0·198	0·189	0·188	0·314
$^{87}Rb/^{86}Sr$	6·56	4·41	2·50	1·96	4·42	3·63	6·32	1·86
$^{87}Sr/^{86}Sr$	0·7585	0·7449	0·7320	0·7264	0·7355	0·7373	0·7364	0·7162
$^{87}Sr/^{86}Sr_{(100Ma)}$	0·7474	0·7386	0·7284	0·7236	0·7293	0·7321	0·7274	0·7136
$^{87}Sr/^{86}Sr_{(350Ma)}$	0·7241	0·7229	0·7195	0·7166	0·7136	0·7192	0·7049	0·7070
$^{147}Sm/^{144}Nd$	0·1070	0·1246	0·1156	0·1304	0·1196	0·1145	0·1138	0·1898
$^{143}Nd/^{144}Nd$	0·5120	0·5120	0·5120	0·5121	0·5121	0·5121	0·5121	0·5123
$\varepsilon Nd_{(100Ma)}$	−12·0	−11·2	−11·2	−9·6	−10·2	−9·9	−9·4	−6·5
$\varepsilon Nd_{(350Ma)}$	−9·2	−8·9	−8·7	−7·5	−7·7	−7·2	−6·8	−6·3

(continued)

Table 4: Continued

Rock type:	Leucosome in paragneiss			Melanosome in paragneiss			Orthogneiss	
Sample no.:	K6-A22	K6-A24	K6-B51	K6-A22	K6-A24	K6-B51	K6-B26	K6-L12
Sm	3·11	1·74	3·52	26·32	17·22	10·15	5·66	2·84
Nd	13·88	6·43	17·10	142·89	102·00	52·52	32·35	13·21
Sm/Nd	0·224	0·270	0·206	0·184	0·169	0·193	0·175	0·215
$^{87}Rb/^{86}Sr$	1·45	1·51	1·28	16·78	9·75	46·99	1·36	1·86
$^{87}Sr/^{86}Sr$	0·7306	0·7361	0·7297	0·7455	0·7452	0·7951	0·7145	0·7162
$^{87}Sr/^{86}Sr_{(100Ma)}$	0·7285	0·7340	0·7279	0·7216	0·7313	0·7284	0·7125	0·7136
$^{87}Sr/^{86}Sr_{(350Ma)}$	0·7234	0·7286	0·7233	0·6621	0·6967	0·5616	0·7077	0·7070
$^{147}Sm/^{144}Nd$	0·1357	0·1633	0·1244	0·1113	0·1020	0·1168	0·1059	0·1300
$^{143}Nd/^{144}Nd$	0·5121	0·5121	0·5122	0·5121	0·5121	0·5121	0·5122	0·5123
$\varepsilon Nd_{(100Ma)}$	−9·5	−9·2	−8·3	−10·2	−9·8	−9·0	−6·6	−5·5
$\varepsilon Nd_{(350Ma)}$	−7·5	−8·1	−6·0	−7·4	−6·8	−6·4	−3·7	−3·4

Sm, Nd concentrations measured by isotope dilution with the ICP-MS.

uncertainties are given in the Appendix. Whole-rock Sr and Nd isotope ratios for rocks from the Ford Ranges, age corrected to 350 Ma and 100 Ma, are presented in Fig. 9.

Potential source rocks

Isotopic compositions of potential source rocks have been age corrected to 350 Ma and 100 Ma. The dataset presented here also includes data from Weaver *et al.* (1992), Pankhurst *et al.* (1998), and Adams *et al.* (2005). Analyzed Swanson Formation samples have relatively high $^{87}Sr/^{86}Sr$ and negative εNd, similar to the isotopic characteristics of the various sedimentary formations along the convergent margin of East Gondwana, including the Lachlan Fold Belt in Australia (Turner *et al.*, 1993), the Greenland Belt in New Zealand (Waight *et al.*, 1998), and the Wilson Terrane of Northern Victoria Land (Turner *et al.*, 1993). At 350 Ma, the Swanson Formation has $^{87}Sr/^{86}Sr_{(350Ma)}$ values between 0·7166 and 0·7350 with εNd$_{(350Ma)}$ ranging from −11·5 to −7·5 (Fig. 9). The Ford Granodiorite suite has $^{87}Sr/^{86}Sr_{(350Ma)}$ ranging from 0·7051 to 0·7078, and εNd$_{(350Ma)}$ from −3·5 to −0·7 (Fig. 9). At 100 Ma, the Swanson Formation has $^{87}Sr/^{86}Sr_{(100Ma)}$ = 0·7236−0·7707 and εNd$_{(100Ma)}$ = −14 to −9·6, and the Ford Granodiorite suite has $^{87}Sr/^{86}Sr_{(100Ma)}$ = 0·7078−0·7311 and εNd$_{(100Ma)}$ = −6·2 to −3·1 (Fig. 9).

Carboniferous granites

The Carboniferous granites with low Rb/Sr ratios (<1·0) have $^{87}Sr/^{86}Sr_{(350Ma)}$ and εNd$_{(350Ma)}$ values ranging from 0·7059 to 0·7084 and from −3·9 to −3·2, respectively. The isotope compositions are comparable with those of samples from the Ford Granodiorite suite (Fig. 9). In contrast, sample C5-Is51A (Rb/Sr > 2·5) has a higher

$^{87}Sr/^{86}Sr_{(350Ma)}$ (0·7152) and more negative εNd$_{(350Ma)}$ (−6·8) than those of the other Carboniferous granites, and is comparable with the range of the Swanson Formation (Fig. 9). The significant difference in the isotope compositions between the two granite types strongly suggests derivation from different sources.

Cretaceous granites

The three Cretaceous granites with magmatic zircon (Type I) have a range of εNd$_{(100Ma)}$ values (−7·5 to −3·9) but similar $^{87}Sr/^{86}Sr_{(100Ma)}$ values (0·7167−0·7102; Fig. 9). These results are broadly comparable with those for samples from the Byrd Coast Granite suite ($^{87}Sr/^{86}Sr_{(100Ma)}$ = 0·7080−0·7212; εNd$_{(100Ma)}$ = −7·7 to −3·6, this study; Weaver *et al.*, 1992) and samples from the Ford Granodiorite suite (Fig. 9). The Cretaceous granites with inherited zircon (Type II) have similar εNd$_{(100Ma)}$ values ranging from −7·4 to −6·6, and $^{87}Sr/^{86}Sr_{(100Ma)}$ values ranging from 0·7155 to 0·7390.

Other rocks and migmatite components

The migmatites in the deepest structural level of the Fosdick migmatite–granite complex underwent melting and melt loss during a Carboniferous high-temperature metamorphic event although additional low-volume melt may have been generated from residual compositions during the Cretaceous event (Korhonen *et al.*, 2009). To evaluate which partial melting event the leucosome network and host gneisses actually record, the isotopic data have been age-corrected to 350 Ma and 100 Ma (Fig. 9).
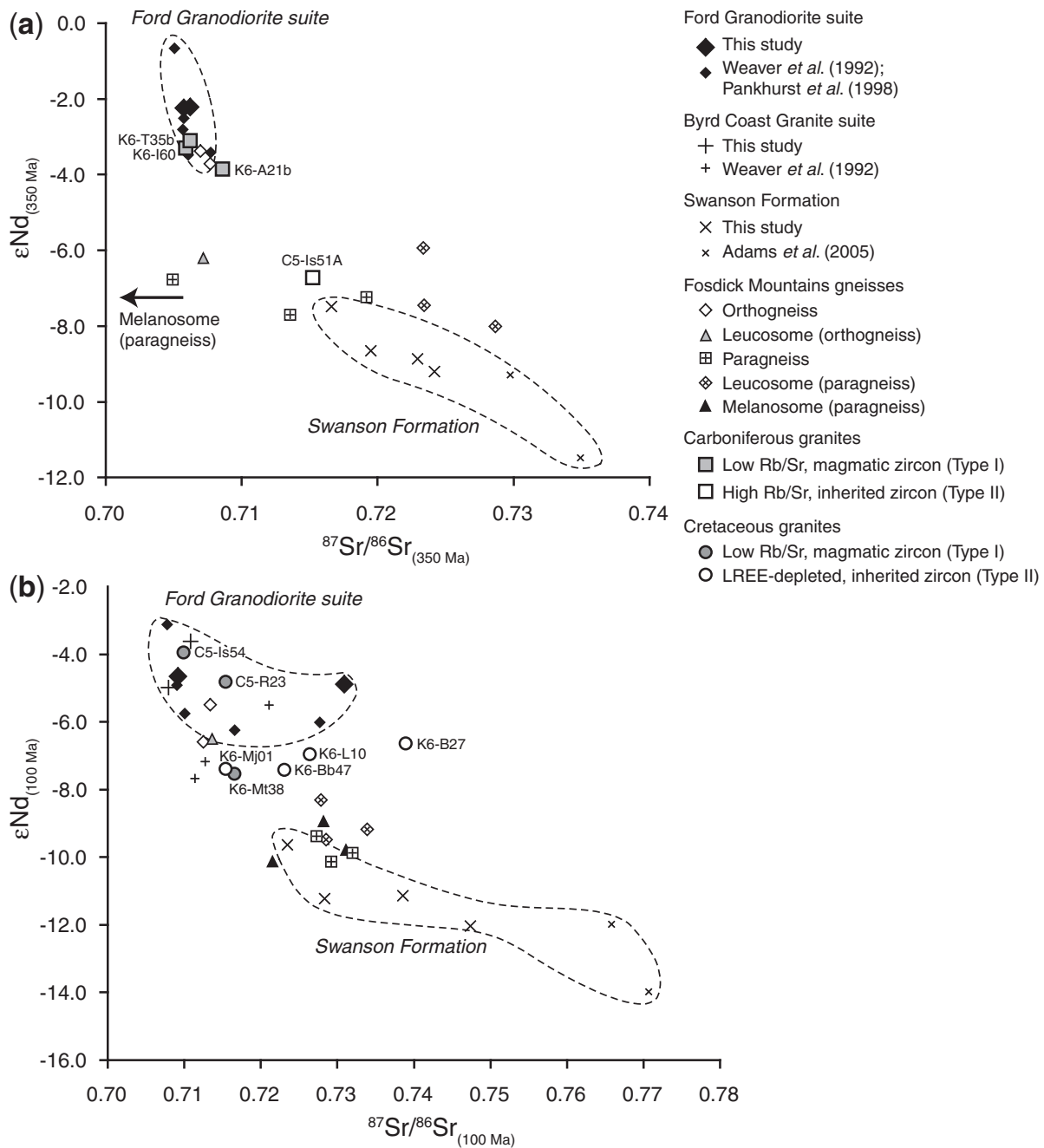
Fig. 9. εNd–$^{87}Sr/^{86}Sr$ isotopic compositions at (a) 350 Ma and (b) 100 Ma for rocks from the Ford Ranges. Dashed fields indicate the range of Ford Granodiorite suite and Swanson Formation sources.

At 100 Ma, three paragneiss samples have $^{87}Sr/^{86}Sr_{(100Ma)}$ ranging from 0·7274 to 0·7321, and $\varepsilon Nd_{(100Ma)}$ between −10·2 and −9·4, comparable with those of the Swanson Formation age corrected to 100 Ma (Fig. 9). At 350 Ma, the paragneiss has lower $^{87}Sr/^{86}Sr_{(350Ma)}$ values (0·7049–0·7192) than the Swanson Formation age corrected to 350 Ma, but slightly higher $\varepsilon Nd_{(350Ma)}$ values (−7·7 to −6·8; Fig. 9). The leucosome

and melanosome components have broadly similar isotopic compositions to the paragneiss at 100 Ma. The melanosomes typically have similar $\varepsilon Nd_{(100Ma)}$ values (−10·2 to −9·0) to the whole-rock, although a sample from the sheeted leucogranite complex (sample K6-B5l; Fig. 1d) has a slightly higher $\varepsilon Nd_{(100Ma)}$ value. A melanosome from Mt. Avers (sample K6-A22; Fig. 1d) has a lower $^{87}Sr/^{86}Sr_{(100Ma)}$ value (0·7216) than the whole-rock.

The leucosomes have systematically higher $\varepsilon Nd_{(100Ma)}$ values ($-9\cdot5$ to $-8\cdot3$) compared with the melanosomes and whole-rock, and similar $^{87}Sr/^{86}Sr_{(100Ma)}$ values ($0\cdot7279-0\cdot7340$) to the whole-rock. At 350 Ma, the isotopic compositions of the migmatite components are significantly different from those of the paragneiss host. These data support an anatectic event at *c.* 100 Ma (e.g. Korhonen *et al.*, 2009).

The two orthogneiss samples analyzed have similar isotopic compositions. At 350 Ma, the $^{87}Sr/^{86}Sr_{(350Ma)}$ and $\varepsilon Nd_{(350Ma)}$ values range from $0\cdot7070$ to $0\cdot7077$ and from $-3\cdot7$ to $-3\cdot4$, respectively. Age correction to 100 Ma results in $^{87}Sr/^{86}Sr_{(100Ma)}$ values of $0\cdot7125-0\cdot7136$ and $\varepsilon Nd_{(100Ma)}$ from $-6\cdot6$ to $-5\cdot5$. Both sets of age-corrected data are comparable with the isotopic compositions of the Ford Granodiorite suite (Fig. 9). The similarity in the major and trace element compositions of the orthogneiss and the Ford Granodiorite suite (Figs 6 and 7) supports previous interpretations that the protolith of the orthogneiss is Ford Granodiorite suite rocks (e.g. Siddoway *et al.*, 2004).

An in-source leucosome component separated from one of the orthogneiss samples in the sheeted leucogranite complex has an isotopic composition of $^{87}Sr/^{86}Sr_{(100Ma)}$ $= 0\cdot7136$ and $\varepsilon Nd_{(100Ma)} = -6\cdot5$. These values are very similar to the isotopic composition of the host orthogneiss at 100 Ma (Fig. 9). Age correction to 350 Ma results in a more negative $\varepsilon Nd_{(350Ma)}$ value for the leucosome ($-6\cdot3$) compared with the host orthogneiss ($-3\cdot7$). These data support a low-volume anatectic event at *c.* 100 Ma (e.g. Korhonen *et al.*, 2009).

DISCUSSION
Carboniferous granites in the Fosdick migmatite–granite complex
Relationship between Ford Granodiorite suite and Carboniferous granites

Compositional variability within the Ford Granodiorite suite can be investigated using the ternary system (Na + Ca)−(Fe* + Mg + Ti)−K (Fig. 10a; after Solar & Brown, 2001). The most primitive Ford Granodiorite suite compositions analyzed plot near the biotite–plagioclase tieline in Fig. 10a. Plagioclase, hornblende and biotite are the primary phases that would fractionate from Ford Granodiorite suite magmas, resulting in the displacement of evolved compositions from these phases (Fig. 10a) provided that mass balance is preserved during crystallization.

The similarity between the Sr–Nd isotopic compositions of the Carboniferous low Rb/Sr granites and the Ford Granodiorite suite suggests that the granites are genetically related to the Ford Granodiorite suite (Fig. 9). The compositions of the Carboniferous granites generally fall within the range of fractionated Ford Granodiorite suite compositions (Fig. 10a). However, the Zr/Y ratios of the Carboniferous granites are higher than those of the Ford Granodiorite suite rocks (Fig. 11), which is inconsistent with the granites representing fractionated Ford Granodiorite suite magmas. In addition, the Carboniferous granites yield zircon crystallization ages of *c.* 358–336 Ma, which post-date the short-lived pulse of Devonian–Carboniferous calc-alkaline magmatism in the Ford Ranges and emplacement of the Ford Granodiorite suite at *c.* 375 Ma (Pankhurst *et al.*, 1998).

Field relationships between the Carboniferous granites and inferred Ford Granodiorite suite also demonstrate that the granite crystallization post-dates emplacement of the Ford Granodiorite suite. The granodiorite enclaves in the Carboniferous granite body at Mt. Iphigene contain a weak foliation that is rotated with respect to the magmatic foliation of the host granite (Fig. 3e). Except for a thin reaction selvedge on the margins, the enclaves appear to be relatively unaffected by the host granite. These results suggest that the Carboniferous low Rb/Sr granites are anatectic products of Ford Granodiorite suite plutons, and not fractionated Ford Granodiorite suite magmas.

Petrogenesis of Carboniferous granites
Ford Granodiorite source. The low Rb contents in the granites derived from the Ford Granodiorite suite are consistent with melting reactions that do not involve biotite, whereas the elevated Sr contents probably reflect the involvement of plagioclase. Previous mineral equilibria modeling of Ford Granodiorite suite compositions has shown that the major melt-producing reactions (>10 vol. % melt) occur at temperatures above biotite stability, probably involving hornblende (+ plagioclase) breakdown (Korhonen *et al.*, 2009); results consistent with the granite chemistry. The modeling also suggests that less evolved Ford Granodiorite suite compositions (e.g. sample 9N27-4; Fig. 10a) are significantly more fertile than the evolved compositions (e.g. sample 912-2A; Fig. 10a) at the same *P–T* conditions.

The partial melting experiments of Skjerlie & Johnston (1993) used a composition similar to the less evolved, more fertile Ford Granodiorite suite compositions (Fig. 10a), and may provide an appropriate comparison for melt compositions derived from the Ford Granodiorite suite. In-source leucosome in orthogneiss (sample K6-B26) and granite sample K6-A21b have similar compositions to the experimental glasses of Skjerlie & Johnston (1993), suggesting that they may represent near-melt compositions. The compositions of the other Carboniferous low Rb/Sr granites can be modeled by either the entrainment of residual biotite and plagioclase or the accumulation of early crystallized phases (Fig. 10a). However, there is no textural evidence for residual phases, suggesting that the cumulate is composed of early crystallized phases. Projecting from the inferred melt composition represented by the leucosome in orthogneiss through the granite composition onto the biotite–plagioclase tieline
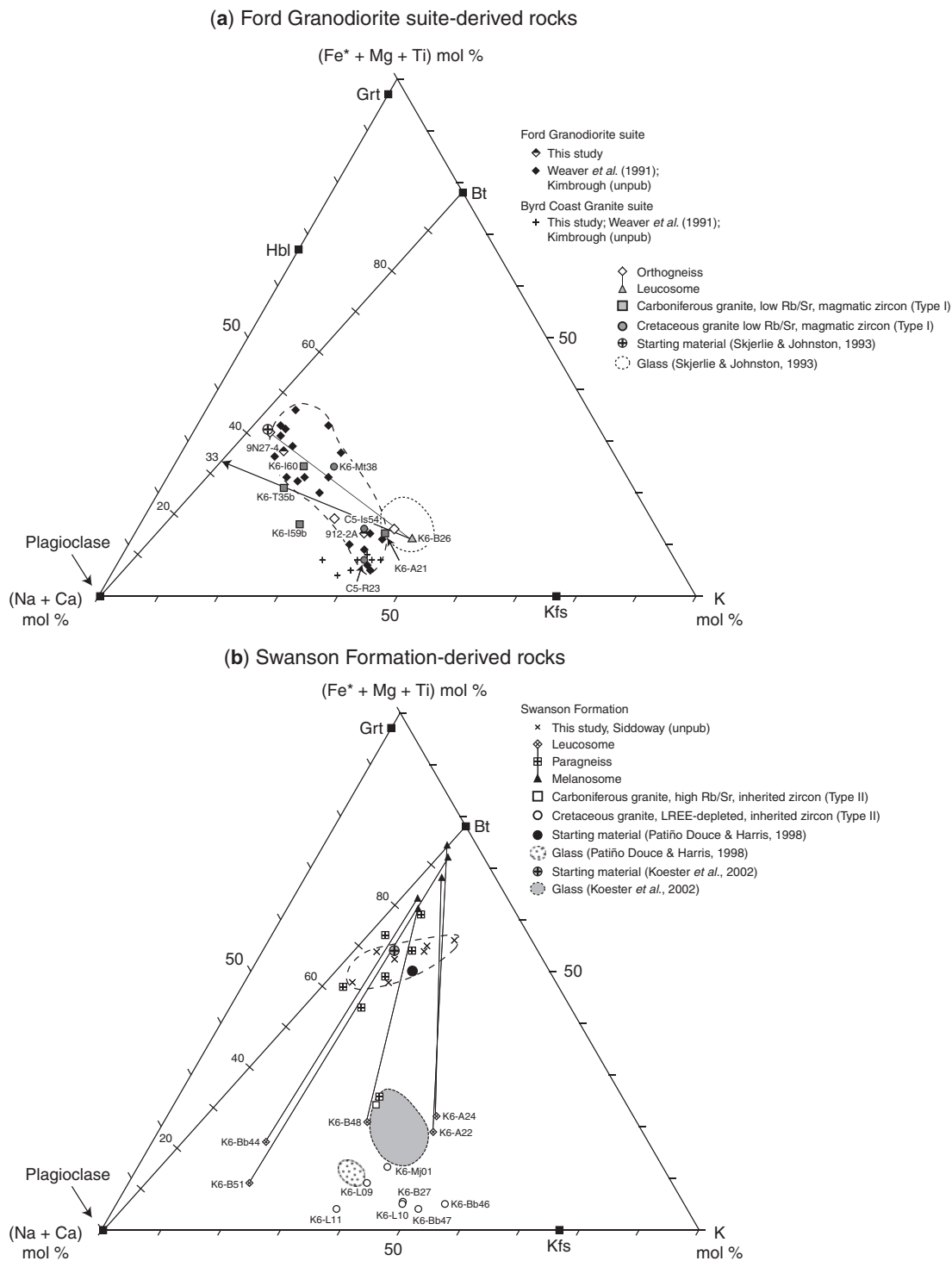
Fig. 10. $(Fe^* + Mg + Ti)–K–(Na + Ca)$ ternary diagram (after Solar & Brown, 2001) for (a) Ford Granodiorite suite-derived rocks and (b) Swanson Formation-derived rocks. Experimental studies for starting materials with compositions similar to the Ford Granodiorite suite and Swanson Formation and corresponding glass compositions are also shown. Tick marks on the line connecting biotite and plagioclase are 20% increments of biotite content, and represent the amount of cumulate and the proportion of these phases in the cumulate. The arrow through sample K6-T35b from the inferred melt composition represented by the leucosome in orthogneiss tracks the model cumulate and fractionated melt trend. The granite composition would require the addition of ∼65% cumulate comprising ∼33% biotite and 67% plagioclase. Petrogenenic models for other granites are described in the text.
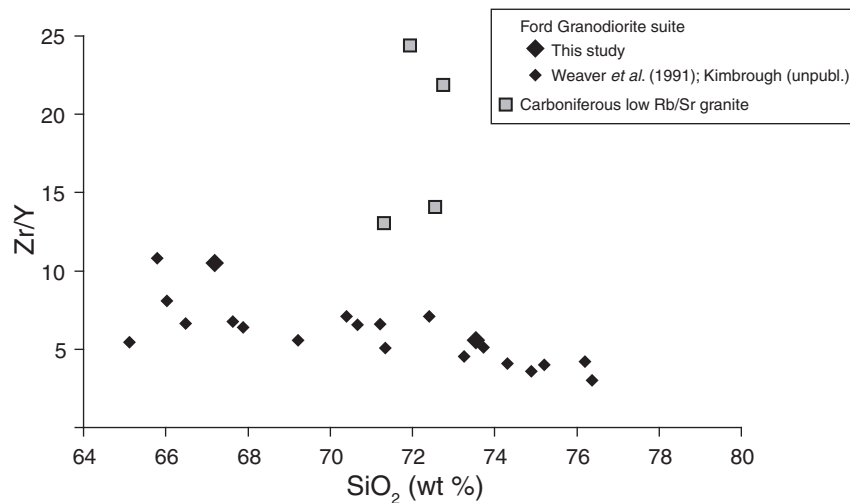
Fig. 11. Zr/Y vs SiO$_2$ for Ford Granodiorite suite and Carboniferous granites. The decrease in Zr/Y ratios with increasing SiO$_2$ within the Ford Granodiorite suite shows the range of fractionated compositions, and suggests that the Carboniferous granites are not fractionated Ford Granodiorite suite magmas. Data for Ford Granodiorite suite include data from Weaver *et al.* (1991) and Kimbrough (unpublished data).

indicates the amount of cumulate and the proportion of these phases that would need to be incorporated into the granite (Fig. 10a). Sample K6-T35b would require the addition of ∼65% cumulate comprising ∼33% biotite and 67% plagioclase, whereas sample K6-I60 is consistent with ∼33% cumulate with ∼40% biotite and 60% plagioclase. Sample K6-I59b represents the same granite body as K6-I60, and can be modeled by the fractionation of ∼60% biotite and ∼40% plagioclase from K6-I60. Alternatively, it can be modeled as a 50% cumulate with ∼20% biotite and 80% plagioclase. Uncertainties in the melt composition would only slightly modify the relative proportions of cumulate phases. The accumulation of plagioclase and biotite would increase the Rb and Sr contents of the granites relative to the initial melt compositions, although these granites have similar Rb/Sr ratios (∼0·5), suggesting that the proportion of cumulate biotite and plagioclase had a similar effect on the Rb/Sr ratios.

Swanson Formation source. The Sr–Nd isotope composition of sample C5-Is51A is similar to the isotopic composition of the Swanson Formation (Fig. 9). This granite also has much higher Rb contents and lower Sr contents compared with the granites derived from the Ford Granodiorite suite, suggestive of melting reactions involving biotite. The experimental melting studies of Himalayan metapelites by Patiño Douce & Harris (1998) used starting materials with similar compositions to the Swanson Formation (Fig. 10b). The composition of C5-Is51A is displaced from the experimental glass compositions towards biotite, possibly reflecting the entrainment of residual or accumulation of early crystallized biotite (Fig. 10b). This process may also account for the elevated Rb contents in this granite.

Cretaceous granites in the Fosdick migmatite–granite complex

Petrogenesis of Cretaceous granites

Ford Granodiorite source. The Sr–Nd isotope compositions of samples C5-Is54 and C5-R23 are within the isotopic range of the Ford Granodiorite suite source (Fig. 9). In addition, the trace element compositions and REE patterns of these samples are similar to the Carboniferous low Rb/Sr granites, also derived from the Ford Granodiorite suite (Fig. 8), and sample C5-R23 contains inherited Devonian–Carboniferous zircon cores (Fig. 4j). The major element composition of C5-Is54 can be explained as a melt composition with the accumulation of minor amounts of biotite and plagioclase, similar to Carboniferous granite K6-A2lb (Fig. 10a). The composition of sample C5-R23 reflects a melt composition with the addition of an ∼35% cumulate comprising ∼40% K-feldspar and 60% plagioclase (Fig. 10a). The accumulation of early crystallized K-feldspar from an evolved liquid is consistent with the emplacement of this granite at structural levels above the detachment and lower zircon saturation temperatures compared with the granites at deeper structural levels.

The role of accessory phases related to these petrogenetic processes can be assessed through Sr–Nd isotope and trace element chemistry. Differences in the involvement of accessory phases that sequester the Sm and Nd budget may result in Sm/Nd fractionation, and higher Sm/Nd ratios may indicate increasing apatite dissolution in the source (Zeng *et al.*, 2005). The Sm/Nd ratio of C5-R23 is within the range of the Ford Granodiorite suite source, whereas the Sm/Nd ratio of C5-Is54 is greater
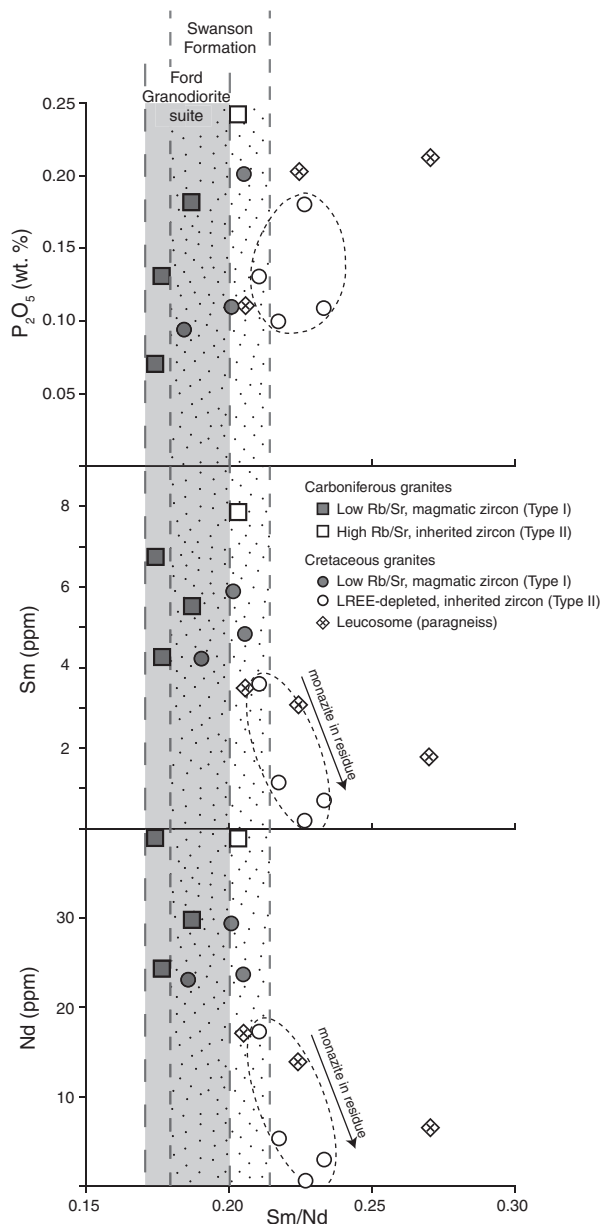
Fig. 12. Sm/Nd vs P_2O_5, Sm, and Nd for Carboniferous and Cretaceous granites and leucosome in paragneiss compared with the range of Sm/Nd for the Ford Granodiorite suite (this study; Weaver *et al.*, 1992; Pankhurst *et al.*, 1998) and Swanson Formation (this study; Adams *et al.*, 2005) sources. Plotted Sm and Nd contents were measured by isotope dilution with ICP-MS (Table 4). The Cretaceous granites derived from the Swanson Formation (Fig. 7) with distinct LREE depletion and inherited zircon (Type II) and the leucosomes in the paragneiss have systematically higher Sm/Nd than the source, consistent with inhibited monazite dissolution.

than that of the source (Fig. 12), consistent with increased apatite dissolution. The relatively high P_2O_5 content in sample C5-Is54 is also consistent with apatite dissolution. This process will increase the $\varepsilon Nd_{(100Ma)}$ values relative to the source (Zeng *et al.*, 2005), and may account for

$\varepsilon Nd_{(100Ma)}$ near the upper values for the range of Ford Granodiorite suite samples.

Sample K6-Mt38 has chemical similarities to the Carboniferous and Cretaceous granites derived from the Ford Granodiorite suite, although the $\varepsilon Nd_{(100Ma)}$ value is lower (Fig. 9). An $\varepsilon Nd_{(100Ma)}$ value more negative than the inferred Ford Granodiorite suite source suggests either monazite or apatite in the residue or a contribution from a source with lower $\varepsilon Nd_{(100Ma)}$, such as the Swanson Formation. The presence of monazite or apatite in the residue would also lower Sm/Nd ratios relative to the source (Zeng *et al.*, 2005), whereas the Sm/Nd ratio of K6-Mt38 is slightly higher than the Ford Granodiorite suite, but within the range defined by the Swanson Formation (Fig. 12). Therefore, the isotopic composition of K6-Mt38 probably reflects either a mixture of melts derived from Swanson Formation and Ford Granodiorite suite or a hybrid source. The biotite in this sample is distinctive from the other granites, and closely resembles biotite from the paragneiss, which is equated to the Swanson Formation. The entrainment of residual biotite with inclusions of accessory phases during emplacement of granite sourced from the Ford Granodiorite suite could account for an $\varepsilon Nd_{(100Ma)}$ composition between the two sources. The major element composition of K6-Mt38 is displaced towards the biotite–plagioclase join in Fig. 10a, consistent with the accumulation of residual and/or early crystallized biotite and plagioclase.

Fertile Swanson Formation source. The Cretaceous granites with inherited zircon (Type II) have isotopic compositions that lie between the Ford Granodiorite suite and the Swanson Formation, similar to sample K6-Mt38 described above. The granites have a narrow range in $\varepsilon Nd_{(100Ma)}$ values, but a wide range in $^{87}Sr/^{86}Sr_{(100Ma)}$ values (Fig. 9). Although a possible hybrid source composed of Ford Granodiorite suite and the Swanson Formation is consistent with the isotope compositions, the granites typically have Sm/Nd ratios greater than both potential sources (Fig. 12). Dissolution of apatite into the melt can strongly influence the Sm–Nd isotopic system, increasing Sm/Nd ratios and εNd values relative to the source. The LREE-depleted signature of these granites also implicates monazite as a fractionating phase (e.g. Wark & Miller, 1993; Watt & Harley, 1993; Nabelek & Glascock, 1995; Fig. 8), which has been used to explain Nd isotopic differences within granites from other studies (e.g. Harrison *et al.*, 1987; Ayres & Harris, 1997; Zeng *et al.*, 2005).

Under high-temperature and low water content conditions, apatite dissolution can suppress monazite dissolution and/or favor monazite crystallization, and a combination of these processes will enhance the apatite signature (Zeng *et al.*, 2005). The Cretaceous granites do not show a correlation between Sm/Nd and P_2O_5 (Fig. 12) as would be expected if apatite was the major phase controlling

Sm–Nd fractionation. However, LREE contents decrease systematically with increasing Sm/Nd ratios (Fig. 12), consistent with modal differences in monazite. These results imply that monazite sequestered in the residue during melting and/or melt extraction may have elevated the $\varepsilon Nd_{(100Ma)}$ values and Sm/Nd ratios of the granites with respect to the source. The Ford Granodiorite suite has higher $\varepsilon Nd_{(100Ma)}$ values than the granites, therefore it cannot be the primary source.

To evaluate the effects of selective dissolution of apatite with inhibited monazite dissolution on the Nd isotopic composition of granites sourced from the Swanson Formation, the $\varepsilon Nd_{(100Ma)}$ values of apatite and monazite in the Swanson Formation were estimated. The Swanson Formation represents accumulation of voluminous sediments derived from the Ross–Delamerian Orogen along the convergent margin of Gondwana (e.g. Squire *et al.*, 2006; Fig. 13a). Therefore, Nd isotopic compositions of monazite and apatite from average I-type and S-type granite in the Delamerian Orogen (*c.* 500 Ma, Foden *et al.*, 2002) may provide suitable compositions for isotopic modeling.

The calculated $\varepsilon Nd_{(100Ma)}$ values for apatite sourced from average sediments in the Delamerian Orogen range from −9·6 to −2·3 (Table 5). These values are more positive than the $\varepsilon Nd_{(100Ma)}$ of the average Swanson Formation composition (−11·7; Table 4) but within the range of the granites (−7·4 to −6·6; Fig. 9). These results support the proposal that the selective dissolution of apatite into the melt during anatexis of the Swanson Formation could produce granites with the observed Nd isotopic composition. However, limitations of the modeling, including uncertainty in the actual $\varepsilon Nd_{(100Ma)}$ values of apatite and monazite in the Swanson Formation, allow the possibility of a minor Ford Granodiorite component.

The compositions of these Cretaceous granites are displaced towards the K-feldspar–plagioclase join relative to experimental glass compositions derived from the Himalayan metapelites (Fig. 10b; Patiño Douce & Harris, 1998), suggesting the accumulation of early crystallized K-feldspar and plagioclase from an evolved liquid. This process would result in elevated Sr contents and consequently a lower Rb/Sr ratio than the initial melt composition. However, the elevated Rb contents probably approximate the initial melt contents and suggest melting reactions involving biotite, consistent with the inferred melting reactions constrained by mineral equilibria modeling of fertile Swanson Formation (Korhonen *et al.*, 2009).

Mica breakdown melting would result in accumulation of residual plagioclase in the source, leading to a relatively Eu-depleted liquid. Plagioclase crystallized from such a liquid would have low Eu contents, and accumulation of these feldspars would be characterized by a positive Eu

anomaly but low Eu contents (Fig. 8). In addition, the granites show varying degrees of REE depletion (Fig. 8). The inhibited dissolution of accessory phases that control the REE budget, such as monazite and zircon, would have a primary control on the REE pattern, although the dilution effect of accumulated feldspars may also have contributed. The enrichment in HREE of some samples is related to the presence of garnet.

Residual Swanson Formation source. Sample K6-Mj01 is a concordant 1 m thick granite sill intrusive into migmatitic gneisses at Marujupu Peak (Fig. 1d) that appears to have a different petrogenesis compared with the other granites. The migmatites in the central Fosdick Mountains preserve the Carboniferous history, and the major melt extraction event is interpreted to be Carboniferous (Korhonen *et al.*, 2009). However, mineral equilibria modeling results indicate that the residual gneisses would be capable of producing up to 12 vol. % melt at the *P*–*T* conditions of the Cretaceous event (Korhonen *et al.*, 2009).

Granite K6-Mj01 has chemical similarities to the Cretaceous granites derived from the Swanson Formation, including similar REE patterns and the presence of inherited zircon. However, this granite has elevated Ba and Sr contents and a correspondingly low Rb/Sr ratio compared with the other Swanson Formation-derived granites, consistent with melting reactions that may have been dominated by plagioclase rather than muscovite or biotite. A residual metasedimentary source, such as the Swanson Formation that had lost most of the melt produced during the Carboniferous event, would have a reduced contribution from biotite or muscovite relative to plagioclase during melt production. This difference would result in lower Rb/Sr and $^{87}Sr/^{86}Sr_{(100Ma)}$ ratios of the Cretaceous granites derived from residual Swanson Formation as compared with granites derived from fertile Swanson Formation.

In addition, the $^{87}Sr/^{86}Sr_{(100Ma)}$ value of K6-Mj01 is slightly less than the inferred Swanson Formation source, which is consistent with only minor involvement of either muscovite or biotite in the melting reactions under conditions of isotopic disequilibrium (Zeng *et al.*, 2005). Disequilibrium melting can occur if the melt is extracted from the source too quickly to allow equilibrium between them to be achieved. The crystallization age of *c.* 102 Ma corresponds closely to the onset of regional extension recorded in the Fosdick migmatite–granite complex (Siddoway, 2008; McFadden *et al.*, 2009, in preparation), suggesting that rapid melt extraction during extensional deformation may have led to disequilibrium between melt and residue.

The experimental results of Koester *et al.* (2002) also support a petrogenetic model that K6-Mj01 was produced from residual Swanson Formation. The composition of the cordierite gneiss starting material used in that study plots
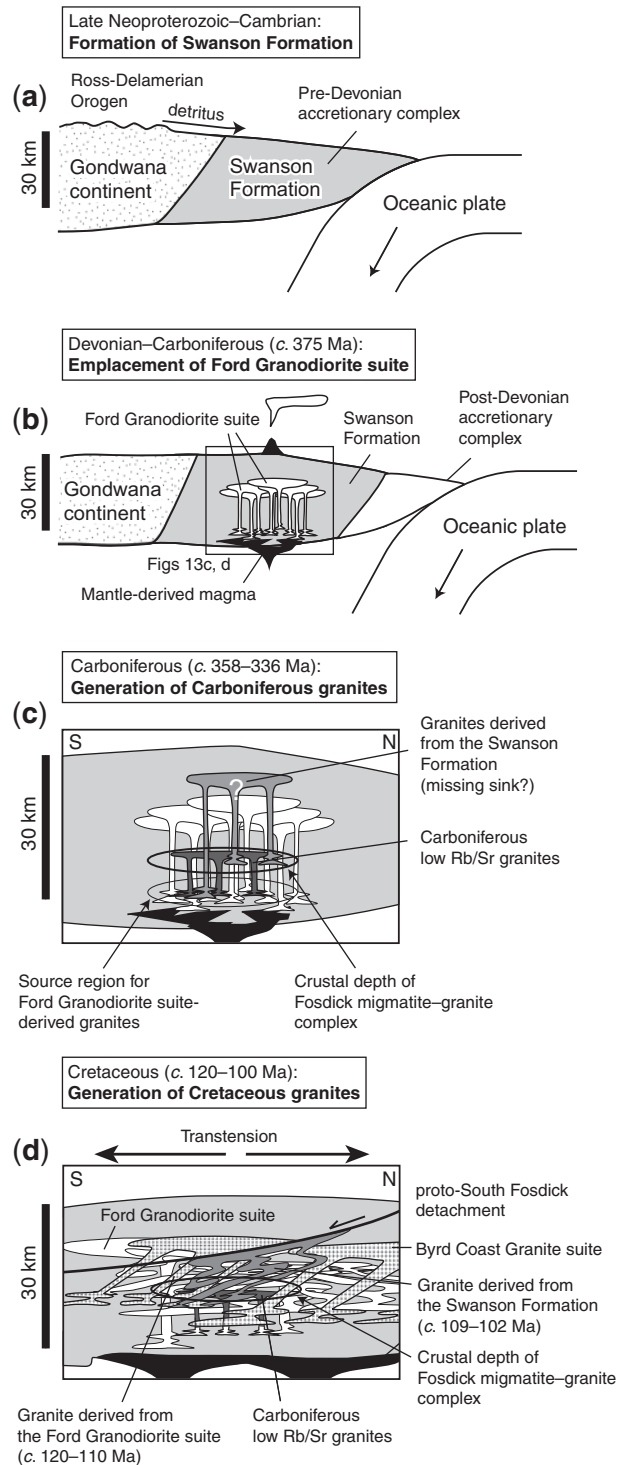
Fig. 13. Schematic model to show the proposed intracrustal differentiation evolution of the Fosdick migmatite–granite complex. (a) Detritus shed off the Ross–Delamerian Orogen accumulated in an accretionary complex, represented in Marie Byrd Land as the Swanson Formation. (b) Arc magmatism associated with subduction along the East Gondwana margin resulted in emplacement of the Ford Granodiorite suite at *c.* 375 Ma. (c) Anatexis of Ford Granodiorite suite plutons at a deeper crustal level resulted in the emplacement of Carboniferous low Rb/Sr granites within the Fosdick migmatite–granite complex. Carboniferous granites derived from the Swanson Formation are sparse, and the sink for these melts is inferred to have been at higher crustal levels than exposed at present. (d) Cretaceous granites sourced from the Ford Granodiorite suite were emplaced within the Fosdick migmatite–granite complex at *c.* 120–110 Ma, and were probably feeder zones for the Byrd Coast Granite suite at higher structural levels. Anatexis of both fertile and residual Swanson Formation sources occurred slightly later (*c.* 109–102 Ma), and the corresponding granites probably had low water contents, consistent with dehydration of the Swanson Formation as the Byrd Coast Granite suite magmas were transferring through the crustal level of the Fosdick migmatite–granite complex. Granites derived from fertile Swanson Formation make up the leucogranite sheeted complex below the South Fosdick detachment (Figs 1d and 2). Additional details on the role of melt transfer and emplacement of the Fosdick migmatite–granite complex have been given by McFadden *et al.* (in press) and (in preparation).

Table 5: Model Nd isotope values of monazite and apatite in Swanson Formation

Mineral:	monazite	monazite	apatite	apatite	Swanson Fm av.*
Source:	I-type granite	S-type granite	I-type granite	S-type granite	
Sm (ppm)	18000†	18000†	175·3†	175·3†	6·9
Nd (ppm)	104000†	104000†	432†	432†	35·8
Sm/Nd	0·1731	0·1731	0·4058	0·4058	0·1927
$^{143}Nd/^{144}Nd_{(500Ma)}$	0·51175‡	0·51138§	0·51175‡	0·51138§	0·51199
$\varepsilon Nd_{(500Ma)}$	−4·7‡	−12·0§	−4·7‡	−12·0§	−7·7
$^{143}Nd/^{144}Nd_{(350Ma)}$	0·51185	0·51148	0·51199	0·51162	0·51172
$\varepsilon Nd_{(350Ma)}$	−6·5	−13·8	−3·8	−11·1	−9·2
$^{143}Nd/^{144}Nd_{(100Ma)}$	0·51203	0·51165	0·51239	0·51202	0·51191
$\varepsilon Nd_{(100Ma)}$	−9·4	−16·7	−2·3	−9·6	−11·68

*This study; Adams *et al.* (2005).
†Data from Zeng *et al.* (2005).
‡Average of I-type granite in Delamerian Orogen (Foden *et al.*, 2002).
§Average of S-type granite in Delamerian Orogen (Foden *et al.*, 2002).

within the field of residual paragneiss compositions from the core of the Fosdick migmatite–granite complex. Granite K6-Mj01 has a similar composition to the experimental glass compositions from that study, although it is slightly displaced towards plagioclase, possibly representing a more cumulate-rich composition (Fig. 10b).

Relationship between Cretaceous granites and Byrd Coast Granite suite: a possible melt sink?

The Cretaceous Byrd Coast Granite suite in the Ford Ranges was emplaced at a higher structural level than the granites and migmatites exposed in the Fosdick migmatite–granite complex (Richard *et al.*, 1994). Sample K6-NU01 located in the hanging wall of the Fosdick migmatite–granite complex (Fig. 1d) has a U–Pb zircon age of *c.* 119 Ma. This age is comparable with ages of some granites within the complex (*c.* 115–98 Ma), and suggests that the Byrd Coast Granite suite may represent the sink for melt generated during the Cretaceous anatectic event. The Sr–Nd isotope compositions of the Byrd Coast Granite suite (this study; Weaver *et al.*, 1992) are comparable with the Cretaceous granites derived from the Ford Granodiorite suite (Fig. 9), supporting the hypothesis that the granites inside the complex represent feeders for the Byrd Coast Granite suite.

The higher SiO_2 contents of the Byrd Coast Granite suite (74–79 normalized wt %) compared with these Cretaceous granites (71–75 normalized wt %) require significant fractionation. The Byrd Coast Granite suite has a range of compositions that are displaced from the other Cretaceous granites toward the feldspar join in the K–(Fe* + Mg + Ti)–(Na + Ca) diagram (Fig. 10a), suggesting that the Byrd Coast Granite suite crystallized from a K_2O-enriched (evolved) liquid in comparison with the granites inside the complex. The prominent negative Eu anomaly in the Byrd Coast Granite suite is also consistent with the fractionation of plagioclase during the evolution of these melts.

Previously, Weaver *et al.* (1992) had proposed that the Byrd Coast Granite suite in the Edward VII Peninsula (Fig. 1b; *c.* 310 km SW of the Fosdick Mountains) formed by partial melting of a Ford Granodiorite source. The emplacement of large, regionally extensive leucogranite intrusions represented by the Byrd Coast Granite suite in Marie Byrd Land implies significant extraction and migration of melts from a deeper Ford Granodiorite suite source to upper crustal levels during the Cretaceous event.

Petrogenetic link between leucosomes and granites in the Fosdick migmatite–granite complex

The genetic link between leucosomes and small-scale granites in migmatites and spatially and temporally related leucogranites has been discussed in previous studies by, for example, Solar & Brown (2001), Brown (2004), Olsen *et al.* (2004) and Hinchey & Carr (2006). Those workers interpreted migmatite horizons as zones of melt generation and magma transfer, and suggested that small-scale granites represent the feeders for shallow-level leucogranite intrusions. The estimated pressure in the Fosdick Mountains for the Carboniferous is 7·5–11·5 kbar and for the Cretaceous event is 6–7·5 kbar (Korhonen *et al.*, 2009), corresponding to depths in the lower to middle crust. Thus, the granites within the Fosdick migmatite–granite complex could represent the feeders for granite melts that coalesced to form larger intrusions in the upper crust.

In this case, leucosomes record former melt flow pathways for melt generated at the structural level exposed to be extracted and incorporated with melt transferring through this crustal level.

The chemical and isotopic data for the paragneisses are comparable with those for the Swanson Formation, consistent with previous interpretations suggesting that the protolith of the paragneiss was the metasedimentary rocks of the Swanson Formation (e.g. Siddoway *et al.*, 2004). Modeling of rock fertilities during the polyphase melting history suggests that the residual paragneiss at Mt. Avers underwent significant melting and melt loss during the Carboniferous event (Korhonen *et al.*, 2009). However, the residual paragneiss could produce additional low-volume melt after the initial melt loss event, so that the remnant melt network preserved as the leucosomes at Mt. Avers may record the Cretaceous melting history. The isotopic compositions of the migmatite components calculated to 100 Ma are similar to the whole-rock paragneiss compositions (Fig. 9), suggesting either that the leucosomes record partial melting during the Cretaceous or that the compositions were homogenized during this high-temperature overprint.

The two leucosome samples from Mt. Avers plot near the experimental glass compositions of Koester *et al.* (2002), and have low Rb/Sr ratios (0·52–0·55) and significantly elevated Ba contents (1356–1467 ppm) compared with the other leucosomes and granites (<700 ppm; Fig. 7). These data are consistent with melt produced from a residual metasedimentary source and a greater contribution from plagioclase. The leucosomes from Mt. Avers have higher Sm/Nd ratios than the paragneiss and the Swanson Formation source (Fig. 12). The negative correlation of Sm/Nd with Sm and Nd, but not P_2O_5, suggests that monazite was retained in the residue or melanosome, similar to the petrogenetic model for the Cretaceous granites derived from the Swanson Formation.

The leucosomes from Mt. Avers and the granite sill at Marujupu Peak (sample K6-Mj01) appear to have a similar paragenesis, indicating that the low melt volume derived from residual Swanson Formation during the Cretaceous event may have accumulated into larger dikes and sills. The compositions of the leucosomes and sill are similar to melt compositions, although the sill has a slightly more cumulate composition and the leucosomes can be modeled as melts with slight enrichment in K_2O and residual biotite (Fig. 10b). These processes are consistent with the interpretation that the sill may represent the accumulation site for melts derived from residual Swanson Formation during the Cretaceous event, and that the leucosomes may be the crystallized in-source melts associated with the final stages of melt production.

In contrast, the leucosome network preserved within the sheeted leucogranite complex preserves no evidence of the older Carboniferous history (Korhonen *et al.*, 2008; McFadden *et al.*, in preparation), suggesting either that the highest structural levels of the Fosdick migmatite–granite complex were subsolidus during the Carboniferous event and therefore provided fertile sources during the Cretaceous or that the high-temperature conditions (>800°C) during the Cretaceous obliterated any evidence for the older history.

Leucosome compositions from paragneiss in the sheeted leucogranite complex show that one sample represents a near-melt composition (sample K6-B48) and two samples have cumulate-rich compositions (K6-Bb44, K6-B5l; Fig. 10b). The cumulate compositions have a positive Eu anomaly, and lower Rb/Sr ratios (Fig. 7) and more depleted REE patterns (Fig. 8) compared with the near-melt leucosome. However, the cumulate leucosomes are typically not as REE-depleted as the Cretaceous granites (Fig. 8). These chemical constraints suggest that the near-melt leucosome may represent a melt that did not undergo significant monazite fractionation and crystallized near the source, whereas the cumulate leucosomes may be part of the remnant melt flow network that fed the ascent conduits for melts that accumulated as the Cretaceous granites. The low Ba contents and Rb/Sr ratios in these samples (Fig. 7) are consistent with derivation from a fertile source.

A single leucosome separated from orthogneiss in the sheeted leucogranite complex (sample K6-B26) has a near-melt composition (Fig. 10a). Extant modeling of the Ford Granodiorite suite suggests that the orthogneiss would produce <5 vol. % melt at the *P–T* conditions of Cretaceous metamorphism (Korhonen *et al.*, 2009). The low melt volumes produced in the orthogneiss would probably not coalesce into an interconnected network capable of large-scale melt extraction, suggesting that the melts that accumulated as the evolved Byrd Coast Granite suite must have been derived from a deeper source. Therefore, the leucosomes in the orthogneiss probably represent melt crystallized at or near the source, and were not part of a significant melt transfer network for Ford Granodiorite suite melts derived from deeper sources that accumulated within and above the Fosdick migmatite–granite complex.

Implications for polyphase intracrustal differentiation in an active continental margin

Accessory phase behavior and evidence for contrasting H_2O content

The presence of inherited zircon cores and the chemical evidence for inhibited monazite dissolution in the Cretaceous granites derived from the Swanson Formation indicate that there is a fundamental control on the behavior of these accessory phases during anatexis. In addition,

the Carboniferous granites do not show evidence for inhibited dissolution of accessory phases, suggesting that the conditions of anatexis were different during the Cretaceous event as compared with the Carboniferous one. The solubility of zircon and monazite into melt are primarily controlled by melt composition, temperature, and water content. Elevated temperatures will enhance the dissolution of these phases into the melt, whereas under dry conditions the solubility of zircon and monazite is greatly inhibited (e.g. Harrison & Watson, 1983; Rapp & Watson, 1986; Montel, 1993). The metamorphic temperatures in the Fosdick migmatite–granite complex estimated from mineral equilibria modeling are >800°C for both the Carboniferous and the Cretaceous events, suggesting that the variation in accessory phase behavior is not related to temperature, but may be related to differences in water content.

Monazite. The chemical and isotopic data for the Cretaceous granites are consistent with inhibited dissolution of monazite into the melt. The solubility of monazite in granitic melts decreases with decreasing water content and is very low under 'dry' conditions (>2 wt % H_2O; Rapp & Watson, 1986). Inhibited dissolution of monazite would account for the depletion of LREE in the Cretaceous granites, as well as the elevated Sm/Nd ratios and $\varepsilon Nd_{(100Ma)}$ relative to the Swanson Formation source. In contrast, the Carboniferous granites show evidence for dissolution of apatite, which is independent of water content in the melt for a range of 0–10 wt % H_2O (Harrison & Watson, 1984; Pichavant *et al.*, 1992; Wolf & London, 1995; Zeng *et al.*, 2005).

Zircon. The implications of calculated zircon saturation temperatures in granites have been investigated by Miller *et al.* (2003). Those workers found that for plutons that lack inherited zircon, T_{Zr} will provide a minimum estimate for magma temperature at a time before extensive crystallization, effectively upon emplacement. This situation applies to the Carboniferous granites, which lack inherited zircon. Independent of the granite source, T_{Zr} estimates for these granites range between 815 and 785°C (Table 2), consistent with the metamorphic temperatures estimated from the host gneisses. In addition, accumulation of early crystallized biotite and plagioclase will increase the compositional parameter M and lower estimates of T_{Zr}, so that these temperatures are probably the minimum temperatures at the time of emplacement in the Fosdick migmatite–granite complex. In contrast, the presence of inherited zircon indicates that part of the total Zr concentration in the granite would have been incorporated in the inherited zircon crystals rather than dissolved in the melt, and therefore T_{Zr} will be a maximum temperature estimate (Miller *et al.*, 2003). The T_{Zr} estimates for the Cretaceous granites with inherited zircon range between 735 and 665°C,

suggesting that the Cretaceous granites may have been produced at relatively low temperatures. However, T_{Zr} estimates for Cretaceous granites that lack inherited zircon (C5-Is54 and K6-Mt38) are 810–775°C, suggesting either that the Cretaceous granites crystallized through a wide temperature range or that some temperature estimates may be spurious. An important consideration is that the zircon saturation thermometer of Watson & Harrison (1983) is calibrated for melts with >2 wt % H_2O, therefore T_{Zr} estimates from a 'dry' melt are beyond the calibration of the thermometer and may not be accurate. In addition, the results from Harrison & Watson (1983; reviewed by Hanchar & Watson, 2003) indicate that pre-existing zircon could survive an anatectic event if the granitic melts were 'dry'. These observations suggest that the Cretaceous granites derived from the Swanson Formation probably had much lower water contents (<2 wt %) than the other granites in the Fosdick migmatite–granite complex.

Devonian–Carboniferous intracrustal differentiation

The petrogenetic models for the Carboniferous granites and the metamorphic constraints from the host gneisses reveal a simple model of intracrustal differentiation for the Devonian–Carboniferous event that is best preserved in the central Fosdick Mountains. High-temperature metamorphism at *c.* 370–340 Ma post-dates the main pulse of emplacement of Ford Granodiorite suite magmas during Andean-style convergence at *c.* 375 Ma (Richard & Kimbrough, 1991; Pankhurst *et al.*, 1998; Korhonen *et al.*, 2008; Siddoway & Fanning, 2009; Fig. 13b).

Chemical constraints indicate that the Ford Granodiorite suite was the principal source for the Carboniferous granites emplaced within the Fosdick migmatite–granite complex. The granites are derived by anatexis of the Ford Granodiorite suite, consistent with granite crystallization ages (*c.* 358–336 Ma) that post-date the main episode of magmatism (Fig. 13c). However, at the conditions of peak metamorphism recorded in the Fosdick migmatite–granite complex, the Ford Granodiorite suite would produce <5 vol. % melt (Korhonen *et al.*, 2009). Thus, the Carboniferous granites derived from the Ford Granodiorite suite were probably sourced from a deeper crustal level than that exposed at present (Fig. 13c). The elevated Sr and low Rb contents in the granites are consistent with the mineral equilibria modeling results that show significant melt production (>10 vol. %) at conditions above biotite stability, probably involving hornblende and plagioclase. The compositions of the granites are similar to melt compositions with accumulation of early crystallized biotite and plagioclase. Granites with accumulated phases typically show chemical and isotopic evidence for increased apatite dissolution.

Based on the results from this study, Carboniferous granites derived from the Swanson Formation are not widely exposed in the Fosdick migmatite–granite complex, although the Swanson Formation would have been a fertile source. Mineral equilibria modeling of the Swanson Formation protolith shows that it would produce 4–25 vol. % melt by biotite breakdown at the conditions of Carboniferous metamorphism (Korhonen et al., 2009). Melt-producing reactions involving biotite are consistent with the chemistry of one Carboniferous granite of this study, which is interpreted to have been derived from the Swanson Formation. However, significant melt loss is required to preserve the high-grade assemblages in the migmatites (Powell & Downes, 1990; Brown, 2002; White & Powell, 2002; Diener et al., 2008; Brown & Korhonen, 2009; Korhonen et al., 2009). The transfer of melt to shallower crustal levels than now exposed may account for the relative scarcity of granites derived from the Swanson Formation within the exposed level of the Fosdick migmatite–granite complex (Fig. 13c).

Cretaceous intracrustal differentiation

The second anatectic event recorded in the Fosdick migmatite–granite complex appears to have been a two-stage process. Cretaceous granites (c. 120–110 Ma) derived from Ford Granodiorite suite, emplaced within and above the exposed level of the Fosdick migmatite–granite complex, represent the first stage of the Cretaceous differentiation event (Fig. 13d). However, at the conditions of Cretaceous metamorphism, the Ford Granodiorite suite is not a fertile source (Korhonen et al., 2009). Therefore, the source for the Cretaceous granites that accumulated within the Fosdick migmatite–granite complex is inferred to have been at a deeper level, similar to the petrogenetic model for the Carboniferous granites.

The regionally exposed Byrd Coast Granite suite also has chemical and isotopic compositions consistent with derivation from the Ford Granodiorite suite, although these granites have highly evolved compositions (Weaver et al., 1992; this study). These results suggest that the Fosdick migmatite–granite complex was mainly a transfer zone for melts derived from the Ford Granodiorite suite that accumulated at shallower crustal levels than the Byrd Coast Granite suite (Fig. 13d).

The second stage of the differentiation process corresponds to the anatexis of both fertile and residual Swanson Formation sources. The granites (c. 109–102 Ma) within the sheeted leucogranite complex below the South Fosdick detachment appear to be evolved melts that formed mainly by muscovite or biotite breakdown of fertile sources. These melts, however, probably had low water contents, as suggested by the chemical evidence for inhibited monazite dissolution and the presence of inherited zircon cores. Only granites sourced from the Swanson Formation show evidence for low water contents,

suggesting that the Swanson Formation may have been dehydrated prior to anatexis as granites derived from the Ford Granodiorite suite were transferring through or accumulating above the now exposed level of the Fosdick migmatite–granite complex. The leucosomes in paragneiss within the sheeted leucogranite complex correspond to both near-melt compositions that probably crystallized near the source and cumulate compositions that may represent part of the remnant melt flow network that fed the ascent conduits for melts that accumulated as the Cretaceous granites.

Leucosomes and a small-scale granite sill within the deeper structural levels of the Fosdick migmatite–granite complex correspond to the remnant melt network derived from the residual Swanson Formation. The sill may represent a melt flow conduit for these low-volume melts, whereas the leucosomes may be the crystallized in-source melts associated with the final stages of melt production. The isotopic composition and crystallization age of the sill suggest disequilibrium between the melt and residue, which is permissible evidence that the rate of melt extraction during extensional deformation exceeded the rate of accessory phase dissolution.

The crystallization ages of the granites derived from the Swanson Formation are systematically younger than the ages of the Cretaceous granites derived from the Ford Granodiorite suite. McFadden et al. (in preparation) have described a similar age distribution with granite crystallization ages in the deeper structural level ('western Ochs Glacier suite') ranging from c. 115 to 105 Ma, and granite crystallization ages in the upper structural level ('South Fosdick detachment zone suite') ranging from c. 109 to 102 Ma. These results suggest that anatexis of the Ford Granodiorite suite, melt transfer through the Fosdick migmatite–granite complex, and accumulation and crystallization of the Byrd Coast Granite suite at higher structural levels initiated just prior to the anatexis of the Swanson Formation. High-grade metamorphism and anatexis of the Swanson Formation occurred during a transition from tectonic convergence to extension at c. 105 Ma (Siddoway et al., 2004; Siddoway, 2008; McFadden et al., in preparation). The granites derived from the Swanson Formation make up the horizontal sheeted leucogranite complex, and accumulated at deeper levels than the crystallizing Byrd Coast granite. Accumulation of these melts probably facilitated melt-induced weakening of the crust, the formation of the South Fosdick detachment, and rapid cooling between c. 105 and 94 Ma (Richard et al., 1994; McFadden et al., in preparation).

Intracrustal differentiation along the East Gondwana margin

Understanding of the evolution of the East Gondwana margin comes mainly through studies from the Western Province of New Zealand (e.g. Ireland & Gibson, 1998;

Muir *et al.*, 1998; Mortimer *et al.*, 1999; Adams, 2008; Tulloch *et al.*, 2009) and the Lachlan and New England fold belts of eastern Australia (e.g. Murray *et al.*, 1987; Chappell, 1994; Foster & Gray, 2000; Collins, 2002; Kemp *et al.*, 2007, 2009). Although previous investigations have resolved the magmatic record preserved in North Victoria Land and Marie Byrd Land of West Antarctica (e.g. Borg *et al.*, 1987; Weaver *et al.*, 1991; Cooper & Tulloch, 1992; Stump, 1995; Pankhurst *et al.*, 1998; Mukasa & Dalziel, 2000), this area remains a less studied, but critical segment of the Gondwana margin that links Andean-style (e.g. Vaughan & Pankhurst, 2008) to Lachlan-style (e.g. Foster & Gray, 2000; Glen, 2005) circum-Pacific orogenesis.

Recent work by Tulloch *et al.* (2009) along the once-contiguous New Zealand sector of the East Gondwana margin has revealed a highly episodic emplacement history between *c.* 371 and 305 Ma. Voluminous Paleozoic magmatism is recorded by two pairs of S- and I-type magmatic suites, with the major pulse at *c.* 371–358 Ma and emplacement of the Karamea suite, and a minor pulse at *c.* 355–337 Ma. This history corresponds closely to the Devonian–Carboniferous history preserved in and above the now exposed Fosdick migmatite–granite complex, where S- and I-type granites of similar chemistry were emplaced during an interval of *c.* 369–343 Ma (Fig. 13b and c; Richard & Kimbrough, 1991; Siddoway & Fanning, 2009; Tulloch *et al.*, 2009; this study).

There are also compelling similarities between the Jurassic–Cretaceous history preserved in New Zealand and that in Marie Byrd Land. The Jurassic–Cretaceous magmatic arc along the East Gondwana margin is represented by the calc-alkaline, I-type Median Batholith in New Zealand, emplaced mainly between *c.* 145 and 120 Ma (Fig. 1b; Muir *et al.*, 1998; Mortimer *et al.*, 1999; Tulloch & Kimbrough, 2003). Tectonic reconstructions show continuity of the magmatic arc into eastern Marie Byrd Land with crystallization ages ranging between *c.* 124 and *c.* 96 Ma (Fig. 1b; Pankhurst *et al.*, 1998; Mukasa & Dalziel, 2000).

The Ford Ranges of Marie Byrd Land are located inboard of the Jurassic–Cretaceous calc-alkaline magmatic arc (Fig. 1b), and the alkalic magmatism recorded by the Byrd Coast Granite suite has been attributed to back-arc extension (Weaver *et al.*, 1992, 1994; Mukasa & Dalziel, 2000; Siddoway, 2008). The results from this study suggest that anatexis of the Swanson Formation may slightly post-date the anatexis of the Ford Granodiorite and emplacement of the Byrd Coast Granite suite (Fig. 13d). Potential correlatives to this differentiation event may be the Separation Point and Rahu suites in New Zealand, which also form the inboard part of the magmatic arc and have similar emplacement ages (Tulloch, 1983; Allibone *et al.*, 2007). The Separation Point plutons were emplaced between *c.* 118 and 111 Ma (Kimbrough *et al.*, 1994; Muir

et al., 1994) and have I-type chemistry (e.g. Allibone *et al.*, 2007). The Rahu suite contains inherited zircon from the Greenland Group, but rim ages suggest granite crystallization at *c.* 115–110 Ma (Waight *et al.*, 1997). The granites associated with this suite are both I- and S-types.

SUMMARY

The Fosdick migmatite–granite complex in Marie Byrd Land, West Antarctica records the processes and conditions associated with two cycles of intracrustal differentiation along the active continental margin of East Gondwana. The close correspondence in timing and chemical evolution to the Western Province of New Zealand suggests that the polyphase intracrustal differentiation history preserved in the Fosdick migmatite–granite complex may provide significant insight into the processes of large-scale intracrustal differentiation along the East Gondwana margin.

The first period of high-temperature metamorphism during the Devonian–Carboniferous slightly post-dates the main pulse of emplacement of calc-alkaline arc magmas during Andean-style convergence (Fig. 13b). This event resulted in anatexis of calc-alkaline plutons derived from a deeper crustal level and their host metasedimentary rocks (Fig. 13c). Granites derived from each of these two sources were emplaced within the Fosdick migmatite–granite complex, although the presence of residual paragneisses and scarcity of granites derived from the metasedimentary rocks suggest that significant quantities of melt escaped to shallower crustal levels than now exposed (Fig. 13c). This event stabilized the Swanson Formation accretionary complex and associated Ford Granodiorite suite as continental crust.

The second period of high-temperature metamorphism during the Cretaceous was a two-stage evolution. Constraints from granite chemistry suggest that the Fosdick migmatite–granite complex was probably a transfer zone for evolved melts derived from fertile Devonian–Carboniferous calc-alkaline plutons. These melts are represented by the Cretaceous Byrd Coast Granite suite plutons at higher structural levels (Fig. 13d). Anatexis of both fertile and residual metasedimentary rocks immediately followed (Fig. 13d); chemical and isotopic compositions indicate that these melts had low water contents, suggesting that portions of the crust may have been dehydrated prior to anatexis as the Byrd Coast Granite suite was transferring through or accumulating above the now exposed level of the Fosdick migmatite–granite complex. The granites derived from the metasedimentary rocks make up a prominent horizontal sheeted leucogranite complex. The accumulation of these melts probably facilitated melt-induced weakening of the crust during the transition from regional shortening to regional extension at *c.* 100 Ma, the formation of the detachment structure, and rapid

exhumation of the Fosdick migmatite–granite complex (Richard *et al.*, 1994; McFadden *et al.*, in preparation).

ACKNOWLEDGEMENTS

SUPPLEMENTARY DATA

Supplementary data for this paper are available at *Journal of Petrology* online.

REFERENCES

Adams, C. J. (1986). Geochronological studies of the Swanson Formation of Marie Byrd Land, West Antarctica, and the correlation with northern Victoria Land, East Antarctica and the South Island, New Zealand. *New Zealand Journal of Geology and Geophysics* **29**, 345–358.

Adams, C. J. (1987). Geochronology and granite terranes in the Ford Ranges, Marie Byrd Land, West Antarctica. *New Zealand Journal of Geology and Geophysics* **30**, 51–72.

Adams, C. J. (2004). Rb–Sr age and strontium isotopic characteristics of the Greenland Group, Buller terrane, New Zealand, and correlations at the East Gondwana margin. *New Zealand Journal of Geology and Geophysics* **47**, 189–200.

Adams, C. J. (2008). Geochronology of Paleozoic terranes at the Pacific Ocean margin of Zealandia. *Gondwana Research* **13**, 250–258.

Adams, C. J., Pankhurst, R. J., Mass, R. & Millar, I. L. (2005). Nd and Sr isotope signatures of metasedimentary rocks around the South Pacfic margin and implications for their provenance. In: Vaughan, A. P. M., Leat, P. T. & Pankhurst, R. J. (eds) *Terrane Processes at the Margins of Gondwanaland. Geological Society, London, Special Publications* **246**, 113–141.

Allibone, A. H., Turnball, I. M., Tulloch, A. J. & Cooper, A. F. (2007). Plutonic rocks of the Median Batholith in southwest Fiordland,

New Zealand: field relations, geochemistry, and correlation. *New Zealand Journal of Geology and Geophysics* **50**, 283–314.

Ayers, M. & Harris, N. (1997). REE fractionation and Nd-isotope disequilibrium during crustal anatexis: constraints from Himalayan leucogranites. *Chemical Geology* **139**, 247–267.

Baker, D. R., Conte, A. M., Freda, C. & Ottolini, L. (2002). The effect of halogens on Zr diffusion and zircon dissolution in hydrous metaluminous granitic melts. *Contributions to Mineralogy and Petrology* **142**, 666–678.

Black, L. P., Kamo, S. L., Allen, C. M., Aleinikoff, J. N., Davis, D. W., Korsch, R. J. & Foudoulis, C. (2003). TEMORA 1: a new standard for Phanerozoic U–Pb geochronology. *Chemical Geology* **200**, 155–170.

Borg, S. G., Stump, E., Chappell, B. W., McCulloch, M. T., Wyborn, D., Armstrong, R. L. & Holloway, J. R. (1987). Granitoids of northern Victoria Land, Antarctica: implications of chemical and isotopic variations to regional crustal structure and tectonics. *American Journal of Science* **287**, 127–169.

Boyd, F. R. & Mertzmann, S. (1987). Composition and structure of the Kaapvaal lithosphere, Southern Africa. In: Mysen, B. O. (ed.) *Magmatic Processes: Physiochemical Principles. Geochemical Society Special Publication* **1**, 13–24.

Brown, M. (2002). Retrograde processes in migmatites and granulites revisited. *Journal of Metamorphic Geology* **20**, 25–40.

Brown, M. (2004). The mechanism of melt extraction from lower continental crust of orogens. *Transactions of the Royal Society of Edinburgh: Earth Sciences* **95**, 35–48.

Brown, M. (2009). The spatial and temporal patterning of the deep crust and implications for the process of melt extraction. *Philosophical Transactions of the Royal Society of London, Series A*, doi:10.1098/rsta.2009.0200.

Brown, M. & Korhonen, F. J. (2009). Some remarks on melting and extreme metamorphism of crustal rocks. In: Gupta, A. K. & Dasgupta, S. (eds) *Physics and Chemistry of the Earth's Interior.* New Delhi: Indian National Science Academy, Springer (India), pp. 67–87.

Brown, M. & Rushmer, T. (eds) (2006). *Evolution and Differentiation of the Continental Crust.* Cambridge: Cambridge University Press.

Chang, Z., Vervoort, J. D., McClelland, W. C. & Knaack, C. (2006). U–Pb dating of zircon by LA-ICP-MS. *Geochemistry, Geophysics, Geosystems* **7**, doi:10.1029/2005GC001100.

Chappell, B. W. (1994). Lachlan and New England: fold belts of contrasting magmatic and tectonic development. *Journal and Proceedings of the Royal Society of New South Wales* **127**, 47–59.

Collins, W. J. (2002). Hot orogens, tectonic switching, and creation of continental crust. *Geology* **30**, 535–538.

Cooper, R. A. & Tulloch, A. J. (1992). Early Paleozoic terranes in New Zealand and their relationship to the Lachlan fold belt. *Tectonophysics* **214**, 129–144.

Davidson, J. P. & Arculus, R. J. (2006). The significance of Phanerozoic arc magmatism in generating continental crust. In: Brown, M. & Rushmer, T. (eds) *Evolution and Differentiation of the Continental Crust.* New York: Cambridge University Press, pp. 135–172.

Day, J. M. D., Pearson, D. G. & Hulbert, L. J. (2008). Rhenium–osmium and platinum-group element constraints on the origin and evolution of the 1·27 Ga Muskox layered intrusion. *Journal of Petrology* **49**, 1255–1295.

Diener, J. F. A., White, R. W. & Powell, R. (2008). Granulite facies metamorphism and subsolidus fluid-absent reworking, Strangways Range, Arunta Block, central Australia. *Journal of Metamorphic Geology* **26**, 603–622.

Foden, J. D., Elburg, M. A., Turner, S. P., Sandiford, M., O'Callaghan, J. & Mitchell, S. (2002). Granite production in the

Delamerian Orogen, South Australia. *Journal of the Geological Society, London* **159**, 557–575.

Foster, D. A. & Gray, D. R. (2000). The structure and evolution of the Lachlan Fold Belt (Orogen) of eastern Australia. *Annual Review of Earth and Planetary Sciences* **28**, 47–80.

Glen, R. A. (2005). The Tasmanides of eastern Australia. In: Vaughan, A. P. M., Leat, P. T. & Pankhurst, R. J. (eds) *Terrane Processes at the Margins of Gondwanaland. Geological Society, London, Special Publication* **246**, 23–96.

Hanchar, J. M. & Watson, E. B. (2003). Zircon saturation thermometry. In: Hanchar, J. M. & Hoskin, P. W. O. (eds) *Zircon. Mineralogical Society of America and Geochemical Society, Reviews in Mineralogy and Geochemistry* **53**, 89–112.

Harrison, T. M. & Watson, E. B. (1983). Kinetics of zircon dissolution and zirconium diffusion in granitic melts of variable water content. *Contributions to Mineralogy and Petrology* **84**, 67–72.

Harrison, T. M. & Watson, E. B. (1984). The behaviour of apatite during crustal anatexis: equilibrium and kinetic considerations. *Geochimica et Cosmochimica Acta* **48**, 1467–1477.

Harrison, T. M., Aleinikoff, J. N. & Compston, W. (1987). Observations and controls on the occurrence of inherited zircon in Concord-type granitoids, New Hampshire. *Geochimica et Cosmochimica Acta* **51**, 2549–2558.

Hinchey, A. M. & Carr, S. D. (2006). The S-type Ladybird leucogranite suite of southeastern British Columbia: Geochemical and isotopic evidence for a genetic link with migmatite formation in the North American basement gneisses of the Monashee complex. *Lithos* **90**, 223–248.

Ireland, T. R. & Gibson, G. M. (1998). SHRIMP monazite and zircon geochronology of high-grade metamorphism in New Zealand. *Journal of Metamorphic Geology* **16**, 149–167.

Ireland, T. R., Flöttman, T., Fanning, C. M., Gibson, G. M. & Preiss, V. W. (1998). Development of the early Paleozoic Pacific margin of Gondwana from detrital-zircon ages across the Delamerian orogen. *Geology* **26**, 243–246.

Kelsey, D. E., Clark, C. & Hand, M. (2008). Thermobarometric modelling of zircon and monazite growth in melt-bearing systems: examples using model metapelitic and metapsammitic granulites. *Journal of Metamorphic Geology* **26**, 199–212.

Kemp, A. I. S., Hawkesworth, C. J., Foster, G. L., Paterson, B. A., Woodhead, J. D., Hergt, J. M., Gray, C. M. & Whiteouse, M. J. (2007). Magmatic and crustal differentiation history of granitic rocks from Hf–O isotopes in zircon. *Science* **315**, 980–983.

Kemp, A. I. S., Hawkesworth, C. J., Collins, W. J., Gray, C. M., Blevin, P. L. & Edinburgh Ion Microprobe Facility. (2009). Isotopic evidence for rapid continental growth in an extensional accretionary orogen: the Tasmanides, eastern Australia. *Earth and Planetary Science Letters* **284**, 455–466.

Kimbrough, D. L., Tulloch, A. J., Coombs, D. S., Landis, C. A., Johnston, M. R. & Mattinson, J. M. (1994). Uranium–lead zircon ages from the Median Tectonic Zone, New Zealand. *New Zealand Journal of Geology and Geophysics* **37**, 393–419.

Koester, E., Pawley, A. R., Fernandes, L. A. D., Porcher, C. C. & Soliarni, E., Jr (2002). Experimental melting of cordierite gneiss and the petrogenesis of syntranscurrent peraluminous granites in southern Brazil. *Journal of Petrology* **43**, 1595–1616.

Korhonen, F. J., Brown, M. & Siddoway, C. S. (2007). Petrologic and geochronological constraints on the polymetamorphic evolution of the Fosdick migmatite dome, Marie Byrd Land, West Antarctica. In: Cooper, A. K., Raymond, C. R., *et al.* (eds) *Antarctica: A Keystone in a Changing World—Online Proceedings of the 10th ISAES. US Geological Survey Open-File Report* **2007-1047**, Extended Abstract 049.

World Wide Web Address: http://pubs.usgs.gov/of/2007/1047/ea/of2007-1047ea049.pdf.

Korhonen, F. J., Brown, M., Saito, S. & Siddoway, C. S. (2008). The link between migmatites and granites: polyphase melting and granite magmatism during the tectonic evolution of the Fosdick migmatite dome, West Antarctica. , In: Abstracts of the 33rd International Geologic Congress, 6-14 August, Oslo, Norway. Abstract #: MPN12812L.

Korhonen, F. J., Saito, S., Brown, M. & Siddoway, C. S. (2009). Modeling multiple melt loss events in the evolution of an active continental margin. *Lithos*, Special Volume, doi:10.1016/j.lithos.2009.09.004.

Kretz, R. (1983). Symbols for rock-forming minerals. *American Mineralogist* **68**, 277–279.

Ludwig, K. R. (1999). *Isoplot/Ex Version 2.00: a Geochronological Toolkit for Microsoft Excel. Berkeley Geochronology Center Special Publication* **1a**, 46 p.

Luyendyk, B. P. (1995). Hypothesis for Cretaceous rifting of East Gondwana caused by subducted slab capture. *Geology* **23**, 373–376.

McFadden, R., Siddoway, C. S., Teyssier, C., Fanning, C. M. & Kruckenberg, S. C. (2007). Cretaceous oblique detachment tectonics in the Fosdick Mountains, Marie Byrd Land, Antarctica. In: Cooper, A. K., Raymond, C. R. *et al.* (eds) *Antarctica: A Keystone in a Changing World—Online Proceedings of the 10th ISAES. US Geological Survey Open-File Report* **2007-1047**, Short Research Paper 046, doi:10.3133/of 2007-1047.srp046.

McFadden, R., Teyssier, C., Siddoway, C. S., Whitney, D. L. & Fanning, C. M. (2009). Cretaceous Oblique dilation, melt transfer, and gneiss dome emplacement. *Geology* **38**, 375–378.

McFadden, R., Siddoway, C. S., Teyssier, C. & Fanning, C. M. (in preparation). Cretaceous intracontinental extension in the Fosdick Mountains migmatite–granite complex. West Antarctica: *Tectonics*.

Miller, C. F., McDowell, S. M. & Mapes, R. W. (2003). Hot and cold granites? Implications of zircon saturation temperatures and preservation of inheritance. *Geology* **31**, 529–532.

Montel, J. M. (1993). A model for monazite/melt equilibrium and application to the generation of granitic magmas. *Chemical Geology* **110**, 127–146.

Mortimer, N., Tulloch, A. J., Spark, R. N., Walker, N. W., Ladley, E., Allibone, A. & Kimbrough, D. L. (1999). Overview of the Median Batholith, New Zealand: a new interpretation of the geology of the Median Tectonic Zone and adjacent rocks. *Journal of African Earth Sciences* **29**, 257–268.

Muir, R. J., Ireland, T. R., Weaver, S. D. & Bradshaw, J. D. (1994). Ion microprobe U–Pb zircon dating of granitic magmatism in the Western Province of South Island, New Zealand. *Chemical Geology* **113**, 171–189.

Muir, R. J., Ireland, T. R., Weaver, S. D., Bradshaw, J. D., Evans, J. A., Eby, G. N. & Shelley, D. (1998). Geochronology and geochemistry of a Mesozoic magmatic arc system, Fiordland, New Zealand. *Journal of the Geological Society, London* **155**, 1037–1053.

Mukasa, S. B. & Dalziel, I. W. D. (2000). Marie Byrd Land, West Antarctica: evolution of Gondwana's Pacific margin constrained by zircon U–Pb geochronology and feldspar common-Pb isotopic compositions. *Geological Society of American Bulletin* **112**, 611–627.

Murray, C. G., Fergusson, C. L., Flood, P. G., Whitaker, W. G. & Korsch, R. J. (1987). Plate tectonic model for the Carboniferous evolution of the New England fold belt. *Australian Journal of Earth Sciences* **34**, 213–236.

Nabelek, P. I. & Glascock, M. D. (1995). REE-depleted leucogranites, Black Hills, South Dakota: a consequence of disequilibrium melting of monazite-bearing schists. *Journal of Petrology* **36**, 1055–1071.

Olsen, S. N., Marsh, B. D. & Baumgartner, L. P. (2004). Modelling midcrustal migmatite terrains as feeder zones for granite plutons: the competing dynamics of melt transfer by bulk versus porous flow. *Transactions of the Royal Society of Edinburgh: Earth Sciences* **95**, 49–58.

Otamendi, J. E., Ducea, M. N., Tibaldi, A. M., Bergantz, G. W., de la Rosa, J. D. & Vujovich, G. I. (2009). Generation of tonalitic and dioritic magmas by coupled partial melting of gabbroic and meta-sedimentary rocks within the deep crust of the Famatinian magmatic arc, Argentina. *Journal of Petrology* **50**, 841–873.

Pankhurst, R. J., Weaver, S. D., Bradshaw, J. D., Storey, B. C. & Ireland, T. R. (1998). Geochronology and geochemistry of pre-Jurassic superterranes in Marie Byrd Land, Antarctica. *Journal of Geophysical Research* **103**, 2529–2547.

Patiño Douce, A. E. & Harris, N. (1998). Experimental constraints on Himalayan anatexis. *Journal of Petrology* **39**, 689–710.

Pichavant, M., Montel, J.-M. & Richard, L. R. (1992). Apatite solubility in peraluminous liquids: experimental data and an extension of the Harrison–Watson model. *Geochimica et Cosmochimica Acta* **56**, 3855–3861.

Powell, R. & Downes, J. (1990). Garnet porphyroblast-bearing leucosomes in metapelites: mechanisms and an example from Broken Hill, Australia. In: Ashworth, J. R. & Brown, M. (eds) *High Temperature Metamorphism and Crustal Anatexis*. London: Unwin Hyman, pp. 105–123.

Rapp, R. P. & Watson, E. B. (1986). Monazite solubility and dissolution kinetics: implications for the thorium and light rare earth element chemistry of felsic magmas. *Contributions to Mineralogy and Petrology* **94**, 304–316.

Ryerson, F. J. & Watson, E. B. (1987). Rutile saturation in magmas: implications for Ti–Nb–Ta depletion in island-arc basalts. *Earth and Planetary Science Letters* **86**, 225–239.

Richard, S. M. & Kimbrough, D. L. (1991). Mesozoic plutonism, metamorphism of Paleozoic rocks, and cooling related to Gondwana rifting, Fosdick Mountains region, West Antarctica. *Geological Society of America, Abstracts with Programs* **23**(5), A364.

Richard, S. M., Smith, C. H., Kimbrough, D. K., Fitzgerald, P. G., Luyendyk, B. P. & McWilliams, M. O. (1994). Cooling history of the northern Ford Ranges, Marie Byrd Land, West Antarctica. *Tectonics* **13**, 837–857.

Rudnick, R. L. (ed.) (2003). *The Crust, Treatise on Geochemistry, 3.* Oxford: Elsevier–Pergamon.

Saito, S., Arima, M., Nakajima, T., Misawa, K. & Kimura, J.-I. (2007). Formation of distinct granitic magma batches by partial melting of hybrid lower crust in the Izu arc collision zone, central Japan. *Journal of Petrology* **48**, 1761–1791.

Sawyer, E. W. (2008). *Atlas of Migmatites. The Canadian Mineralogist Special Publication* **9**.

Siddoway, C. (2008). Tectonics of the West Antarctic Rift System: new light on the history and dynamics of distributed intracontinental extension. In: Cooper, A. K., Barrett, P. J., Stagg, H., Storey, B., Stump, E., Wise, W. & the 10th International Team (eds) *Antarctica: A Keystone in a Changing World*. Washington, DC: National Academies Press, pp. 91–114.

Siddoway, C. S. & Fanning, C. M. (2009). Continental tectonics of the East Gondwana margin: Timing and significance of middle Paleozoic orogenesis in West Antarctica. *Tectonophysics*, doi:10.1016/j.tecto.2009.04.021.

Siddoway, C. S., Richard, S., Fanning, C. M. & Luyendyk, B. P. (2004). Origin and emplacement mechanisms for a middle Cretaceous gneiss dome, Fosdick Mountains, West Antarctica. In: Whitney, D. L., Teyssier, C. T. & Siddoway, C. (eds) *Gneiss Domes in Orogeny. Geological Society of America, Special Papers* **380**, 267–294.

Siddoway, C. S., Sass, L. C. & Esser, R. P. (2005). Kinematic history of western Marie Byrd Land, West Antarctica: direct evidence from Cretaceous mafic dykes. In: Vaughan, A. P. M., Leat, P. T. & Pankhurst, R. J. (eds) *Terrane Processes at the Margins of Gondwana. Geological Society, London, Special Publications* **246**, 417–438.

Siddoway, C. S., Fanning, C. M., Kruckenberg, S. C. & Fadrhonc, S. C. (2006). U–Pb SHRIMP investigation of the timing and duration of melt production and migration in a Pacific margin gneiss dome, Fosdick Mountains, Antarctica. *Fall AGU Meeting, San Francisco. EOS Transactions, American Geophysical Union* **88**, V23D–0661.

Skjerlie, K. P. & Johnston, A. D. (1993). Fluid-absent melting behavior of an F-rich tonalitic gneiss at mid-crustal pressures: implications for the generation of anorogenic granites. *Journal of Petrology* **34**, 785–815.

Solar, G. S. & Brown, M. (2001). Petrogenesis of migmatites in Maine, USA: possible source of peraluminous leucogranite in plutons? *Journal of Petrology* **42**, 789–823.

Squire, R. J., Campbell, I. H., Allen, C. M. & Wilson, C. J. L. (2006). Did the Transgondwanan Supermountain trigger the explosive radiation of animals on Earth? *Earth and Planetary Science Letters* **250**, 116–133.

Storey, B. C., Leat, P. T., Weaver, S. D., Pankhurst, J. D. & Kelley, S. (1999). Mantle plumes and Antarctic–New Zealand rifting: Evidence from mid-Cretaceous mafic dykes. *Journal of the Geological Society, London* **156**, 659–671.

Stump, E. (1995). *The Ross Orogen of the Transantarctic Mountains.* Cambridge: Cambridge University Press, 284 p.

Tatsumi, Y. (2000). Continental crust formation by crustal delamination in subduction zones and complementary accumulation of the enriched mantle I component in the mantle. *Geochemistry, Geophysics, Geosystems* **1**, doi:10.1029/2000GC000094.

Taylor, S. R. & McLennan, S. M. (1985). *The Continental Crust: its Composition and Evolution.* Oxford: Blackwell Scientific, 311 p.

Tulloch, A. J. (1983). Granitoid rocks of New Zealand : a brief review. p. 5–20. In: Roddick, J. A. (ed.) *Circum-Pacific plutonic terranes. Boulder, Co.: Geological Society of America* **159**, Memoir: Geological Society of America.

Tulloch, A. J. & Kimbrough, D. L. (2003). Paired plutonic belts in convergent margins and the development of high Na, Al, Sr, low Y magmatism: The Peninsular Ranges Batholith of California and the Median Batholith of New Zealand. In: *Geological Society of America, Special Papers* **374**, 275–295.

Tulloch, A. J., Beggs, M., Kula, J., Spell, T. & Mortimer, N. (2006). Cordillera Zealandia, the Sisters Shear Zone and their influence on the early development of the Great South Basin. *New Zealand Petroleum Conference proceedings*. Wellington: Ministry of Economic Development.

Tulloch, A. J., Ramezani, J., Kimbrough, D. L., Faure, K. & Allibone, A. H. (2009). U–Pb geochronology of Paleozoic plutonism in western New Zealand: implications for S-type granite generation and growth of the east Gondwana margin. *Geological Society of America Bulletin* **121**, 1236–1261.

Turner, S., Foden, J., Sandiford, M. & Bruce, D. (1993). Sm–Nd isotopic evidence for the provenance of sediments from the Adelaide Fold Belt and southeastern Australia with implications for episodic crustal addition. *Geochimica et Cosmochimica Acta* **57**, 1837–1856.

Vaughan, A. P. M. & Pankhurst, R. J. (2008). Tectonic overview of the West Gondwana margin. *Gondwana Research* **13**, 150–162.

Waight, T. E., Weaver, S. D., Ireland, T. R., Maas, R., Muir, R. D. & Shelley, D. (1997). Field characteristics, petrography, and geochronology of the Hohonu Batholith and the adjacent Granite Hill complex, North Westland, New Zealand. *New Zealand Journal of Geology and Geophysics* **40**, 1–17.

Waight, T. E., Weaver, S. D., Muir, R. J., Maas, R. & Edy, G. N. (1998). The Hohonu Batholith of North Westland, New Zealand: granitoid compositions controlled by source H_2O contents and generated during tectonic transition. *Contributions to Mineralogy and Petrology* **130**, 225–239.

Wark, D. A. & Miller, C. F. (1993). Accessory mineral behavior during differentiation of a granite suite: monazite, xenotime and zircon in the Sweetwater Wash Pluton, Southeastern California, USA. *Chemical Geology* **110**, 49–67.

Watson, E. B. & Harrison, T. M. (1983). Zircon saturation revisited: temperature and composition effects in a variety of crustal magma types. *Earth and Planetary Science Letters* **64**, 295–304.

Watt, G. R. & Harley, S. L. (1993). Accessory phase controls on the geochemistry of crustal melts and restites produced during water-undersaturated partial melting. *Contributions to Mineralogy and Petrology* **114**, 550–566.

Weaver, S. D., Bradshaw, J. B. & Adams, C. J. (1991). Granitoids of the Ford Ranges, Marie Byrd Land, Antarctica. In: Thomson, M. R. A., Crame, J. A. & Thomson, J. W. (eds) *Geological Evolution of Antarctica.* New York: Cambridge University Press, pp. 345–351.

Weaver, S. D., Adams, C. J., Pankhurst, R. J. & Gibson, I. L. (1992). Granites of Edward VII Peninsula, Marie Byrd Land: anorogenic magmatism related to Antarctic–New Zealand rifting. *Transactions of the Royal Society of Edinburgh: Earth Sciences* **83**, 281–290.

Weaver, S. D., Storey, B. C., Pankhurst, J. D., Mukasa, S. B., DiVenere, V. J. & Bradshaw, J. D. (1994). Antarctica–New Zealand rifting and Marie Byrd Land lithospheric magmatism linked to ridge subduction and mantle plume activity. *Geology* **22**, 811–814.

White, R. W. & Powell, R. (2002). Melt loss and the preservation of granulite facies mineral assemblages. *Journal of Metamorphic Geology* **20**, 621–632.

Wiedenbeck, M., Allé, P., Corfu, F., Griffin, W. L., Meier, M., Oberli, F. *et al.* (1995). Three natural zircon standards for U–Th–Pb, Lu–Hf, trace element and REE analysis. *Geostandards Newsletter* **19**, 1–23.

Wolf, M. B. & London, D. (1995). Incongruent dissolution of REE- and Sr-rich apatite in peraluminous granitic liquids: differential apatite, monazite and xenotime solubilities during anatexis. *American Mineralogist* **80**, 765–775.

Zeng, L., Asimow, P. D. & Saleeby, J. B. (2005). Coupling of anatectic reactions and dissolution of accessory phases and the Sr and Nd isotope systematics of anatectic melts from a metasedimentary source. *Geochimica et Cosmochimica Acta* **69**, 3671–3682.

APPENDIX

Analytical Methods
LA-ICP-MS U–Pb zircon chronology

Zircon U–Pb chronology was undertaken using laser ablation inductively coupled plasma mass spectrometry (LA-ICP-MS) at the Department of Geology, University of Maryland, with a UP-213 laser ablation system in conjunction with a ThermoFinnigan Element 2 single collector ICP-MS system. Fixed 30 or 15 μm diameter spots were used for analysis with a laser frequency of 10 Hz. U–Pb fractionation effects were corrected using zircon standard 91500 (Wiedenbeck *et al.*, 1995) and using the same spot size on both standard and unknown samples. Data reduction, isotope ratios and apparent age calculations were carried out with an Excel macro (Chang *et al.*, 2006). For each analysis the time-resolved signals and U/Pb ratios were carefully checked to detect perturbations. The Temora zircon standard (416·8 Ma, Black *et al.*, 2003) yielded a weighted $^{206}Pb/^{238}U$ age of 422 ± 9 Ma (2σ) ($n = 35$, MSWD $= 4\cdot2$). Concordant ages were calculated using Isoplot version 2 (Ludwig, 1999). The representative analytical results are given in Table 1; full data are available on request from the corresponding author.

Sr–Nd isotopic compositions

Sr and Nd isotopic compositions and Nd and Sm concentrations for several representative samples of various rock types were acquired at the Department of Geology, University of Maryland (Table 2). Rock powders (0·03–0·10 g) were dissolved for 3 days in a mixture of concentrated HF–HNO_3 in a Teflon bomb at 180°C. All samples were spiked with a ^{149}Sm–^{150}Nd mixed solution. Sr, Nd and Sm fractions were separated in two stages. In the first column, filled with BioRad AG 50W-X12 (200–400 mesh) resin, Sr and total REE fractions were collected by eluting with 2·5N HCl and 6N HCl, respectively. The second-stage purification of the Sr fraction was performed using Eichrom Sr-SPEC resin. Nd and Sm fractions were separated from the total REE fraction by eluting with 0·34N HCl and 0·7N HCl, respectively, using the second column filled with Eichrom Ln-resin. Sr fractions were loaded on Re filaments with a Ta activator and isotope ratios were measured in dynamic collection mode on a VG Sector mass spectrometer. $^{86}Sr/^{88}Sr$ ratios were normalized to 0·1194 for mass fractionation correction. Multiple analyses of the NBS987 standard analysis during this study averaged $^{87}Sr/^{88}Sr$ of $0\cdot710247 \pm 0\cdot000012$ (1σ, $n = 23$). Nd fractions were introduced into a Nu Plasma Multi-Collector ICP-MS system with an APEX desolvating nebulizer. Nd isotope rations were measured in static collection mode. Mass fractionation was corrected by normalizing to a $^{146}Nd/^{144}Nd$ of $0\cdot7219$. Repeated analyses of the AMES Nd standard during this study gave a $0\cdot512171 \pm 0\cdot000014$ (1σ, $n = 39$). All $^{143}Nd/^{144}Nd$ ratios measured in the samples were corrected for instrumental bias to an AMES standard $^{143}Nd/^{144}Nd$ value of $0\cdot512138$ (in-house TIMS measurements). Using this method, average $^{143}Nd/^{144}Nd$ for BHVO-2 standard is $0\cdot512984 \pm 0\cdot000015$ (1σ, $n = 7$). Nd and Sm concentrations were determined by isotope dilution analyses with a Nu Plasma Multi-Collector ICP-MS system.

ICP-MS trace element analysis

Trace element analyses were performed using solution-based ICP-MS techniques at the Department of Geology, University of Maryland following a method similar to that previously reported by Day *et al.* (2008), with some modifications. Two digestion techniques were employed during the course of this study. First, all samples were prepared using Savillex Teflon vials on a hotplate for >72 h at

150°C and then selected samples were digested in Teflon bombs at >180°C for >72 h in an oven. The reason for using Teflon bombs was because of the persistence of acid-resistant phases such as zircon within the hotplate digestion experiments for some samples. The results of these experiments show limited differences for all elements with the exception of Zr and Hf.

In both digestion experiments, 0.1 ± 0.001 g of homogenized whole-rock powder was digested in a 4:1 mixture of concentrated HF and HNO_3. Digestion vessels were then allowed to cool, were uncapped, and solutions were taken to incipient dryness. The residues were then taken into solution with concentrated HNO_3 and dried down twice to remove any residual fluorides. Samples were spiked with indium for internal normalization and drift correction and diluted by a factor of 5500 in 3% HNO_3. International standards BCR-1, BIR-1, BHVO-2, BHVO-1, JB-2 and G-2 were prepared with samples and include basaltic, granitic and shale standards for appropriate matrix matching. Solutions were measured using an Element 2 single collector ICP-MS system at the University of Maryland in low-resolution mode. Samples were introduced via a cyclonic spray chamber with oxide production below 3%. Raw data were corrected offline for blank contributions (which were low and consistent) and drift (which was found to be negligible during analysis), and were calibrated and monitored relative to accepted values of international standards BHVO-1, JB2 or BHVO-2 standards. Reproducibility was better than 3% for most elements, with the exception of U and Th (better than 5%). Standards run as unknowns are reported in Supplementary Table 1, which is available for downloading at http://www.petrology.oxfordjournals.org.